

Reflection of Solar Radiation by Inhomogeneous Clouds

Tamás Várnai

Department of Atmospheric and Oceanic Sciences
McGill University
Montreal, Canada.

October 1996

A thesis submitted to the Faculty of
Graduate Studies and Research
in partial fulfilment of the requirements of the degree of
Doctor of Philosophy

© Tamás Várnai



National Library
of Canada

Acquisitions and
Bibliographic Services Branch

395 Wellington Street
Ottawa, Ontario
K1A 0N4

Bibliothèque nationale
du Canada

Direction des acquisitions et
des services bibliographiques

395, rue Wellington
Ottawa (Ontario)
K1A 0N4

Your file *Votre référence*

Our file *Notre référence*

The author has granted an irrevocable non-exclusive licence allowing the National Library of Canada to reproduce, loan, distribute or sell copies of his/her thesis by any means and in any form or format, making this thesis available to interested persons.

The author retains ownership of the copyright in his/her thesis. Neither the thesis nor substantial extracts from it may be printed or otherwise reproduced without his/her permission.

L'auteur a accordé une licence irrévocable et non exclusive permettant à la Bibliothèque nationale du Canada de reproduire, prêter, distribuer ou vendre des copies de sa thèse de quelque manière et sous quelque forme que ce soit pour mettre des exemplaires de cette thèse à la disposition des personnes intéressées.

L'auteur conserve la propriété du droit d'auteur qui protège sa thèse. Ni la thèse ni des extraits substantiels de celle-ci ne doivent être imprimés ou autrement reproduits sans son autorisation.

ISBN 0-612-19781-6

Abstract

The goal of this study is to improve knowledge about how cloud inhomogeneities affect the reflection of solar radiation. In particular, it addresses two main questions: what the processes through which inhomogeneities influence solar reflection are, and how this influence can be taken into account in albedo retrievals based on future satellite measurements.

The first question is important, since present methods give numerical results only about the overall radiative effect of cloud inhomogeneities, but cannot determine the degree to which various mechanisms are responsible for this overall effect. This study establishes a theoretical framework which defines and evaluates the various processes through which cloud inhomogeneities influence solar radiation. This framework is then used to examine quantitatively the inhomogeneity effects that occur in irregular cloud fields. Among other insights, it is shown and explained that identical variations in cloud optical thickness can cause much stronger inhomogeneity effects if they are due to variations in geometrical cloud thickness, and not in volume extinction coefficient (as assumed in previous studies of irregular cloud fields). The differences in albedo can exceed 0.05, and the relative differences in reflectance toward the zenith can be greater than 25% for overhead sun, and 50% for oblique sun. Also, a possible explanation is given for a phenomenon observed in previous studies: that cloud reflectivity toward the zenith increases with decreasing solar elevation.

This study also develops an albedo retrieval algorithm that considers radiative inhomogeneity effects. The algorithm takes advantage of the unique multi-view capability of the Multi-angle Imaging SpectroRadiometer (MISR) placed on the Earth Observing System-AM satellite (to be launched in 1998). This instrument will offer new possibilities for albedo retrievals since, unlike present instruments, it will measure the radiation reflected in not only one, but nine directions. The potential accuracy of the algorithm is analyzed for a dataset obtained by using a Monte Carlo model to simulate radiative transfer through a large number of irregular cloud fields. The results indicate that using multi-view measurements can improve the accuracy of satellite-based albedo retrievals by a factor of three or more.

Résumé

Le but de cette étude est de mieux comprendre les effets de l'hétérogénéité des nuages sur la réflexion de la radiation solaire. En particulier, on se pose deux questions: quels sont les processus dont l'hétérogénéité influence la réflexion solaire, et comment tenir compte de cette influence dans les données d'albédo qui seront prises par les satellites dans le futur.

La première question est importante puisque les méthodes courantes ne donnent que des résultats numériques sur l'ensemble des effets de l'hétérogénéité, mais n'évaluent pas l'importance des mécanismes divers. Cette étude développe un modèle théorique pour définir et évaluer les processus dont l'hétérogénéité des nuages influence la radiation solaire. Ce modèle est utilisé pour examiner d'une façon quantitative les effets de l'hétérogénéité des nuages. Parmi d'autres découvertes, l'étude démontre que des variations identiques dans l'épaisseur optique des nuages peuvent produire des effets d'hétérogénéité beaucoup plus importants lorsque les variations proviennent de l'épaisseur géométrique des nuages et non du coefficient d'atténuation par volume (comme cela était présumé dans des études antérieures sur les champs de nuages irréguliers). Les différences d'albédo peuvent dépasser 0.05 et celles de la réflectance vers le zénith peuvent être supérieures à 25% pour un soleil direct et 50% pour un soleil oblique. Aussi, une explication possible est donnée pour un phénomène déjà observé dans des études précédentes que la réflectivité des nuages vers le zénith augmente lorsque l'élévation solaire diminue.

Cette étude développe également un algorithme pour évaluer l'albédo en tenant compte des effets radiatifs de l'hétérogénéité. Cet algorithme profite de la capacité unique de prises de vues multiples du "Multi-angle Imaging SpectroRadiometer (MISR)" qui se trouve sur le satellite "Earth Observing System-AM" (qui sera lancé en 1998). Cet instrument offrira des nouvelles possibilités pour l'évaluation de l'albédo puisqu'il mesure la radiation réfléchie dans neuf directions et non dans une seule direction, comme le font les instruments courants. La précision potentielle de l'algorithme est analysée avec des données qui proviennent d'une simulation de Monte Carlo pour le transfert radiatif à travers un grand nombre de champs de nuages irréguliers. Les résultats démontrent que l'utilisation de mesures avec des prises de vues multiples peut améliorer la précision des données d'albédo provenant de satellites par un facteur d'au moins trois.

Acknowledgments

I am sincerely grateful to my supervisor, Roger Davies for his invaluable advice and guidance. I also greatly appreciate his patience and trust throughout my studies.

I would also like to thank the Jet Propulsion Laboratory of the California Institute of Technology for financial support under Contract 959085.

Thank you to Catherine Moroney and Lisa Ramsaran for their great help in the computing aspects of this study. Also, many thanks to my fellow students Larry Di Girolamo, Norman Loeb, and Lazaros Oreopoulos for their valuable help and enlightening discussions throughout our years at McGill. Also, thank you to Marc Klasa for translating the abstract of this thesis into French.

I wish to express special thanks to my parents and my brother for their encouragement in entering McGill's graduate program, and for their moral support throughout my studies.

Finally, I am infinitely grateful to my wife, Laura Atwood, for proofreading the manuscript and providing wonderful support and motivation for me.

Statement of Originality

This thesis contains the following original contributions to knowledge:

- It establishes a theoretical framework to define and evaluate the various processes through which cloud inhomogeneities influence solar radiation. This framework is then used to obtain and explain the following results:
 - Identical variations in cloud optical thickness can lead to significantly different radiative properties if the variations are due to variations in the volume extinction coefficient (as assumed in previous studies of irregular cloud fields) or in geometrical cloud thickness. For overhead sun, the differences in albedo are comparable in magnitude to the effects of radiative interactions among nearby cloud elements (3-D effects), and can exceed 0.05. For oblique sun, the differences are smaller, but can still be significant.
 - For oblique sun, 3-D effects decrease the scene albedo primarily by making the reflection of upwelling photons more difficult, as opposed to making the transmission of downwelling photons easier.
 - The main means by which 3-D effects decrease the albedo of clouds with volume extinction coefficient variations is the flow of radiation from thick to thin regions. In the case of cloud top height variations, however, the main means is the flow of radiation from thin to thick regions.
 - For overhead sun, 3-D effects can increase the albedo even if neither absorption nor surface reflection occurs. This implies that the Independent Pixel Approximation underestimates the albedo of some inhomogeneous cloud scenes.
 - The addition of an underlying homogeneous, plane-parallel cloud layer can enhance 3-D radiative inhomogeneity effects.

- It offers a possible explanation of why cloud reflectivity toward the zenith increases with decreasing solar elevation. (This phenomenon has been observed in previous studies.)
- It develops an albedo retrieval algorithm to take advantage of the unique multi-angle view capability of the future satellite instrument, the Multi-angle Imaging SpectroRadiometer (MISR).
- It presents an error analysis of the developed algorithm which demonstrates that the use of multi-view satellite measurements can improve the accuracy of cloud albedo retrievals.

Table of Contents

ABSTRACT	i
RÉSUMÉ	ii
ACKNOWLEDGMENTS	iii
STATEMENT OF ORIGINALITY	iv
TABLE OF CONTENTS	vi
LIST OF FIGURES	viii
LIST OF TABLES	xii
LIST OF ABBREVIATIONS	xiii
1 INTRODUCTION.....	1
1.1 Solar Radiation and Clouds.....	1
1.2 Radiative Effects of Cloud Inhomogeneities.....	2
1.3 MISR - A Future Satellite Instrument	5
1.4 Thesis Outline	8
2 MODELING TOOLS.....	9
2.1 Representation of Inhomogeneous Cloud Structures.....	9
2.1.1 Overview of methods for defining cloud structures	9
2.1.2 Cloud structure generation.....	14
2.2 Radiative Transfer Modeling	20
2.2.1. Overview of methods for calculating radiative transfer.....	20
2.2.2. Monte Carlo radiative transfer model.....	23
2.2.2.1 Physics of the model	23
2.2.2.2 Realization of the radiative transfer model.....	25

3	SHORTWAVE RADIATIVE TRANSFER IN INHOMOGENEOUS CLOUD FIELDS	30
3.1	Definitions of Shortwave Radiative Inhomogeneity Effects	31
3.1.1	One-dimensional inhomogeneity effect.....	33
3.1.2	Three-dimensional inhomogeneity effects	42
3.2	Quantitative Analysis of Radiative Inhomogeneity Effects.....	51
3.2.1	Overhead sun.....	52
3.2.2	Oblique sun.....	69
3.2.3	Effects of Cloud Inhomogeneities on Nadir Reflectance.....	98
4	AN ALGORITHM FOR ALBEDO RETRIEVALS USING MULTI-VIEW SATELLITE DATA	108
4.1	Standard MISR Albedo Products.....	108
4.2	General Approach.....	109
4.3	Azimuthal Model Database.....	117
4.3.1	Cloud database.....	117
4.3.2	Azimuthal models.....	119
4.4	Choosing an Azimuthal Model for Observed Scenes.....	122
4.5	Uncertainty Estimations.....	124
4.5.1	Testing the behavior of retrieval algorithms	124
4.5.2	Benefits of using multiple views.....	126
5	CONCLUSIONS	133
	APPENDIX A.....	139
	REFERENCES.....	141

List of Figures

Figure 2.1.1	Top and side views of a cloud field generated using a stochastic model.	17
Figure 2.1.2	Landsat-TM images used in the study.....	19
Figure 3.1.1	1-D inhomogeneity effect.....	32
Figure 3.1.2	Influence of cloud variability on the 1-D inhomogeneity effect.....	34
Figure 3.1.3	Solar beams passing through an inhomogeneous cloud layer.....	36
Figure 3.1.4	Microphysical variations in the TIPA	37
Figure 3.1.5	Analogy between IPA-TIPA and equator-pole differences	40
Figure 3.1.6	Accuracy of albedo estimates based on the IPA and the TIPA for the cloud field shown on Figure 2.1.1.....	41
Figure 3.1.7	Paths of photons that experience 3-D IH effects in clouds having cloud top height and volume extinction coefficient variations	44
Figure 3.1.8	Photon paths if 3-D effects are and are not present.....	49
Figure 3.2.1	A regular array of infinite slabs	53
Figure 3.2.2	Turreted stratus geometry.....	53
Figure 3.2.3	Sensitivity of 3-D effects to τ_{pp} for turreted stratus clouds.....	54
Figure 3.2.4	Influence of radiation flowing from thin to thick and from thick to thin areas on the albedo of turreted stratus clouds	55
Figure 3.2.5	Influence of radiation flowing from thin to thick and from thick to thin areas on the albedo of cloud fields with irregular cloud top height variations.....	57
Figure 3.2.6	Influence of 3-D IH effects due to cloud top height variations on scene albedo by affecting transmission and reflection.....	58
Figure 3.2.7	Influence of downward trapping on the albedo of scenes with a positive 3-D IH effect	59
Figure 3.2.8	Overall 3-D IH effects due to cloud top height and volume extinction coefficient variations for overhead sun	60
Figure 3.2.9	Two-column models for 3-D IH effects due to cloud top height and volume extinction coefficient variations.....	64

Figure 3.2.10	Effects of radiation flowing from thick to thin and from thin to thick areas for clouds with volume extinction coefficient variations.....	68
Figure 3.2.11	Influence of 3-D IH effects due to volume extinction coefficient variations on the scene albedo by affecting transmission and reflection.....	69
Figure 3.2.12	Solar zenith angle dependence of albedos obtained for the cloud field shown in Figure 2.1.1. The albedos are calculated using the homogeneous, plane-parallel assumption, the TIPA, and 3-D Monte Carlo simulations.....	70
Figure 3.2.13	Overall 3-D inhomogeneity effects for scenes with cloud top height variations	72
Figure 3.2.14	3-D inhomogeneity effects as a function of solar zenith angle for the cloud field shown in Figure 2.1.1	73
Figure 3.2.15	Amount of solar radiation intercepted by the two sides of simple clouds.....	76
Figure 3.2.16	Influence of 3-D IH effects on scene albedo for 0° and 60° solar zenith angles.....	79
Figure 3.2.17	Influence of cloud side slope on the magnitude of the upward trapping effect.....	83
Figure 3.2.18	Amount of radiation potentially available for downward trapping in the case of the cloud field shown in Figure 2.1.1	85
Figure 3.2.19	Amount of radiation that is affected by downward trapping after being scattered at a particular angle.....	86
Figure 3.2.20	Paths of photons that experience downward trapping in clouds with volume extinction coefficient variations.....	87
Figure 3.2.21	Forward motion of radiation in a homogeneous cloud.....	90
Figure 3.2.22	Average distance between the x-coordinates of points where transmitted photons enter the cloud top and leave the cloud base.....	91
Figure 3.2.23	Scattering angles suitable for downward escaping in the case of cloud top height variations.....	93
Figure 3.2.24	Mie scattering phase function at 0.865 μm wavelength for a droplet size distribution representative of the top of stratocumulus clouds	95

Figure 3.2.25	Comparison of the effects of radiation flowing from thick to thin and from thin to thick areas for 60° solar zenith angle	96
Figure 3.2.26	Comparison of the influence of 3-D IH effects on scene albedo by affecting transmission and reflection in the case of 60° solar zenith angle.....	99
Figure 3.2.27	Overall 3-D IH effects due to cloud top height and volume extinction coefficient variations at 60° solar zenith angle.....	101
Figure 3.2.28	Overall 3-D IH effects caused by volume extinction coefficient variations at 0° and 60° solar zenith angle	102
Figure 3.2.29	Dependence of observed nadir reflectances on solar zenith angle.....	103
Figure 3.2.30	Nadir reflectance as a function of solar zenith angle, as obtained through 3-D Monte Carlo simulations.....	105
Figure 3.2.31	Nadir reflectance for the same scenes as in Figure 3.2.30, but calculated using the TIPA instead of 3-D Monte Carlo simulations.	106
Figure 3.2.32	Influence of 3-D IH effects on nadir reflectance	107
Figure 4.1.1	The matching of multi-angle measurements using the concept of RLRA.....	109
Figure 4.1.2	Radiative interactions among neighboring regions	112
Figure 4.2.1	Division of the upward hemisphere into nine segments for the energy weighting scheme.....	113
Figure 4.2.2	Angular dependence of the reflected radiation for 60° solar zenith angle.....	115
Figure 4.2.3	Azimuth-dependent bias of the energy weighting scheme for a plane-parallel cloud.....	116
Figure 4.3.1	Albedo retrieval errors for inhomogeneous clouds in the case of 60° solar zenith angle and 30° relative azimuth.....	121
Figure 4.5.1	Average albedo retrieval errors for plane-parallel clouds having modified gamma droplet size distributions with various modal radii.....	125
Figure 4.5.2	Average error if the albedo of plane-parallel clouds is retrieved using generic cloud models.....	126
Figure 4.5.3	RMS error of estimates for inhomogeneous cloud albedos obtained using various cloud models and all nine cameras	127

Figure 4.5.4	RMS error of stochastic albedo retrievals using a single nadir view and nine views.....	128
Figure 4.5.5	The w_k camera weights for various solar zenith angles as a function of the camera viewing zenith angle.....	129
Figure 4.5.6	RMS retrieval errors if oblique cameras are obscured.....	130
Figure 4.5.7	RMS error of stochastic albedo retrievals at 0.443 μm and 0.865 μm wavelengths.....	132

List of Tables

Table 1.3.1	Main parameters of the EOS-AM 1 satellite..	5
Table 1.3.2	Main parameters of the MISR instrument.....	7
Table 2.1.1	Simple cloud structures in previous studies	10
Table 2.2.1	Various methods to solve the equation of radiative transfer for inhomogeneous clouds.....	21
Table 2.2.2	Monte Carlo uncertainties for 100 homogeneous plane-parallel and inhomogeneous cloud fields.....	27
Table 2.2.3	Comparison of plane-parallel albedos obtained using Monte Carlo simulations and the discrete ordinates method	28
Table 2.2.4	Comparison of fluxes obtained for cuboidal and cylindrical clouds with values reported in previous studies	29
Table 3.2.1	3-D inhomogeneity effects in a regular array of infinite slabs.....	52
Table 3.2.2	Input parameters for a set of artificially generated cloud fields.....	56
Table 3.2.3	3-D inhomogeneity effects for the cloud field shown in Figure 2.1.1.....	61

List of Abbreviations

ASTER	Advanced Spaceborne Thermal Emission and Reflection Radiometer
AVHRR	Advanced Very High-Resolution Radiometer
AZM	Azimuthal model
BRF	Bidirectional reflectance factor
BRDF	Bidirectional reflection distribution function
CERES	Clouds and Earth's Radiant Energy System
CF	Cloud fraction
CTH	Cloud top height
DE	Downward escaping
DT	Downward trapping
EOS	Earth Observing System
ERBE	Earth Radiation Budget Experiment
GCM	General circulation model
GOES	Geostationary Operational Environmental Satellite
IH	Inhomogeneity
IHE	Inhomogeneity effect
IPA	Independent pixel approximation
JPL	Jet Propulsion Laboratory
LWC	Liquid water content
MC	Monte Carlo
MISR	Multi-angle Imaging SpectroRadiometer
MODIS	Moderate-Resolution Imaging Spectroradiometer
MOPITT	Measurements of Pollution in the Troposphere
MTPE	Mission to Planet Earth
NASA	National Aeronautics and Space Administration
RLRA	Reflecting layer reference altitude
RMS	Root mean square
SZA	Solar zenith angle
SW	Shortwave
TIPA	Tilted independent pixel approximation
TOA	Top of atmosphere

UE Upward escaping
UT Upward trapping
VEC Volume extinction coefficient

Chapter 1

Introduction

1.1 Solar Radiation and Clouds

The solar radiation absorbed by the earth is the ultimate source of energy for all atmospheric processes. However, not all of the radiation which reaches the planet is absorbed; about 30% of it gets reflected back to space. Since clouds are responsible for about two-thirds of this reflection (Hartman 1994), a thorough understanding of how clouds affect solar radiation is very important for climate studies. This understanding is also important because, by using satellites to measure the radiation reflected from clouds, one can infer cloud properties that influence this reflection. As Rossow (1989) asserts, we must understand solar radiative transfer through clouds in order to obtain a global distribution of cloud properties.¹

Due to its high importance, the effect of clouds on solar radiation has been the focus of intense research efforts for several decades. Despite the great achievements of these efforts, some very important questions still remain unanswered (Harshvardhan 1991; Vonder Haar 1994). As Arking states in his review paper (Arking 1991), "clouds may have a strong influence on climate change, but we are far from knowing the magnitude or even the sign of this influence."² Our understanding of climate and our ability to model and predict possible climate changes suffer greatly from these uncertainties. For example, the study by Cess et al. (1990) shows that the main reason that 19 climate models from around the world have different sensitivities to increased carbon-dioxide levels is that they treat cloud feedback processes differently.³ The measurement of cloud properties from satellites is also

¹Clouds not only affect solar radiation, but, conversely, are also influenced by the solar energy they absorb (Jonas 1989; Boers and Mitchell 1994; Xu 1995).

²The results of a recent study by Chou et al. (1995) suggest that clouds may decrease the energy available for the Earth-Atmosphere system, even if the longwave effect is included.

³The study of Ellingson and Fouquart (1990) shows that radiative processes are represented more accurately in climate models for clear than for cloudy conditions.

highly limited by the uncertainties in our understanding of solar radiative processes which occur in clouds (Marshak et al. 1995b; Pincus et al. 1995).

Due to the high importance of its still unresolved questions, the radiative effect of clouds is widely regarded as one of the most urgent problems in current climate research. For example, the Intergovernmental Panel on Climate Change set up by the United Nations recognized it as a key area of scientific uncertainty (IPCC, 1990). Also, the study of the role that clouds play in our climate is the top priority of the United States Global Change Research Program. Similarly, the first scientific priority of the Earth Observing System—the centerpiece of the US satellite remote sensing efforts over the next few decades—is to study cloud formation, dissipation and radiative properties (Asrar and Dokken 1993; Wielicki et al. 1995).

Dozens of publications and the worldwide survey of 25 research centers by Browning (1994) indicate that the scientific community views the inhomogeneous nature of clouds as a very important, but poorly known factor in determining the radiative effects of clouds. Hence, the main goal of this thesis is to improve understanding of the shortwave radiative effects of cloud inhomogeneities and to develop new methods for including these effects in the interpretation of satellite data.

1.2 Radiative Effects of Cloud Inhomogeneities

Three-dimensional radiative transfer is such a complex process that present climate models and satellite data interpretation methods cannot fully represent it. Instead, they use one-dimensional approximation which assumes that clouds appear in homogeneous, plane-parallel layers. However, there is no doubt that cloud inhomogeneities exist. Everyday experience and numerous measurements (Stephens and Platt 1987; Jonas 1990) show that clouds are very inhomogeneous, both vertically and horizontally. Airplane measurements by Korolev (1993) reveal large variations even within stratiform clouds. Numerous studies, both theoretical and experimental, suggest that these inhomogeneities often have significant radiative effects that demand consideration.

Theoretical studies

Dozens of simulation studies have shown that inhomogeneities can alter the way clouds reflect solar radiation.⁴ Numerous experiments have also demonstrated that the plane-parallel, homogeneous representation of clouds leads to significant errors in both climate models (Welch and Wielicki 1984; Harshvardhan and Randall 1985) and satellite retrievals of cloud properties (Davies 1984; Coakley and Kobayashi 1989; Barker and Liu 1995).

Since most studies used highly idealized (for example cuboidal) inhomogeneous clouds, the majority of results can only be used in a qualitative sense. Therefore, further studies, based on more realistic cloud fields, are needed to determine quantitatively the radiative effect of cloud inhomogeneities.

Experimental evidence

Various measurements (Stuhlmann et al. 1985; Cahalan et al. 1995) have established that radiative transfer through large areas cannot be represented accurately if the scene is assumed either to be completely covered by a homogeneous, plane-parallel cloud, or to be totally cloud free. These results imply that exact radiative transfer calculations require knowledge of the frequency distribution of cloud thicknesses. Furthermore, some studies point out that even this frequency distribution may not be sufficient, because the spatial distribution of the various thicknesses is also important. For example, Davies (1978, 1994) and Hayasaka et al. (1995) have shown that local fluxes of transmitted and reflected radiation depend not only on local cloud properties, but also on interactions among neighboring cloud elements.

It is much more difficult to demonstrate that not only local, but also scene average radiative properties are affected by interactions of nearby cloud elements. The main problem is to distinguish the effects of cloud inhomogeneity from those of other poorly known properties (for example, cloud droplet size distribution). Nevertheless, numerous studies have been able to reveal behaviors in various measurements that were inconsistent with the one-dimensional theory of homogeneous clouds. In his study of cloud albedos—the ratio of reflected flux to incoming radiative energy—Davies (1978) points out that cloud inhomogeneities can explain the "albedo paradox," i.e., that cloud albedos rarely exceed

⁴Table 2.1.1 displays a long, but far from complete list of references.

0.8, even though plane-parallel calculations based on cloud microphysical measurements would often predict otherwise. Coakley and Davies (1986) have shown that at wavelengths where clouds absorb significant amounts of solar radiation, broken cloud fields tend to reflect more radiation than overcast cloud fields. This finding contradicts the one-dimensional theory but is consistent with the properties of inhomogeneous clouds. Recently, Loeb and Davies (1996a,b) found that cloud reflection depends on solar elevation in a way that is inconsistent with plane-parallel theory. The differences were significant even if all liquid water clouds, including the most homogeneous stratiform clouds, were averaged together. These results indicate that cloud inhomogeneities have significant shortwave radiative effects. However, due to various uncertainties (such as cloud droplet size distribution), the magnitude of these effects could not yet be estimated accurately.

Even though radiative inhomogeneity effects are widely recognized to be very significant, the theory of how these effects work has not yet been fully examined. One of the main goals of this thesis is to address some of the still unexplored problems. The first such problem is that no precise definitions have existed for the solar radiative effects of cloud inhomogeneities and thus there has been no way to tell the degree to which various mechanisms are responsible for the overall effect of cloud inhomogeneities. In this study, quantitative definitions for these effects are developed and organized into a comprehensive classification scheme. This scheme is then used to examine the processes through which inhomogeneities affect cloud reflection. It is also used to demonstrate that radiative properties change significantly if the horizontal optical thickness variations which are observed from satellites are attributed not to variations in cloud density (as in previous studies), but to variations in the geometrical cloud thickness (which is probably a more realistic attribution for many Cumulus cloud fields). Finally, the proposed approach is also used to investigate whether cloud inhomogeneities may be responsible for the fact that nadir reflectance is larger for oblique than for overhead sun (Loeb and Davies 1996b), a phenomenon that seems to contradict the theory of radiative transfer in homogeneous clouds.

1.3 MISR - A Future Satellite Instrument

In 1990, the President of the United States launched the initiative Mission to Planet Earth (MTPE) with the goal of providing a scientific basis for understanding global change. The purpose of MTPE is to collect ground- and space-based measurements of all components of the climate system. The centerpiece of the mission is the Earth Observing System (EOS), a series of polar-orbiter and low-inclination satellites operated by the National Aeronautics and Space Administration (NASA). The EOS satellites are planned to take measurements from 1998 to 2017. The measurements obtained by the EOS satellites will be processed routinely at designated processing centers, and data from various stages of this processing will be made available to the wider research community (Price et al 1994). A more detailed overview of the EOS project can be found in the EOS Reference Handbook (Asrar and Dokken 1993).

Some of the instruments flown on EOS satellites will be improved versions of previous instruments, while others will realize new concepts for the first time. One of the instruments in the latter group will be the Multi-Angle Imaging SpectroRadiometer (MISR). MISR is scheduled to be flown on the EOS-AM satellites, the first of which is expected to be launched in June 1998. The main parameters of this satellite are shown in Table 1.3.1.

TABLE 1.3.1. Main parameters of the EOS-AM 1 satellite

Orbit	Descending polar orbit
Inclination	98.2°
Equator crossing time	10:30 AM
Height	705 km
Orbit repeat cycle	16 days (233 orbit)
Planned launch	June 1998
Instruments on board	ASTER, CERES, MISR, MODIS, MOPITT

ASTER = Advanced Spaceborne Thermal Emission and Reflection Radiometer
CERES = Clouds and Earth's Radiant Energy System
MISR = Multi-angle Imaging SpectroRadiometer
MODIS = Moderate-Resolution Imaging Spectroradiometer
MOPITT = Measurements of Pollution in the Troposphere

The main novelty of MISR is its multi-view capability. Most current geophysical instruments view a particular scene from only one angle at a time.⁵ (A comprehensive list of presently operating and planned geophysical satellite instruments can be found in Gurney et al. (1993).) Such instruments can only measure the amount of solar radiation reflected in a single direction, toward the satellite. The radiation that is reflected in other directions remains unknown. MISR, in contrast, will measure the radiation that is reflected in nine separate directions. Thus, the properties of a scene can be inferred based on how the scene looks not only from a single direction, but also from eight additional directions. This is possible because the instrument consists of nine cameras, each tilted at a different angle. Thus, when MISR approaches a particular scene, the most forward-tilted camera first sees the area. Within the next few minutes, as MISR gradually passes over the scene, the less forward-tilted and aft-tilted cameras also see the scene, each camera from a different angle. This way the reflection from the scene can be measured from nine directions during the seven minute interval of the satellite's passage. The main parameters of the MISR instrument are shown in Table 1.3.2.

Since MISR is the first instrument of its kind, there are no well-developed and thoroughly tested methods available to process its measurements. Thus the MISR science team, set up by NASA to design algorithms for the routine processing of MISR data, has had to develop various new concepts and approaches. Theoretical studies by members of the science team demonstrate that MISR's multi-angle data will improve our ability to retrieve aerosol optical properties (Wang and Gordon 1994), to correct surface reflectances for atmospheric effects (Diner et al. 1994) and to detect thin Cirrus clouds (Di Girolamo and Davies 1994). Novel algorithms are also being developed for cloud top height and wind field retrievals as well as for the determination of various aerosol and surface properties (Diner et al. 1995a, 1995b, 1995c).

One of the most important purposes of MISR is to provide accurate albedo measurements. When single-view instruments are used, the total reflection from a scene must be estimated from the amount of radiation reflected in a single direction. Therefore, models are needed to estimate the radiation that is reflected in all other directions. Such angular models have been constructed both theoretically (based on various physical assumptions (Rossow 1989)), and statistically (using the distribution of measurements taken at various view

⁵The French SPOT, the European ATSR-2 and the Japanese OPS instruments can provide stereoscopic data as well, and the recently launched POLDER instrument can also provide some multi-angle measurements.

angles (Taylor and Stowe 1984)). However, Stuhlmann et al. (1985) and Loeb and Davies (1996a) have demonstrated large differences between theoretically derived and statistically constructed angular models. The errors of both approaches are due to variations in cloud and surface properties that cannot be deduced from satellite data. Unfortunately, assumptions based on an incorrect angular model can lead to large biases in the estimated albedo values.

TABLE 1.3.2 Main parameters of the MISR instrument

9 camera angles at the surface	0°, ±26.1°, ±45.6°, ±60.0°, ±70.5°
spectral coverage	10 nm wide bands at 443, 555, 670 and 865 nm
spatial coverage	from 80°South to 80° North
return time*	9 days at the equator 2 days near the poles
Spatial resolution**	
cross-track sample spacing	250m for nadir, 275 m for off-nadir cameras
cross-track IFOV	250m for nadir, 275 m for off-nadir cameras
along-track sample spacing	275 m
along-track IFOV	214-707 m
total swath width measured by all cameras	360 km
Radiometric performance	
signal to noise ratio	linear encoding of 14 bits degraded to square-root encoding of 12 bits
calibration accuracy	more than 300 3-6% absolute uncertainty 1-2% camera-by-camera, band-by-band uncertainty

* Time between consecutive measurements of the same area.

** A 4x4 on-board averaging will be performed on the measurements of all non-nadir cameras for all but the red channel.

Since MISR will measure the solar reflection from not only one, but nine separate directions, it is expected to provide much more accurate albedo estimates than single view instruments. However, because the radiation reflected to directions other than the nine measured ones will still remain unknown, angular models will still be needed for the estimation of albedo values.

The main source of uncertainties in angular models of cloud reflection—and thus in cloud albedo estimates as well—is the effect of cloud inhomogeneities (e.g., Davies 1984; Rossow 1989; Coakley and Kobayashi 1989; Loeb and Davies 1996a). One of the main goals of this thesis is to develop new methods of estimating the albedo of inhomogeneous clouds during the routine processing of future MISR data.

1.4 Thesis outline

The overall goal of the work presented in this thesis is to improve knowledge about the solar reflection of inhomogeneous clouds. In particular, the mechanisms of radiative inhomogeneity effects are examined, and a new approach is developed to account for them in the processing of future satellite measurements. The outline of the thesis is as follows.

Chapter 2 describes the main tools used in the study to represent inhomogeneous clouds and to calculate radiative transfer through the cloud fields. Chapter 3 contains theoretical results about the shortwave radiative effects of cloud inhomogeneities. A comprehensive classification scheme for these effects is developed and applied to examine various aspects of cloud reflection. Chapter 4 describes a new algorithm that has been developed to infer the albedo of inhomogeneous clouds from future satellite measurements. This albedo-retrieval method takes advantage of the unique multi-view capability of the planned MISR instrument. Thus Chapters 3 and 4 complement each other: Chapter 3 deals with the theory of how radiative inhomogeneity effects work, and Chapter 4 describes a way to measure them more accurately. Finally, Chapter 5 contains some concluding remarks.

Chapter 2

Modeling Tools

The main purpose of this chapter is to describe the modeling tools that are used in the present study. Section 2.1 describes how inhomogeneous cloud are represented, and section 2.2 presents the radiative transfer model that has been implemented for this study.

2.1 Representation of Inhomogeneous Cloud Structures

2.1.1 Overview of methods for defining cloud structures

Radiative inhomogeneity studies can take one of three approaches to define inhomogeneous cloud structures: 1) the use of simple cloud geometries, such as cubes; 2) retrieval of cloud structure from various measurements; and 3) generation of stochastic fields using cloud models.

Simple cloud geometries have been in widespread use ever since the first inhomogeneity studies. Table 2.1.1 shows a list of various cloud structures studied. One of the reasons for their popularity is that these structures are very suitable for studying the basic mechanisms of radiative inhomogeneity effects. For example, the small number of geometrical parameters involved and the researcher's full control over the cloud field can help in examining how various physical cloud properties can affect radiative transfer (Davies 1978; Barker 1994). The other reason for the popularity of simple geometrical structures is that radiative transfer calculations involving them are relatively simple and therefore rapid. This is especially important in the development of new two- or three-dimensional radiative calculation methods (Davies 1978; Kobayashi 1991; Sánchez et al. 1992). Some simple cloud geometries are used in the present study as well. For example, regular arrays of infinite slabs are considered in Chapter 3 in order to study some basic properties of radiative inhomogeneity effects.

TABLE 2.1.1. Simple cloud structures in previous studies

Cubes	McKee and Cox (1974); Davies (1976, 1978, 1984); Aida (1977); McKee and Klehr (1978); Davis, Cox and McKee (1979, 1983); Welch et al. (1980); Welch and Zdunowski (1981); Davies et al. (1984); Schmetz (1984); Welch and Wielicki (1984); Coakley and Davies (1986); Davis and Cox (1986); Kobayashi (1988); Bréon, (1992); Barker (1992, 1994); Kobayashi (1993); Gierens (1993); Li, Geldart and Chylek (1994a)
Cloud bars	Harshvardhan and Thomas (1984); Smith and Ehlert (1993); Hayasaka et al. (1995)
Turreted Clouds	Davies (1976); Wendling (1977); McKee and Klehr (1978); Kobayashi (1993); Chylek and Dobbie (1995)
Hexagonal cells	Jonas (1994)
Cylinders	Busygin et al (1973); Welch and Zdunowski (1981); Welch and Wielicki (1984); Kobayashi (1988); Alberta and Cox (1990); Bréon (1992)
Spheres and hemispheres	Busygin et al (1973); Welch and Zdunowski (1981); Davies (1984); Welch and Wielicki (1984); Kobayashi (1988)
Paraboloids	Busygin et al (1973); Busygin et al (1977)
Waves	Gaussian wave: Kobayashi (1991) Sinusoidal waves: Li, Geldart and Chylek (1994b); Gabriel and Evans (1996)

Real clouds, however, display very complex structures that cannot be represented through simple geometrical shapes. Therefore, the quantitative study of radiative inhomogeneity effects requires the use of much more complex clouds structures, based on either measurements or cloud models.

Cloud measurements could theoretically offer an ideal way to obtain realistic cloud structures. Unfortunately, to date it has proved nearly impossible to obtain accurately the full three-dimensional distribution of cloud properties, especially the volume extinction coefficient (VEC).

The most reliable data have been obtained by *in situ* aircraft measurements. For example, Barker (1992) used such data for radiative studies. Unfortunately, the use of *in situ* data is severely limited by the fact that, since airplanes can give only one-dimensional transects through cloud fields, the full three-dimensional distribution of cloud properties remains unknown. The same problem arises if ground-based microwave radiometers are used for optical depth retrieval (Cahalan and Snider 1989; Cahalan et al. 1994a). The effects of this limitation have been studied by Barker (1996b) who found that the use of one-dimensional transects (instead of three-dimensional structures) can lead to large biases in the calculated radiative properties.

Stackhouse and Stephens (1994) used cloud measurements taken by a Ka band radar. The main limitation of such measurements is in transforming radar reflectances into shortwave radiative properties (Atlas et al. 1995).¹ If the uncertainties of this transformation could be reduced significantly, radar measurements could prove very useful in future radiative studies.

The most commonly used data in shortwave radiative studies come from satellite measurements. Usually, visible radiances measured by a satellite are used to infer the horizontal distribution of cloud optical depth τ . Since τ -retrievals are not based on three-dimensional radiative transfer calculations, most studies use the Independent Pixel Approximation (IPA) (Rossow et al. 1985; Coakley and Kobayashi 1989; Marshak et al. 1995a). This approximation assumes that the radiance measured at each pixel of a satellite image depends only on the radiative properties within the pixel in question (i.e., it is independent of the neighboring pixels). This assumption allows the use of one-dimensional radiative transfer models, and thus makes the satellite retrievals feasible. Unfortunately, the neglect of interactions among nearby pixels can lead to large biases (Barker and Liu 1995; Hayasaka et al. 1995; Marshak et al. 1995b). Other uncertainties in cloud microphysics and surface reflection properties can further increase the errors. Despite all the uncertainties,

¹This problem did not arise for Haferman et al. (1994), who used 3-D radar measurements to study the microwave radiative effects of cloud inhomogeneities.

however, satellite retrievals can still give valuable information about cloud inhomogeneities. They are therefore used in the present study as well.

Cloud models are also often used in radiative studies. Since dynamical-microphysical cloud models require very lengthy calculations, only a few studies have used them (Barker 1994). For this reason, stochastic cloud models have gained widespread use in radiative studies. Stochastic models are usually not based on strict physical principles; instead, they try to produce cloud fields that resemble real ones. In order to find out how the generated fields should look, many studies have examined the structure of various observed cloud fields (for example, Lovejoy 1982; Cahalan and Snider 1989; Lovejoy and Mandelbrot 1985; Barker and Davies 1992b; Lovejoy et al. 1993; Pflug et al. 1993; Tessier et al. 1993).

A large group of stochastic models aims to reproduce the *scaling* observed in real cloud fields. The feature of scaling (Lovejoy and Mandelbrot 1985) means that, due to the flow of turbulent energy from larger to smaller scales, large-scale variations in cloud properties have large amplitudes, while small-scale variations tend to have smaller amplitudes. In other words, the variations in the τ optical thickness show scaling behavior if, for any $\lambda > 0$ ratio,

$$\tau_{(r)} - \tau_{(r+\lambda\Delta r)} \sim \lambda^s (\tau_{(r)} - \tau_{(r+\Delta r)}).$$

In this equation, r is the position vector and s is the scaling parameter. In terms of the Fourier spectrum of statistically isotropic cloud fields, this implies that the power P at any wavenumber k is inversely related to k through the scaling parameter s :

$$P(k) \sim k^{-s}$$

The value of s has been determined for various cloud fields by, for example, Cahalan and Snider (1989), Barker and Davies (1992b), and Tessier et al. (1993).

One group of scaling models is the discrete cascade models, e.g., the β and α models or the "bounded cascade model" (Frisch et al. 1978; Schertzer and Lovejoy 1987; Cahalan 1989; Barker 1992; Tessier et al. 1993; Gupta and Waymire 1993; Marshak et al. 1995b). As Schertzer and Lovejoy (1987) noted, these models lead to artificial-looking straight

structures in the generated cloud fields. To avoid this problem, they proposed the use of continuous cascade models.² Barker and Davies (1992a) and Padro-Igúzquiza and Chica-Olmo (1994) developed models that are similar to the continuous cascade models in that they also avoid the problem of artificially straight lines. An interesting model that simulates even the time-evolution of the generated cloud field is described in Lovejoy and Mandelbrot (1985). A list of some other stochastic cloud models can be found in Tessier et al. (1993).

Another group of stochastic cloud models aims at generating realistic cloud size and cloud spacing distributions directly, without using scaling laws (Titov 1990; Su and Pomraning 1994; Zuev and Titov 1995).

Unfortunately it is very difficult to evaluate how realistic the cloud fields produced by each model are, and hence it cannot yet be established which models are most appropriate for simulating various cloud types. A common limitation of all models is that although they can generate apparently realistic horizontal τ -distributions, the full three-dimensional distribution of the VEC can be obtained only by using some often unrealistic assumptions, such as homogeneous and isotropic turbulence. Some efforts, such as the development of the Generalized Scale Invariance (Lovejoy and Schertzer 1985; Pflug et al. 1993) have been made to overcome this problem, but no working model has resulted from these efforts yet.

Despite these problems, stochastic cloud models offer good possibilities for studying the radiative properties of a large variety of cloud fields. One reason for this is that using stochastic models makes it very easy to generate a large variety of inhomogeneous clouds. Numerous studies assert that the structures they generated using stochastic models reproduce the most critical features of cloud inhomogeneities (Cahalan 1989; Barker and Davies 1992a, b; Marshak et al. 1995a; Zuev and Titov 1995). Also, by changing the cloud fields' statistical parameters, one can easily study how various cloud properties affect solar radiation.³ Finally, stochastic models are not affected by some of the errors that may arise for other ways of representing clouds, such as introducing an unreal anisotropy if the cloud field is retrieved from visible satellite images measured at oblique sun. (In this case the sunlit side of clouds appear brighter than the shadowy side; hence, the retrievals would

²The terms "discrete" and "continuous" refer to whether the energy at a given wavenumber k can flow only to wavenumber $k' = 2k$, or to any k' greater than k , respectively.

³Another potential advantage of some stochastic models is that they can produce periodic cloud fields that do not have abrupt changes at their edges. This is especially important if radiative properties are to be calculated at high spatial resolution, since computational limitations often allow such calculations for such small scenes that the results for the entire scene may be altered erroneously by abrupt changes at the edge.

result in clouds that would systematically get thinner on the sides away from the sun.) As a result of these advantages, radiative studies often use, and will probably continue using stochastic models until new, more accurate measurements become available. The present study also relies on these models to a large extent. The specific methods used to generate cloud field structures are described in the next section.

2.1.2 Cloud structure generation

The present study uses three basic approaches—simple geometric shapes, stochastic cloud models and satellite measurements—to represent inhomogeneous cloud structures. The main purpose of this section is to describe in detail the various methods used for each of the three approaches.

Simple geometrical structures are used in Chapter 3 to study some basic properties of radiative inhomogeneity effects. Since it is fairly straight-forward to generate these structures, the exact geometries and arrangements are described in detail only in discussions of particular experiments which use them.

Stochastic cloud models are used for many of the experiments presented in Chapters 3 and 4. Two-dimensional fields of horizontal cloud optical thickness variations were generated using a model based on Barker and Davies (1992a). The main steps of the cloud generation process are as follows:

1. Generate random Fourier coefficients for the 2-D scene as a Gaussian white noise with zero mean and unit variance. Then multiply each coefficient $C(\mathbf{k})$ by $|\mathbf{k}|^{-s}$ to obtain the desired scaling (\mathbf{k} is the 2-D wavenumber vector).
2. Perform an inverse Fourier transform that yields a 2-D field of scaling random variations.
3. Obtain the desired cloud fraction CF by adding a constant to each pixel's value so that a $(1 - CF)$ fraction of pixels has negative values, and then setting all negative values to zero.
4. Multiply each pixel's value by a constant which produces a field with the desired scene-average optical thickness.

Some additional features were added to Barker and Davies's model:

- An optional break was included in the cloud field scaling, i.e., the scaling parameter $s(k)$ has different values depending on whether k is less than or greater than an adjustable critical value. The existence of such a break in real clouds is currently a topic of scientific debate, since it was observed in some studies (Cahalan and Snider 1989; Barker and Davies 1992b) but not in others (Lovejoy et al. 1993; Tessier et al. 1993).
- The algorithm was extended to three dimensions to produce VEC distributions that simulate homogeneous and isotropic turbulence.
- The option of exponentiating the field or raising it to a specific power was included between Steps 2 and 3 to produce multifractal cloud fields.

An example of the generated cloud fields used in this study is shown in Figure 2.1.1.

One limitation of the generated scenes is that, since they represent $(35.2 \text{ km})^2$ areas at 68 m resolution, they include variations only at scales between 68 m and 35.2 km. To estimate the importance of this limitation, a few scenes were generated at high (10 m) resolution, and then it was calculated how their radiative properties changed if the resolution was degraded to 80 m by a simple averaging over 8×8 pixel areas. It was found that variations at scales smaller than 80 m did not have significant radiative effects. However, there is no theoretical upper limit to the radiative effect of small-scale variations; in theory, they could have very large effects in extremely inhomogeneous clouds. Unfortunately, the degree to which real small-scale variations influence solar radiation can only be determined based on accurate high-resolution measurements of the three-dimensional cloud structure. Such measurements can be expected from future improvements in radar-based retrieval techniques, for example.

At the other end of the range of represented scales, the results of Davies (1994) suggest that cloud inhomogeneities at scales larger than 35.2 km can have significant radiative effects. (In particular, he showed that the principle of reciprocity is not fulfilled at the resolution of the ERBE instruments, which is somewhat lower than 35.2 km.) Until the importance of such large-scale variations is established, the results presented in this thesis should be considered most appropriate if such variations are not present. This can be the case, for

example, in the middle of cloud fields, whose nearby $(35 \text{ km})^2$ regions all have similar statistical properties.

As mentioned in Section 2.1.1, presently there is no way to evaluate how representative the generated fields are of real clouds. While the generated fields are not expected to accurately represent all atmospheric cloud types (for example, no multi-layer cloud situations are considered), it is believed that in producing irregular scaling fields, the model captures the most critical features of cloud variability. This is supported by the fact that the obtained results are qualitatively consistent with results of other studies (based on either measurements or various cloud models). In addition, to ensure that this study's results are not specific to the used cloud model, a few Landsat images were also used to define inhomogeneous cloud fields (described in detail below). The fact that the results obtained for the artificial scenes are consistent with those obtained for the Landsat scenes further suggests that the model captures the most critical features of cloud inhomogeneities.

The main implication of using artificial scenes is that, while quantitative results could be obtained for the generated cloud fields, only future studies (based on more representative cloud structures) can determine the exact magnitude of the described effects in the real atmosphere.

Satellite retrievals were also used to generate cloud structures in Chapters 3 and 4. Bruce Wielicki (of NASA Langley Research Center) courteously made six Landsat-TM images available for this study. Figure 2.1.2 shows the images containing cumulus and stratocumulus clouds over ocean. For computational reasons, each scene was divided into four rectangular segments, leading to 24 small scenes. These small scenes are especially important in ensuring that the conclusions obtained in the study are not specific to the stochastic cloud model described above.

a

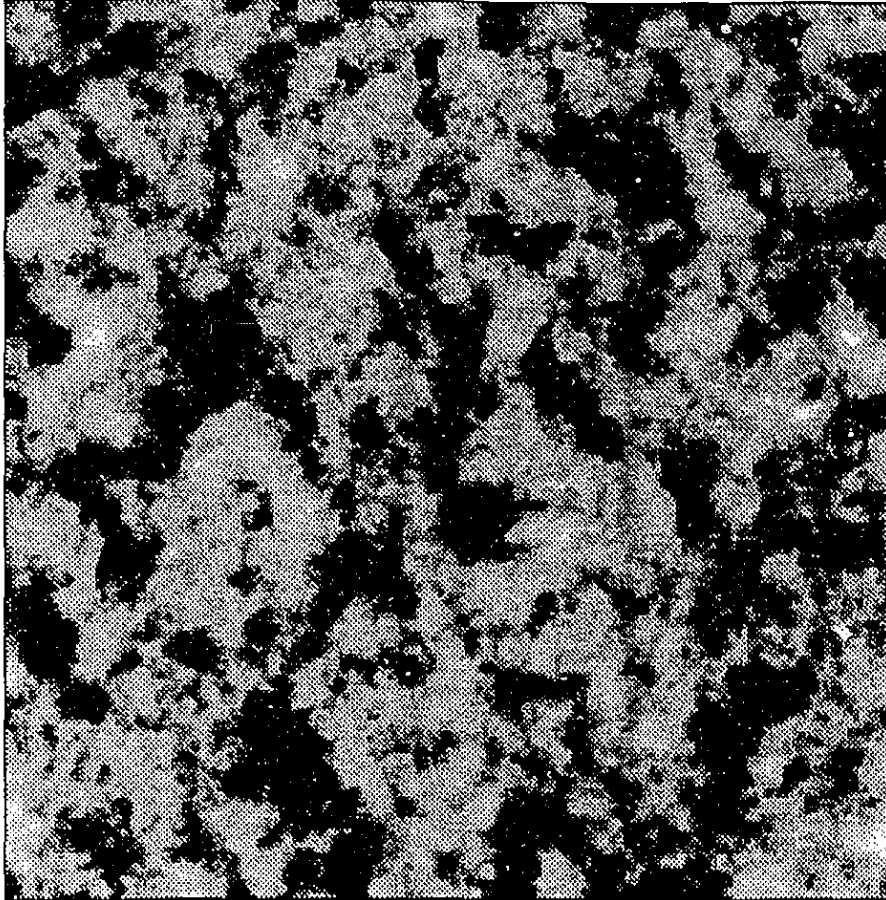
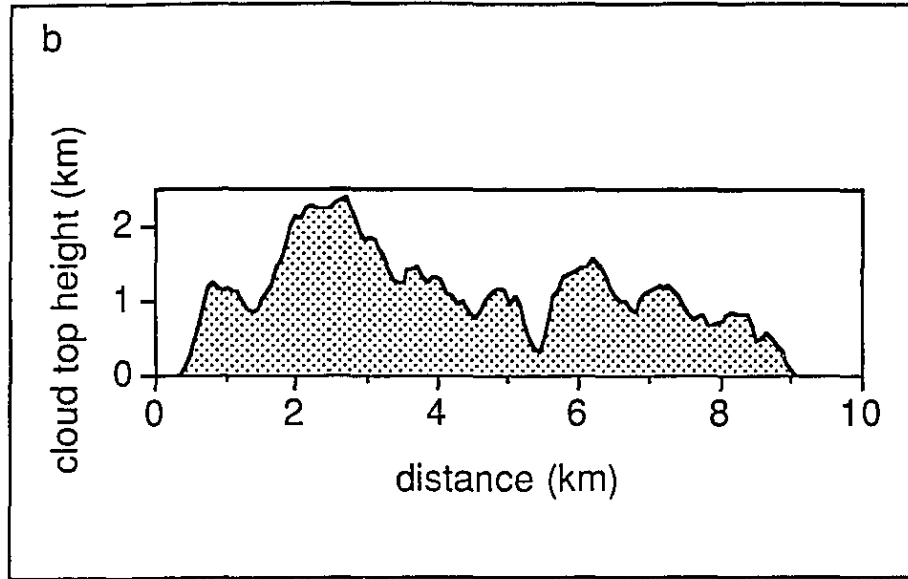


Figure 2.1.1. A cloud field generated using the stochastic cloud model. The cloud field, covering an area of 35.2×35.2 km at a resolution of 68 m, was generated using the input parameters $CF = 0.75$, $\langle \tau \rangle = 15$, $s_{(k)} = 1$ if $k \leq 10$, and $s_{(k)} = 3.6$ if $k > 10$. For 0° and 60° solar zenith angles, the average scene albedos are 0.35 and 0.51, respectively. (The albedos of a homogeneous cloud with $\langle \tau \rangle = 15$ would be 0.50 and 0.66 for the two solar zenith angles.) (a) Top view. The brightness of each pixel is proportional to its albedo, calculated for overhead sun using the Independent Pixel Approximation. (b) Vertical cross section of a cloud in the field, assuming $VEC = 30 \text{ km}^{-1}$.



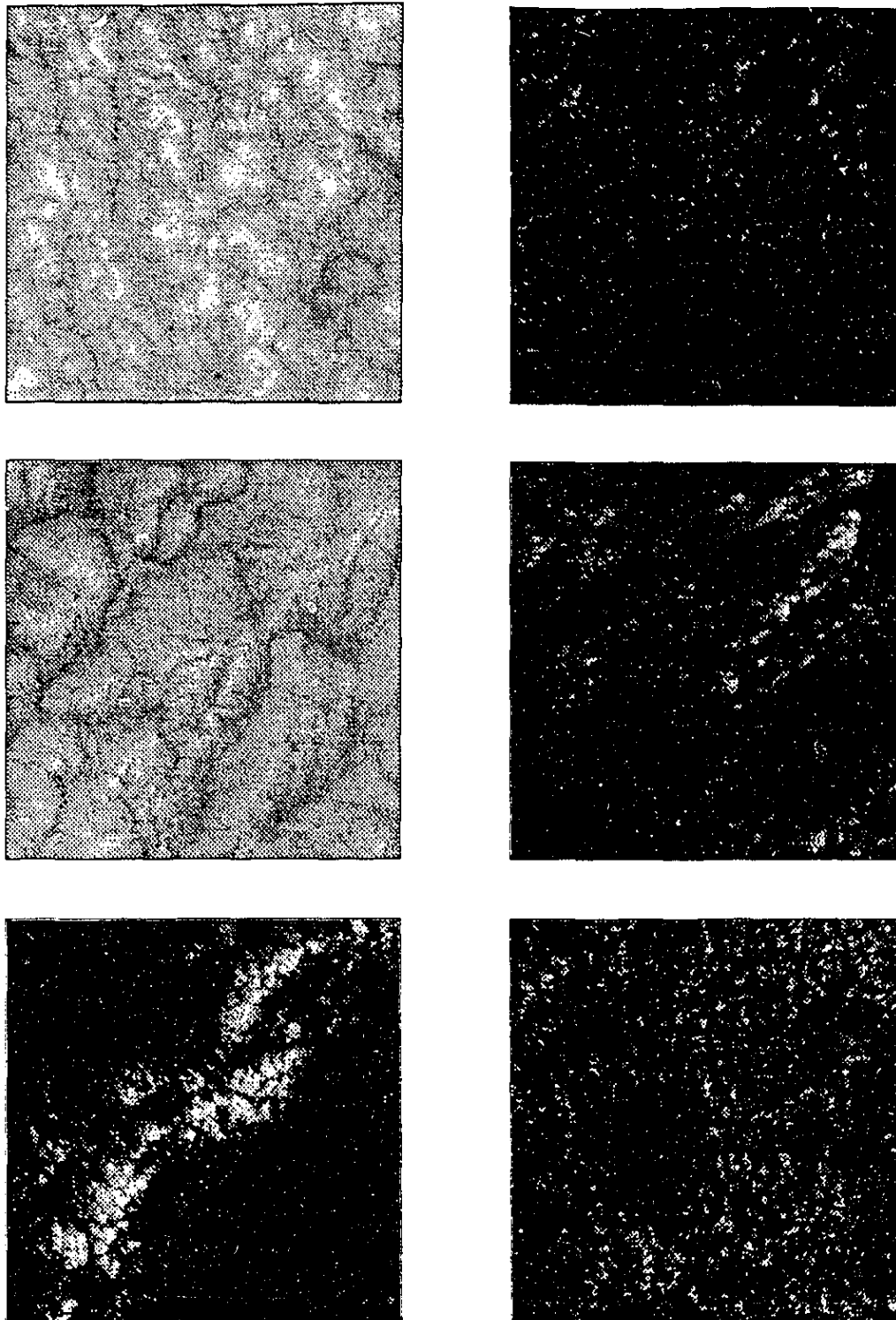


Figure 2.1.2. Landsat images used in the study. The scenes cover 57.3 x 57.3 km areas at 28 m resolution. The average cloud optical thickness varies between 2.8 and 18; the cloud fraction, between 0.13 and 1.

2.2 Radiative Transfer Modeling

2.2.1. Overview of methods for calculating radiative transfer

Since it is difficult to construct realistic physical cloud models and to measure their radiative properties, almost all studies have used mathematical models for radiative transfer calculations.⁴ Mathematical radiative transfer models either use Monte Carlo simulations of photon transport, or apply various techniques to solve the equation of radiative transfer.

Monte Carlo simulations

The basic idea of the Monte Carlo radiative transfer method is to use a computer's random number generator to simulate the path of individual photons through a cloud field. If a large enough number of photons is simulated, their fate can be used to infer the radiative properties of the cloud field. For example, if 43% of the one million simulated photons are reflected in a simulation, the albedo of the particular cloud field can be assumed to be very close to 0.43. Since the method is based on a random simulation of individual photons, the randomness may result in slight errors. Fortunately, this statistical uncertainty is inversely proportional to the square root of the number of simulated photons; thus, it can be decreased beyond any limit by simply simulating a high enough number of photons.

A general description of the Monte Carlo approach for radiative transfer calculations can be found in Carter and Cashwell (1975) and in Marchuk et al. (1980). Detailed descriptions of Monte Carlo models built specifically to simulate shortwave radiative transfer in inhomogeneous clouds can be found in Busygin et al. (1973), Davies (1976), Wendling (1977), Bréon (1992), and Cahalan et al. (1994b).

The main advantages of the Monte Carlo method are that

- any level of accuracy can be attained,
- the method is very flexible, i.e., any cloud structure and scattering phase function can be handled easily,
- it is based on simple theory,

⁴As an exception, some studies used cloud models built of styrofoam (Davis et al. 1983; Davis and Cox 1986; Alberta and Cox 1990).

- the simulations reproduce the real flow of radiation through the cloud field, so radiative processes can be followed closely in a simple way.

As a result of these advantages, the Monte Carlo method is used widely not only to study the radiative properties of inhomogeneous clouds, but also to evaluate the accuracy of other radiative transfer calculation methods.

The main limitation of the Monte Carlo approach is that very large numbers of photons (typically in the order of hundreds of thousand or millions) must be simulated to obtain accurate results, and this requires extremely lengthy calculations. In other words, the Monte Carlo method is accurate and flexible, but very slow.⁵

Solving the equation of radiative transfer

A review of various methods to solve the equation of radiative transfer (Chandrasekhar 1960; Liou 1992) for inhomogeneous situations can be found in Gabriel et al. (1993). An updated list of such methods is presented in Table 2.2.1.

TABLE 2.2.1. Various methods to solve the equation of radiative transfer for inhomogeneous clouds

Perturbation method	Romanova (1975); Li et al. (1994b)
Modified Delta-Eddington method	Davies (1978)
6-Stream method	Gierens (1993)
Discrete angle radiative transfer	Davis et al. (1990); Gabriel et al. (1990); Lovejoy et al. (1990); Davis (1992); Barker and Davies (1992b); Lovejoy et al. (1995)
Spherical Harmonics Spatial Grid Method	Evans (1993b)
Spectral models	Stephens (1988); Gabriel et al. (1993)
Discrete ordinates method	Kobayashi (1991); Smith and Ehlert (1993)
Methods based on modifying the source term in the equation	Barker (1992); Gabriel and Evans (1996)

⁵Some methods to accelerate Monte Carlo simulations are discussed in Paltridge and Platt (1976), O'Brien (1992), Barker (1992), Evans (1993a), Cahalan et al. (1994b), and Marshak et al. (1995a).

Unfortunately, the computational requirements of these methods increase rapidly with the complexity of the cloud field. That is why most studies have presented results for somewhat simplistic cloud structures, e.g., either simple geometric clouds or irregular, but only two-dimensional variations. Barker (1996b) examined the question of how representative two-dimensional results are of 3-D clouds.

The solution of the three-dimensional radiative transfer equation presently poses great difficulties, but efficient methods to solve the equation would prove very useful in the future. One potential advantage over the Monte Carlo approach would be that the equation inherently describes the spatial distribution of the reflected radiation—a task that requires extensive calculations using the Monte Carlo technique. The obtained spatial distributions could then be used, for example, to develop new texture-based methods for the interpretation of satellite images.

Some studies (Stephens et al. 1991; Barker 1992; Evans 1993a; Malvagi et al. 1993) have taken an interesting approach to obtaining quick solutions of the radiative transfer equation. Instead of calculating the radiative properties of specific cloud fields, they have calculated the radiative transfer through fields defined only by their statistical properties. While this stochastic radiative transfer approach can be used fairly well for homogeneous and isotropic turbulence, its suitability for handling usual cloud situations such as cumulus convection is uncertain at this time.

Presently, the most accurate and versatile technique for radiative transfer calculations is the Monte Carlo method. The Monte Carlo model developed for this study is described in the following section.

2.2.2. Monte Carlo radiative transfer model

2.2.2.1 Physics of the model

This study uses a Monte Carlo model developed to calculate monochromatic and narrow-band radiative transfer through the atmosphere.⁶ The model is based on well-known principles and equations, described in detail in the references mentioned in Section 2.2.1. Besides widespread techniques, such as the use of periodic boundary conditions,⁷ the following nonstandard features have also been included into the model:

- The model can handle radiative transfer through cloud fields with irregular variations in both the cloud top height and the three-dimensional distribution of the volume extinction coefficient. Previous models either used volume extinction coefficient (VEC) variations only (and kept the geometrical thickness constant) or assumed simple geometrical cloud shapes (and kept the VEC constant).
- The clouds can be embedded into a multilayer, spherical shell atmosphere. Simulations can include the atmospheric effects of Rayleigh scattering, gaseous absorption, and aerosol scattering and absorption. The model atmosphere consists of homogeneous atmospheric layers, in which there is one layer below the clouds, one layer containing the clouds, and an arbitrary number of layers above the clouds. The layers above the clouds are assumed to be spherical shells, while the two lowest layers (below and around the clouds) are plane-parallel. Since these two layers are fairly thin in most cases, neglecting the curvature of the Earth for them does not lead to significant errors. The experiments presented in this study use a 7-layer model of atmospheric conditions over oceans at 0.443 and 0.865 μm wavelengths. The model atmosphere is based on LOWTRAN 7's OCEAN RH70, TROPO RH00 and STRT H2SO4 aerosol models (Kneizys et al. 1980) and on the empirical formula of Iqbal (1983) for the vertical distribution of the Rayleigh volume extinction coefficient.
- It can use an algorithm similar to the adding-doubling method (Liou 1992) to obtain results for any underlying surface with arbitrary reflection properties. The main advantage of the algorithm is that surface properties can be modified arbitrarily without

⁶The term "narrow-band" refers to situations where atmospheric absorption varies with wavelength, whereas scattering properties are constant throughout the spectral interval considered.

⁷The term "periodic boundary conditions" means that the cloud field is assumed to be repeated infinitely in all directions. In the model this is realized by prescribing that if a photon leaves the cloud field at one side, it reappears instantly at the opposite side.

requiring a new Monte Carlo simulation. However, since this thesis presents results only for black, non-reflecting surfaces (which might be regarded as a first-order approximation for oceans), the details of the algorithm are not discussed here.

Although virtually any physical process could eventually be included into the model, some less important effects are neglected in the present model to increase simulation speed. Thus, the main limitations of the present radiative transfer model are that

- light polarization is neglected,
- atmospheric refraction is neglected,
- ice crystals in clouds must be randomly oriented.

Some sensitivity studies have been carried out to evaluate the effects of these limitations. In typical cases, the first two effects were found to cause errors of less than a few percent. However, it was found that a systematic orientation of ice crystals could possibly alter the results significantly. This problem, though, falls outside the scope of this particular study.

Briefly described, the model handles the processes of scattering and absorption as follows.

Scattering

The model uses pre-calculated look-up tables for the quick generation of random scattering angles. These look-up tables can be created for any particle distribution as long as the particles do not have any preferred orientation. At the moment, look-up tables are available for the following cases:

- Rayleigh scattering.
- Cloud-free atmospheric layers based on model atmospheres (see above).
- Double Henyey-Greenstein phase function with parameters $g_1=0.89$, $g_2=-0.66$, $b=0.98$ (Davies 1978).
- Mie scattering at 443 and 865 nm wavelengths for the following modified gamma droplet size distributions from Welch et al. (1980): $S_{t_{base}}$, $S_{t_{top}}$, $S_{C_{base}}$, $S_{C_{top}}$, C.6 (precipitating convective cloud). The calculations were carried out using the Mie code of Bohren and Hufmann (1983).
- Randomly oriented hexagonal ice crystals from Takano and Liou (1989).
- Randomly oriented ice crystals measured by Sassen and Liou (1979).

Absorption

In order to save some computational time, the code does not lose any photons by absorption. Instead, it decreases the energy, or "weight," of each photon by the probability of it being absorbed (Paltridge and Platt 1976). The initial weight of each photon is decreased upon leaving the atmosphere by taking into account the number of scatterings it went through and the total pathlength it traveled within each atmospheric layer.

2.2.2.2 Realization of the radiative transfer model

The model was realized in the form of a FORTRAN77 code consisting of approximately 2000 lines. The computational time required for each simulation depends strongly on cloud structure and solar elevation. Using an SGI Indigo 2 computer, most experiments presented in this study took from 10 minutes to 5 hours per million simulated photons.

The model uses an equidistant rectangular grid to record the angular distribution of reflected and transmitted radiation. The coordinates of this grid are the relative azimuth (φ) and the cosine of the viewing zenith angle (μ). Most experiments used a $10^\circ \times 0.04$ resolution.

For greater flexibility, the Monte Carlo code itself does not provide results in radiation units; its only output is how many photons go into each angular bin. Then a separate program "calibrates" the results, i.e., transforms the photon numbers into radiance (I), reflectance (also called Bidirectional Reflectance Factor or BRDF), or Bidirectional Reflectance Distribution Function (BRDF) values, using the following equations:

$$I_{(\mu,\varphi)} = \frac{\mu_0 S_0}{\mu \omega_{bin}} \frac{N_{(\mu,\varphi)}}{N_{total}}, \quad (2.2.1)$$

where $N_{(\mu,\varphi)}$ is the number of photons going to the bin at (μ,φ) , N_{total} is the total number of simulated photons and ω_{bin} is the solid angle covered by each bin, equal to $\frac{4\pi}{N_{bins}}$ (N_{bins} being the total number of angular bins);

$$BRF_{(\mu,\varphi)} = \frac{\pi I_{(\mu,\varphi)}}{\mu_0 S_0}; \quad (2.2.2)$$

$$BRDF_{(\mu,\varphi)} = \frac{BRF_{(\mu,\varphi)}}{A}, \quad (2.2.3)$$

where A is the scene albedo. A $BRF_{(\mu,\varphi)}$ value indicates what the albedo would be if the scene were a Lambertian reflector with $I = I_{(\mu,\varphi)}$ for all directions. $BRDF_{(\mu,\varphi)}$ describes the factor by which the real albedo of the scene would change if it reflected $I = I_{(\mu,\varphi)}$ in all directions. (The albedo would not change if $BRDF_{(\mu,\varphi)} = 1$, but it would double if $BRDF_{(\mu,\varphi)} = 2$, etc.) The main advantage of using the BRF is that its values are normalized to the intensity of the solar illumination, while the BRDF is useful in describing the direction to which the reflected radiation goes.

As mentioned in section 2.2.1, the Monte Carlo method does not give exact numbers, only a statistical approximation of the correct result. The standard deviation of the albedo values obtained by subsequent Monte Carlo simulations for the same scene (hereafter referred to as statistical uncertainty or σ) can be calculated using the formula (Davies 1978)

$$\sigma_A = \left[A (1 - A) N_{phot}^{-1} \right]^{1/2}. \quad (2.2.4)$$

The uncertainty of radiance, BRF and BRDF values can be estimated using the following three-step procedure:

1. The uncertainty is estimated using the equation of binomial distribution:

$$\sigma_{(\mu,\varphi)} = \left[P_{(\mu,\varphi)} (1 - P_{(\mu,\varphi)}) N_{phot}^{-1} \right]^{1/2},$$

where $P_{(\mu,\varphi)}$ is the probability that a simulated photon would end up in the angular bin (μ,φ) . Using 36×50 angular bins (which give a $10^\circ \times 0.04$ resolution) and simulating 4 million photons, this uncertainty for a bin at $\mu = 0.5$ with $BRF_{(\mu,\varphi)} = 0.5$ equals 1.178×10^{-5} .

2. The uncertainty in terms of photon numbers is calculated by multiplying the result of Step 1 by the total number of simulated photons. In the given case, this means that instead of the correct number of 2222 photons, about 47 photons more (or less) could go to the angular bin in question.
3. The uncertainty is "calibrated," i.e., transformed from photon numbers to radiation units, by using equations (2.2.1) - (2.2.3). In the mentioned case the uncertainty in BRF units is about 0.0106.

A few experiments were carried out in order to test whether or not the procedure described above gives correct estimates of the statistical uncertainty. In each experiment, 100 Monte Carlo simulations (each using a different random number seed value) were carried out for a homogeneous and an inhomogeneous cloud field. Then the standard deviation of the 100 nadir reflectance values was compared with the theoretically expected uncertainties. From the results shown in Table 2.2.2, one can conclude that the theoretical formulas work well for both homogeneous and inhomogeneous cloud fields.

TABLE 2.2.2. Monte Carlo uncertainties for 100 homogeneous plane-parallel and inhomogeneous cloud fields

Experiment	Theoretical uncertainty	Experimental result
P-p cloud, $\tau = 10$, $N_{\text{phot}} = 10^5$	0.0276	0.0267
P-p cloud, $\tau = 10$, $N_{\text{phot}} = 10^6$	0.0087	0.0082
P-p cloud, $\tau = 6$, $N_{\text{phot}} = 10^5$	0.0217	0.0221
3-D cloud, $N_{\text{phot}} = 10^5$	0.0210	0.0193

In most experiments of the present study, the statistical uncertainties were decreased by a factor of $2^{1/2}$ by a simple symmetric averaging of the obtained photon numbers over the solar plane.

An important part of the model development was to ensure that the code is free of any hidden errors. Hence, the model was verified using the following tests:

- Plane-parallel albedos were tested against results obtained using the Discrete Ordinates Method. Some comparison results are shown in Table 2.2.3.
- Results for simple cloud geometries (cubes, etc.) were compared to results reported in the literature. Examples for these comparisons are shown in Table 2.2.4.
- The azimuthal symmetry of results was tested for appropriate cloud geometries.
- Updated versions of the code were tested thoroughly to give the same results as the preceding versions.
- All results were checked for qualitative consistency with previous results.

TABLE 2.2.3. Comparison of plane-parallel albedos obtained using Monte Carlo (MC) simulations and the discrete ordinates method (DOM). The Monte Carlo experiments simulated 1,000,000 photons, hence the statistical uncertainty of results is 0.0004 - 0.0005.

τ	DOM	MC
SZA = 0°		
5	0.2294	0.2290
10	0.4047	0.4047
30	0.6997	0.6995
SZA = 60°		
5	0.4460	0.4455
10	0.5916	0.5914
30	0.7956	0.7958

TABLE 2.2.4. Comparison of fluxes obtained for cuboidal and cylindrical clouds with values reported in previous studies

Case	Result in literature	Present study	MC uncertainty
Cuboidal cloud, $\tau = 50^*$			
SZA = 0°			
Albedo	0.6341	0.6312	0.0031
Flux through cloud top	0.4088	0.4041	0.0031
Flux through cloud base	0.0208	0.0209	0.0009
SZA = 60°			
Albedo	0.5257	0.5243	0.0032
Flux through cloud top	0.2450	0.2471	0.0027
Flux through cloud base	0.1266	0.1268	0.0021
Cylindrical cloud, $\tau = 49^{**}$			
SZA = 0°			
Flux through cloud top	0.391	0.3897	0.0015
Upward flux through side	0.233	0.2360	0.0013
Downward flux through side	0.361	0.3592	0.0015
Flux through cloud base	0.015	0.0150	0.0004

SZA = solar zenith angle

MC = Monte Carlo

* Davies (1976)

** Bréon (1992)

Chapter 3

Shortwave Radiative Transfer in Inhomogeneous Cloud Fields

One of the main goals of this thesis is to study the processes through which cloud inhomogeneities affect solar radiation. In previous studies, radiative effects of cloud inhomogeneities have been described with numerous terms and expressions, such as "channeling," "plane-parallel albedo bias," "side illumination," "increased backscatter from illuminated cloud sides," "cloud-cloud interactions," "mutual shadowing," "side-leakage," etc. However, these terms do not give full descriptions of the mechanisms through which inhomogeneities influence cloud radiative properties. As a result, there has been no way to tell the degree to which various mechanisms are responsible for the overall inhomogeneity effect. Specifically, the main problems are that

- Most terms have been used only in a qualitative sense, without exact definitions. Thus the magnitudes of various effects could not be quantified.
- Many definitions are appropriate only for special cloud geometries. For example, the term "side illumination" could be interpreted easily for cuboidal or cylindrical clouds, but it is not so obvious exactly where the sides of a cumulus cloud end and the top begins.
- The various terms describe only some individual aspects of radiative transfer in inhomogeneous clouds, but they do not form coherent systems that would explain the overall effects of cloud inhomogeneities. For example, the plane-parallel albedo bias (Cahalan et al. 1994b, 1995; Barker 1996a; Oreopoulos 1996) addresses the fact that the cloud layer which solar radiation reaches has areas where clouds are thicker and thinner than average. However, there are no corresponding definitions for the effects that complement this bias by influencing radiation once it is within the cloud layer.

Thus, the first problem addressed in this chapter is how inhomogeneity effects can be defined in an exact and coherent way. Section 3.1 describes a set of definitions developed for this purpose. The main advantages of the proposed system are that

- It reflects the physical processes through which cloud inhomogeneities influence shortwave radiation.
- It is based on unambiguous, quantitative definitions that are easy to calculate.
- Its individual inhomogeneity effects complement each other without overlap, i.e., they can simply be added up to obtain the overall inhomogeneity effect.
- It can be used for any irregular cloud fields. Any inhomogeneities—for example, internal volume extinction coefficient variations and the effects of cloud brokenness—can be handled within a unified framework.

The new scheme is then used to explore the processes through which cloud inhomogeneities affect solar radiation. In particular, it examines how irregular cloud top height variations influence solar radiation, and how their influence compares to the effects of volume extinction coefficient variations. This important question has not yet been addressed, since earlier studies either used simple cloud geometries (such as cubes), or attributed all τ -variations to changes in the volume extinction coefficient, and kept the geometrical cloud thickness constant (Davis et al. 1990; Gabriel et al. 1990; Barker and Davies 1992a; Davis 1992; Cahalan et al. 1994b; Barker and Liu 1995; Marshak et al. 1995a, 1995b; Gabriel and Evans 1996). While the assumption of a constant cloud top height may be appropriate for stratocumulus clouds, it certainly is not for many cumulus cloud fields. The proposed scheme is also used to investigate whether cloud inhomogeneities may be responsible for the unexpected fact that observed nadir reflectance is larger for oblique than for overhead sun (Loeb and Davies 1996b).

3.1 Definitions of Shortwave Radiative Inhomogeneity Effects

Numerous studies have shown that the shortwave radiative properties of inhomogeneous cloud fields can be very different from those of homogeneous, plane-parallel layers (Section 1.2). Here it is proposed that the differences (i.e., the radiative effects of cloud inhomogeneities) should be separated into two main components.

The first component is that solar beams (photons) entering inhomogeneous fields encounter clouds of various thicknesses; some beams may pass through the cloud layer

without hitting a single droplet, while other beams may have to "fight" their way through thick clouds. Due to the nonlinear nature of radiative transfer, this variation in encountered cloud thickness influences not only local, but also scene-average radiative properties. For example, it is well-known that (in the absence of absorption) the average of a thin and a thick cloud's albedo is lower than the albedo of a cloud with their average optical thickness (Figure 3.1.1). The first component (that photons enter clouds of various thicknesses) then modifies the overall radiative properties of a cloud layer even if these photons do not experience inhomogeneity effects once they enter the clouds. Since this effect can be described using one-dimensional radiative transfer theory, it can be called the *1-D inhomogeneity effect* (1-D IH effect).

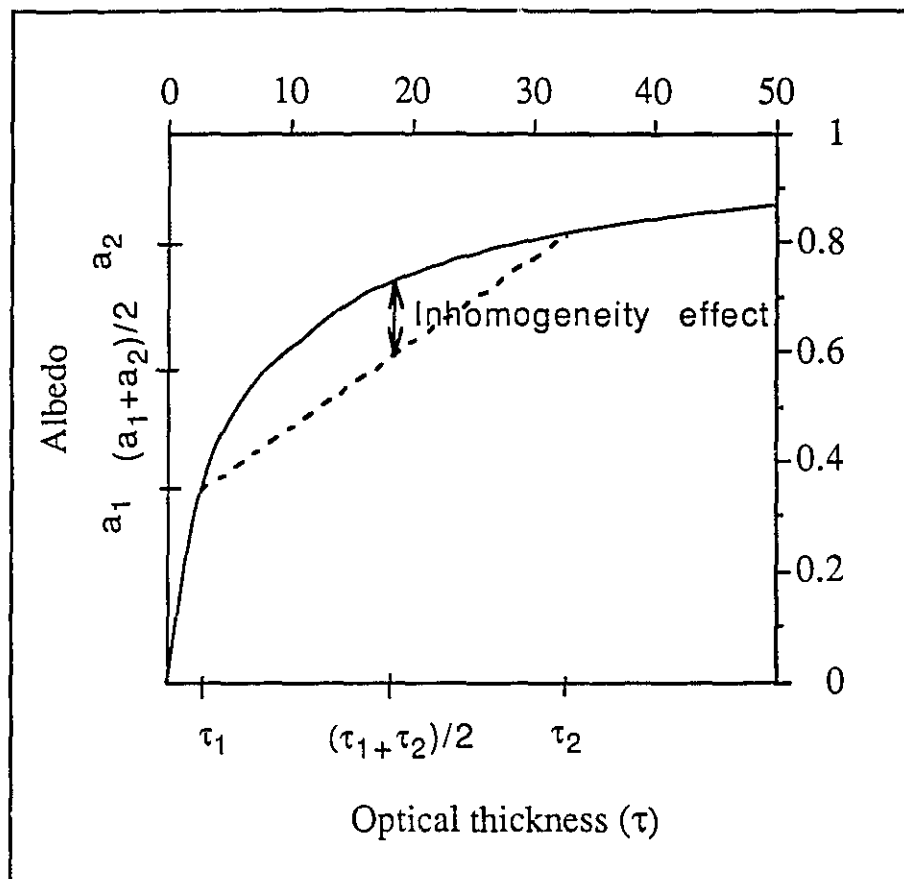


Figure 3.1.1. 1-D inhomogeneity effect. The solid line indicates the albedo of a plane-parallel cloud for 60° solar zenith angle. The dashed line connects the albedos of a thin and a thick cloud.

The second component of the overall inhomogeneity effect is the way photons are affected by inhomogeneities they may encounter once they enter the cloud field. Since this effect can be described only within a three-dimensional framework, this second component can be referred to as the *3-D inhomogeneity effect* (3-D IH effect).

Thus the 1-D effect addresses the fact that photons reach the cloud at locations of various optical thicknesses, whereas the 3-D effect, that these photons may actually encounter more or fewer droplets than their point of entry would suggest, because multiple scattering changes their course. In this section, the separation of the overall influence of cloud inhomogeneities into 1-D and 3-D components is used to develop a system of quantitative definitions for various inhomogeneity effects. Section 3.1.1 describes the 1-D effect in detail, and Section 3.1.2 deals with the 3-D effects.

3.1.1 One-dimensional inhomogeneity effect

For overhead sun, one can calculate how the 1-D IH effect influences cloud albedo by using the Independent Pixel Approximation (IPA) (Cahalan et al. 1994).¹ The main assumption of the IPA is that neighboring cloud pixels have no radiative interactions, and thus can be treated individually. Hence the main advantage of this widely used approximation is to allow fast 1-D radiative calculations for any inhomogeneous cloud fields.

For oblique sun, however, the IPA cannot describe the 1-D IH effect accurately, because it assumes that each solar beam (or photon) remains within the pixel at which it reached the cloud layer. While this assumption is appropriate for overhead sun, it can lead to large biases as soon as the sun moves away from zenith. For example, the IPA would estimate a strong 1-D IH effect for the case shown on Figure 3.1.2a, since it assumes that half of the solar beams pass through the cloud layer without hitting a single droplet, and the other half encounter fairly thick clouds. In reality, however, none of the photons can pass through the layer without entering a cloud. Therefore, the IPA overestimates the influence that the photons' initial position has on whether they get reflected or transmitted, and thus overestimates the 1-D IH effect (Figure 3.1.2/b).

¹The same approximation has been used under various names by Schmetz (1984) and Kobayashi (1991).

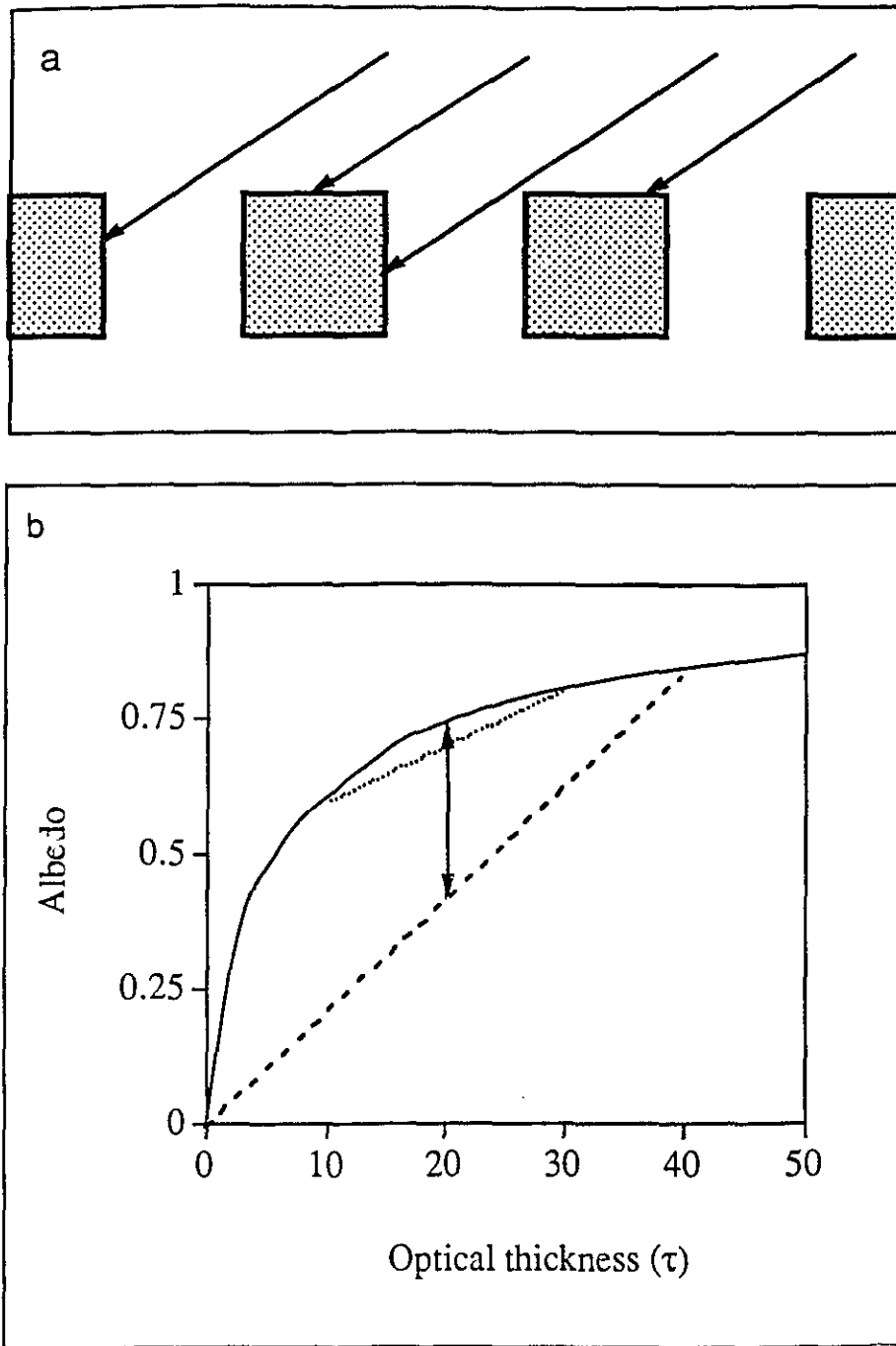


Figure 3.1.2. Influence of cloud variability on the 1-D IH effect: (a) The IPA overestimates the 1-D IH effect for oblique sun over an area of cuboidal clouds; (b) The 1-D IH effect is strong if the photons' initial position has a large influence on their chance of being reflected (for ex., 0% or 84% along the dashed line), whereas it is weaker if the initial position has a smaller influence (for ex., 61% or 80% along the dotted line).

Although Barker (1992) and Gabriel and Evans (1996) constructed various methods to correct the IPA's biases for oblique sun, they focused on obtaining accurate numerical results for the overall cloud reflection rather than calculating any 1-D IH effects. In this section, a simple method is proposed for the calculation of the 1-D IH effect, and then this method is compared to various approximations used in previous studies.

Calculating the 1-D IH effect

As defined above, the 1-D IH effect describes how radiative transfer is affected by the fact that various solar beams reach the cloud layer at locations of different thicknesses. It is not difficult to calculate this effect in the middle of large homogeneous areas. For example, it is easy to see that beam *C* on Figure 3.1.3 encounters a cloud with $\tau = 50$, while beam *A* goes through an area with $\tau = 0$. However, the problem is not so straightforward for beams that reach the cloud layer near inhomogeneities. The IPA assumes that beams *A*, *E* and *F* encounter no clouds at all, while beams *B*, *C* and *D* go through very thick clouds. Consequently, the approximation introduces dramatic differences between beams *A* and *B*, and between *D* and *E*, even though in reality photons in the same beam pair experience the cloud layer very similarly.² The initial locations of beams *A* and *B*, and beams *D* and *E* cause both members within each beam pair to behave fairly similarly to one another. These similarities should be reflected in calculating the 1-D IH effect, and they can be if the initial position of each beam is considered to predetermine that it will encounter a cloud of optical thickness τ^* , defined as

$$\tau_{\Omega}^* = \beta L_{\Omega} \cos \theta_0, \quad \Omega = A, B, C, D, E, F$$

where L_{Ω} is the geometrical length of each beam's interception with the cloud and β is the VEC. This equation can be generalized to any irregular cloud:

$$\tau_{\Omega}^* = \int_{z_{bottom}}^{z_{top}} \beta(x_{(z)}^*, y_0, z) \cos \theta_0 dL = \int_{z_{bottom}}^{z_{top}} \beta(x_{(z)}^*, y_0, z) dz, \quad (3.1.1)$$

where z_{bottom} and z_{top} are the altitudes at the bottom and top of the cloud layer, $x_{(z)}^* = x_0 - (z - z_{top}) \tan \theta_0$, and (x_0, y_0) indicates the point where a beam Ω enters the cloud

²The IPA also assumes that the cloud layer affects the photons in beams *E* and *F* the same way, whereas in reality, it is more likely to reflect photons in beam *E*. (The situation is similar for beams *B* and *C*.)

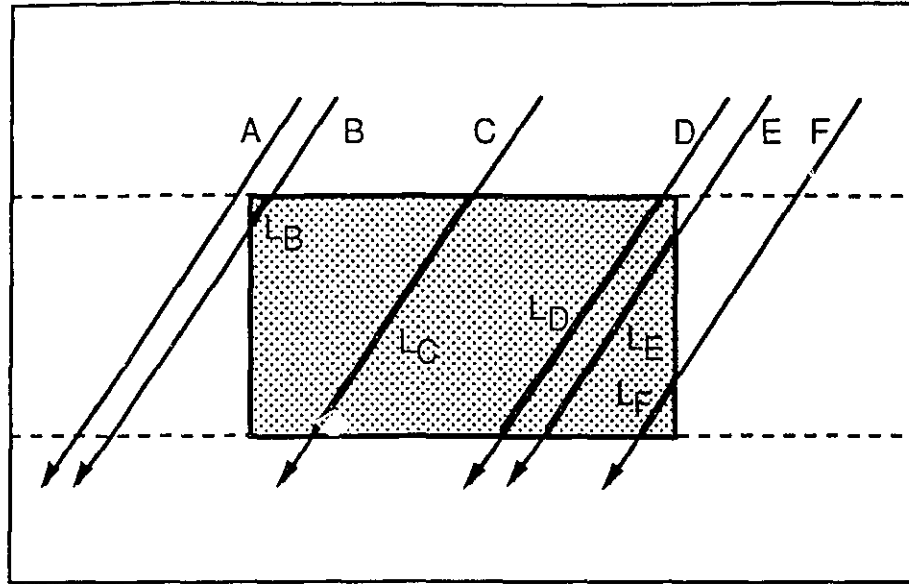


Figure 3.1.3. Solar beams passing through an inhomogeneous cloud layer which lies between altitudes z_{top} and z_{bottom} . L is the geometrical length of each beam's interception with the cloud. The τ optical thickness of the cuboidal cloud is 50.

layer in a direction perpendicular to the y -axis. Then the total 1-D IH effect for an entire scene can be calculated from the equation

$$Eff_{1-DIH} = \langle A_{[\tau_{(x,y)}^*]} \rangle - A_{(\tau)}, \quad (3.1.2)$$

where $A(\tau)$ is the albedo of a plane-parallel cloud with τ optical thickness, and $\langle \rangle$ indicates averaging over an entire scene. The first term in the right hand side of this equation can be calculated in two steps. First, the spatial distribution of τ^* values should be calculated, and then the appropriate albedos can be obtained much as in the IPA, with τ^* substituted for τ . Since the τ^* values are optical thicknesses of thin columns tilted toward the sun, and since the interactions of the tilted columns are not considered in the 1-D IH effect, the calculation of the first term on the right side of equation (3.1.2) can be called Tilted Independent Pixel Approximation (TIPA). Various algorithms developed for

calculations based on the TIPA are presented in Appendix A. Although not specified in equations (3.1.1) and (3.1.2), the effects of variations in microphysical cloud properties (i.e., phase function, single scattering albedo and gaseous volume absorption coefficient) can also be included into the calculations by replacing $A_{(\tau^*)}$ (the albedo of a single homogeneous cloud layer) by A^* (the albedo of a plane-parallel cloud with vertical inhomogeneities) (Figure 3.1.4).

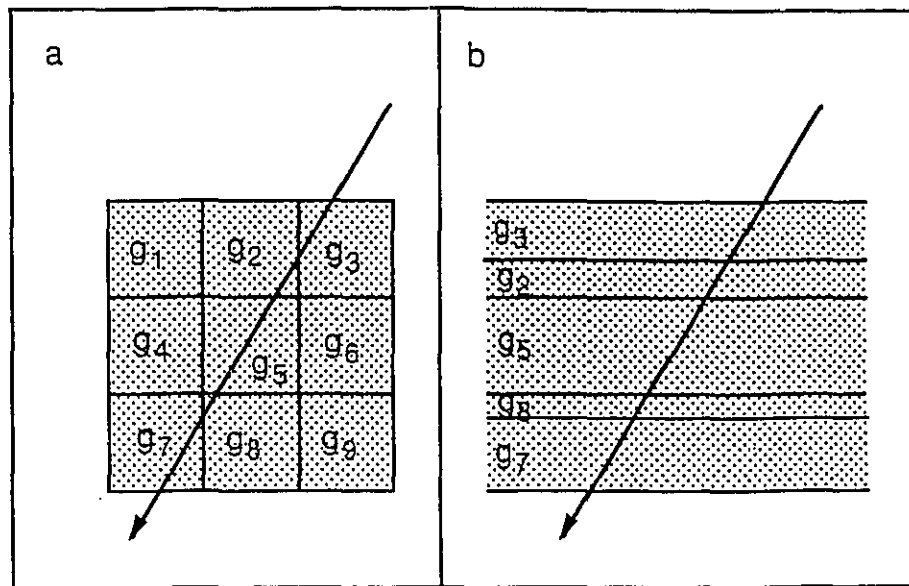


Figure 3.1.4. Microphysical variations in the TIPA: (a) the real cloud with variable phase function asymmetry factor (g_1, g_2, \dots, g_9); (b) the plane-parallel cloud which the beam is assumed to encounter in the TIPA .

The 1-D IH effect's influence on radiance values can be calculated by simply replacing the albedo $A(\tau)$ with the radiance $I_{(\tau, \mu, \varphi)}$. The influence on the spatial distribution of reflected radiation can be calculated using the equation

$$Eff_{1-D IH}(x, y, \mu, \varphi) = \int_0^x \int_0^y I_{(\tau^*(x_0, y_0), x-x_0, y-y_0)} dy_0 dx_0 - I_{((\tau))} , \quad (3.1.3)$$

where X and Y are the horizontal domain sizes in x and y directions, and $I(\tau^*_{(x_0, y_0)}, x - x_0, y - y_0)$ is the radiation that is reflected by a plane-parallel cloud of thickness τ^* at a distance $(x - x_0, y - y_0)$ from the point where it entered the cloud. (This can be determined from plane-parallel Monte Carlo simulations.) It should be noted that even for overhead sun, this equation gives results different from the spatial distributions estimated by the IPA. In estimating local radiances, the IPA assumes not only that the entry point determines the way a photon experiences a cloud, but also that photons do not move horizontally, not even as they would in a plane-parallel cloud. Equation (3.1.3), on the other hand, allows for horizontal flow of radiation as long as individual photons are not affected by horizontal inhomogeneities along their paths. Therefore this equation is more suitable for estimating the 1-D IH effect even for overhead sun. (This does not necessarily imply that equation (3.1.3) would give more accurate estimates for local radiances than the IPA would, since real radiances are influenced by 3-D effects as well.)

Comparison of the TIPA to various other approximations

In this section, the TIPA is compared to three other approximations: a type that uses an apparent cloud fraction (CF_{app}), the IPA, and an approach that treats direct and diffuse radiation separately.

As Minnis (1989) shows, clouds in broken cloud fields appear to occupy increasing portions of a scene as it is viewed from increasingly oblique angles. The cloud fraction apparent from the sun's direction has been used in radiative studies (Aida 1977; Davis et al. 1979; Harshvardhan and Thomas 1984; Kobayashi 1988; Titov 1990; Barker 1994).³ The TIPA is closely related to this CF_{app} , since both calculate the fraction of the incoming solar radiation that is intercepted by clouds. However, while the CF_{app} distinguishes between only two categories (cloud or no cloud), the TIPA also takes into account the effects of cloud optical thickness variations. Therefore the TIPA can be regarded as an extension of CF_{app} .

³The effective cloud fraction has also been used in studies of infrared radiation (Killen and Ellingson 1994).

Although some differences between the IPA and the TIPA were pointed out earlier in this section, some further comparisons may also be of interest. The fundamental difference between the two approximations can also be described in terms of the distribution of incoming solar radiation: the IPA assigns equal amounts to all horizontal unit areas, whereas the TIPA assigns equal amounts to all unit areas perpendicular to the incoming solar radiation. An analogy can be drawn between this difference and the reason the earth's poles are colder than the equator (Figure 3.1.5). This fundamental difference results in the TIPA being able to explain qualitatively why cloud reflection properties depend not only on the frequency distribution of cloud optical thicknesses (as assumed by the IPA), but also on the spatial distribution of τ -values. For example, the TIPA enables explanations of why windshears toward and away from the sun result in different radiative effects (Barker 1994), or why cloud streets parallel and perpendicular to the solar illumination have different albedos (Davies 1976 p. 137).

Although the main purpose of the TIPA is to calculate the 1-D IH effect (as opposed to obtaining quick albedo estimates), it might still be of some value to compare albedo estimates obtained by the TIPA and the IPA. By definition, the two approximations give identical scene-average albedo values for overhead sun. For oblique illumination, the calculation of τ^* values smoothes the original τ values in the x -direction. This smoothing results in τ^* having less variability than the original τ values, and thus causes TIPA albedos to be somewhere in between the albedos calculated using the IPA and the homogeneous, plane-parallel approximation. Since the IPA always gives lower albedos than the homogeneous, plane-parallel assumption (Figure 3.1.1), it follows that TIPA albedos are always higher than IPA albedos. For small solar zenith angles even the IPA tends to overestimate the real albedo, and so the higher TIPA-estimates are even further from the correct albedos. For large solar zenith angles, however, the IPA underestimates the true albedo, and thus the TIPA estimates are more accurate (Figure 3.1.6).

Finally, the TIPA can also be compared to an interesting approach taken by Barker (1992) and Gabriel and Evans (1996). They applied conventional 1-D theory to describe diffuse radiation, whereas they designed various methods to acknowledge that the direct beam penetrates deeper into inhomogeneous cloud fields than into homogeneous clouds. In the present case, as in the Independent Pixel Approximation, Modified Source (IPAMS) in Gabriel and Evans (1996), the direct and diffuse radiation can be separated, assuming that the direct beam is tilted according to the solar elevation, while the diffuse radiation

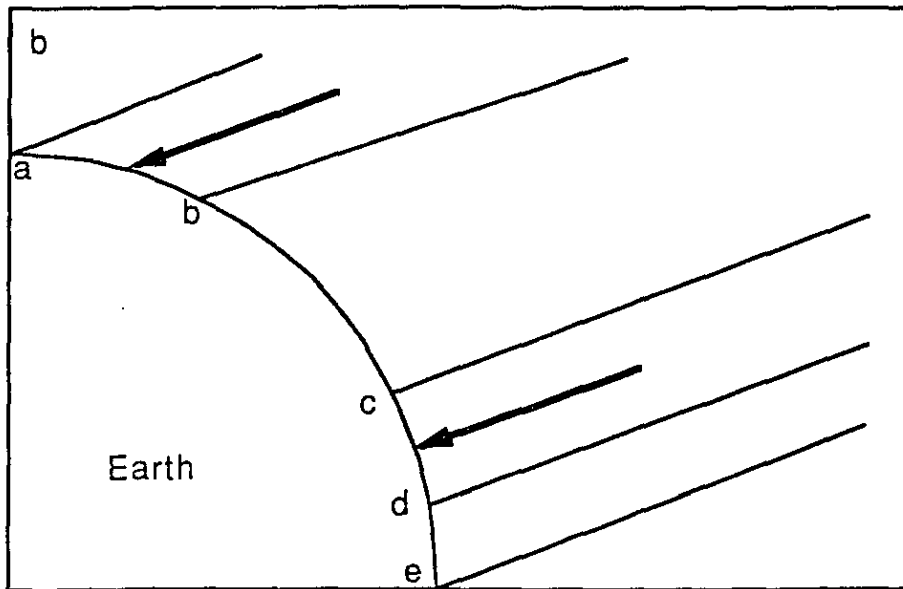
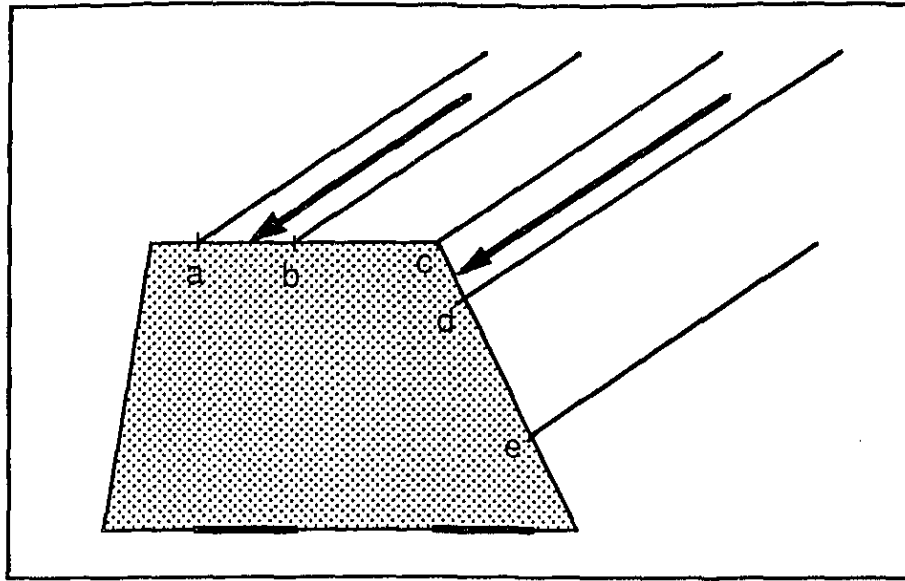


Figure 3.1.5. Analogy between IPA-TIPA and equator-pole differences: (a) The IPA assigns equal amounts of solar radiation to intervals [a,b] and [c,e], whereas the TIPA assigns equal amounts to [a,b] and [c,d]; (b) On the Earth's surface, interval [c,d], and not [c,e], intercepts as much solar radiation as interval [a,b].

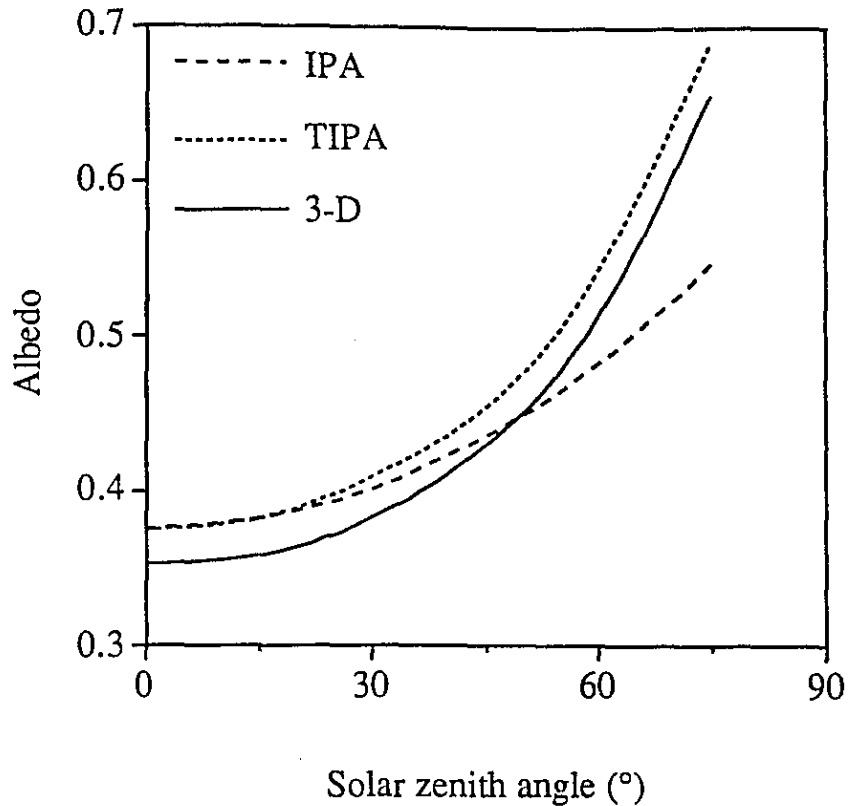


Figure 3.1.6. Accuracy of albedo estimates based on the IPA and the TIPA for the cloud field shown in Figure 2.1.1.

propagates in the vertical direction. Thus, the logic of this approach lies somewhere between that of the IPA (which assumes that all radiation moves vertically) and the TIPA (which assumes that all radiation moves in a tilted direction). The scene albedo can be estimated by using this separation approach to calculate where each photon is first scattered, and then replacing τ or τ^* in IPA or TIPA calculations by the optical thickness of the column below this scattering point. This approximation gives the same results as the TIPA on the sunlit side of a cuboidal cloud, and the same results as the IPA on the shadowy side. Therefore, while this separation approach can be useful for many purposes, the artificial jump at the shadowy cloud edge makes it as unsuitable for estimating the 1-D IH effect as the IPA. (Another problem would arise in the case of a thin overlying Cirrus cloud. Since most photons are scattered only once or twice in such

clouds, they tend to reach the underlying inhomogeneous cloud layer in oblique directions. The separation approach, like the IPA, however, assumes that the photons reach the inhomogeneous layer vertically. Hence, this approach would overestimate the 1-D IH effect for such situations.)

While the TIPA may also be useful for purposes other than calculating the 1-D IH effect, one should not forget about the limitations of its use for other purposes. One main limitation is that since the TIPA is designed for forward calculations, it is highly questionable whether it could be used in satellite retrievals. Another important limitation is that, by definition, it does not include 3-D effects, and thus it cannot estimate phenomena that are not present in 1-D radiative transfer theory. For example, the TIPA cannot give accurate estimates for the angular distribution of radiation reflected from broken cloud fields, since the enhanced backscatter from cloud sides (Davies 1976, p. 127; Wendling 1977) is not present in 1-D theory. This problem can be solved only by considering 3-D radiative effects. The following section describes a way these effects can be defined and calculated.

3.1.2 Three-dimensional radiative inhomogeneity effects

The main purpose of this section is to develop definitions for radiative inhomogeneity effects that cannot be included into a 1-D framework. By definition, the 1-D IH effect describes the aspect of radiative transfer, that photons reach the cloud layer at locations which have various thicknesses. The 3-D effects, on the other hand, describe the various ways individual photons are affected by cloud inhomogeneities they encounter along their paths within the cloud layer. These inhomogeneities can affect a photon in one of two ways:

- It is scattered (and / or absorbed) further in the inhomogeneous cloud even after it would have left a homogeneous cloud, or
- It leaves the cloudy layer "too early," i.e., when it would still be well within a homogeneous cloud.⁴

⁴The time t a photon spends in the cloud layer can be determined from the distance it travels within the layer, using $t = \frac{1}{c} \int_{r_0}^{r_{leaving}} dr$, where r_0 and $r_{leaving}$ are the coordinates of the points where the photon enters and leaves the cloud layer, respectively, and c is the speed of light. (The integration should be performed along the photon's path, instead of along a straight line connecting r_0 and $r_{leaving}$.) However, changing t does not necessarily affect whether it gets transmitted, reflected, or absorbed. For example, if the

Since in both cases, the affected photons can leave the cloud layer either upward or downward, four main inhomogeneity effects can be defined. These are:

- A. The photon does not leave the cloud layer upward when it would in the case of a homogeneous cloud, but instead experiences further scattering (and / or absorption). In the case of clouds with constant microphysical properties and no gaseous absorption, this scattering (and / or absorption) occurs when the radiation travels through more τ upward than it did before downward (Figure 3.1.7a). Since this *upward trapping* effect makes it more difficult for radiation to leave upward, it tends to decrease cloud albedo.⁵
- B. The photon does not leave the cloud layer downward when it would in the case of a homogeneous cloud, but instead experiences further scattering (and / or absorption). In the case of clouds with constant microphysical properties and no gaseous absorption, this occurs if the radiation descends through more τ than it would be required to in order to be transmitted through a homogeneous cloud (Figure 3.1.7b). Since this *downward trapping* effect makes transmission of radiation more difficult, it tends to increase cloud albedo.
- C. The photon leaves the cloud layer upward "too early," i.e., when it would still be well within a homogeneous cloud. In the case of clouds with constant microphysical properties and no gaseous absorption, this occurs if the radiation leaves upward after having traveled through more τ downward than upward (Figure 3.1.7c). Since this *upward escaping* effect allows reflected radiation to leave upward more easily, it tends to increase cloud albedo.⁶

geometrical thickness of a homogeneous, non-absorbing cloud were increased, and its volume extinction coefficient were decreased to keep the optical thickness constant, all photons would still reach the same fate (either reflection or transmission) in the new cloud, even though they would all spend more time in the cloud layer. Consequently, the terms "after," "too early," and "when" do not refer to the time photons spend within the cloud layer, but to the overall optical pathlength $PL = \int_{r_0}^{r_{leaving}} \beta_{(r)} dr$ they travel

through. It is this optical pathlength PL that determines both the number of scatterings a photon experiences, and its chances of being absorbed. Thus, the expressions "after" and "too early" should be interpreted as "having traveled through a larger (or shorter) total optical pathlength."

⁵Special cases for the upward trapping effect have been described (under various names, for example "side illumination") by Wendling (1977) and Kobayashi (1993).

⁶For simple cloud geometries, the increase in reflection in oblique directions (due to the upward escaping effect) has been described by Davies (1978), Kobayashi (1993).

- D. The photon leaves the cloud downward "too early," i.e., when it would still be well within a homogeneous cloud. In the case of clouds with constant microphysical properties and no gaseous absorption, this occurs if the radiation can escape the cloudy layer downward after having traveled through less τ than would be required in a homogeneous cloud (Figure 3.1.7d).⁷ Since this *downward escaping* effect makes it easier for radiation to pass through the cloud layer, it tends to decrease cloud albedo.

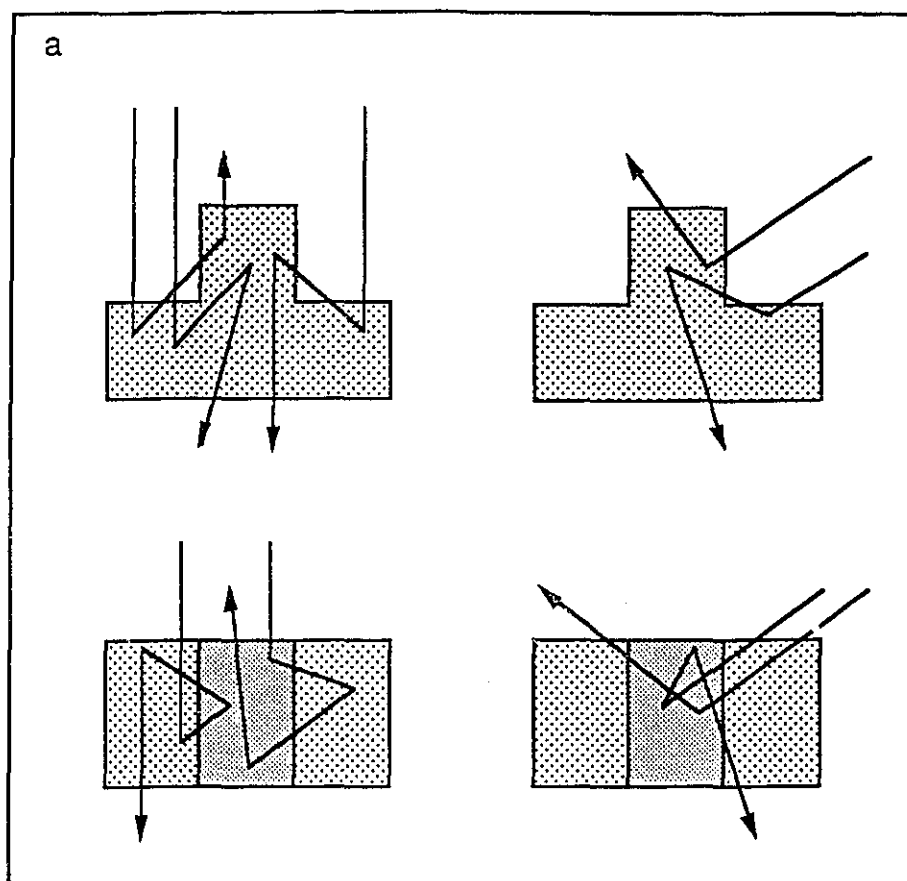
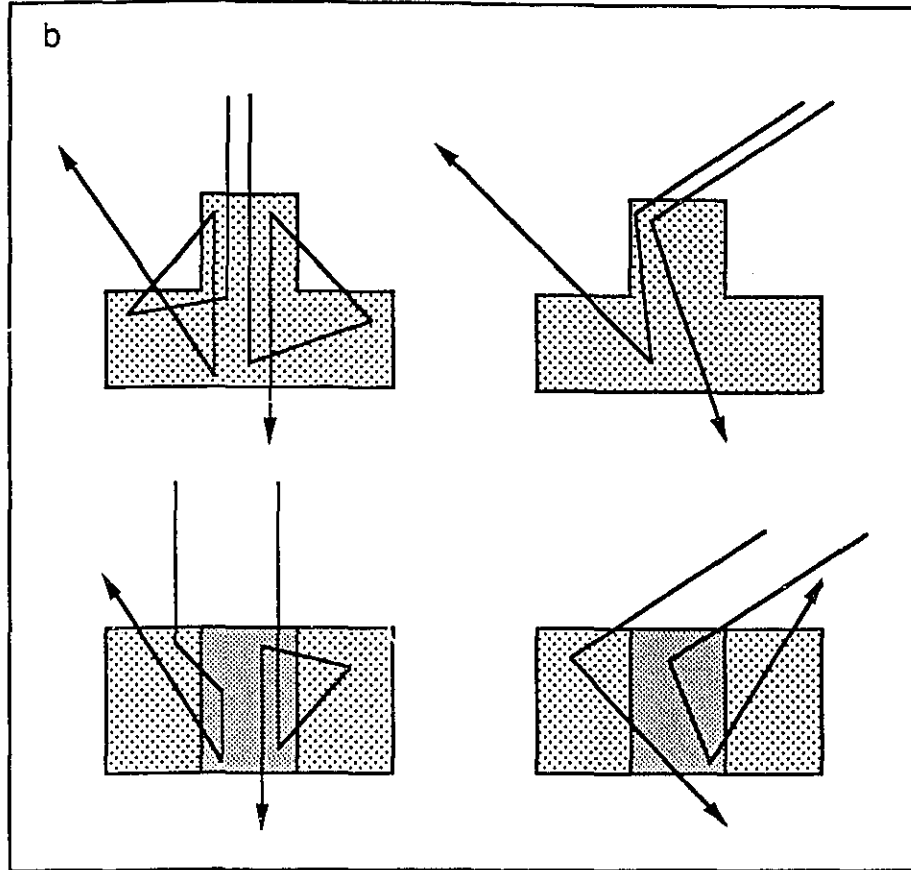
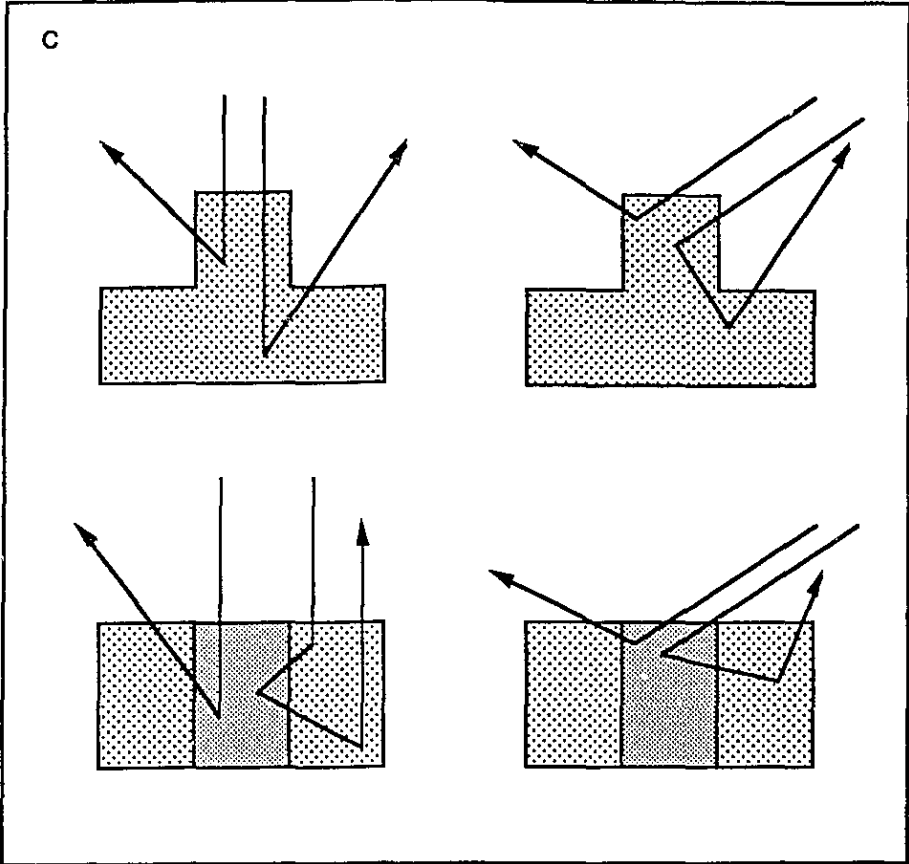
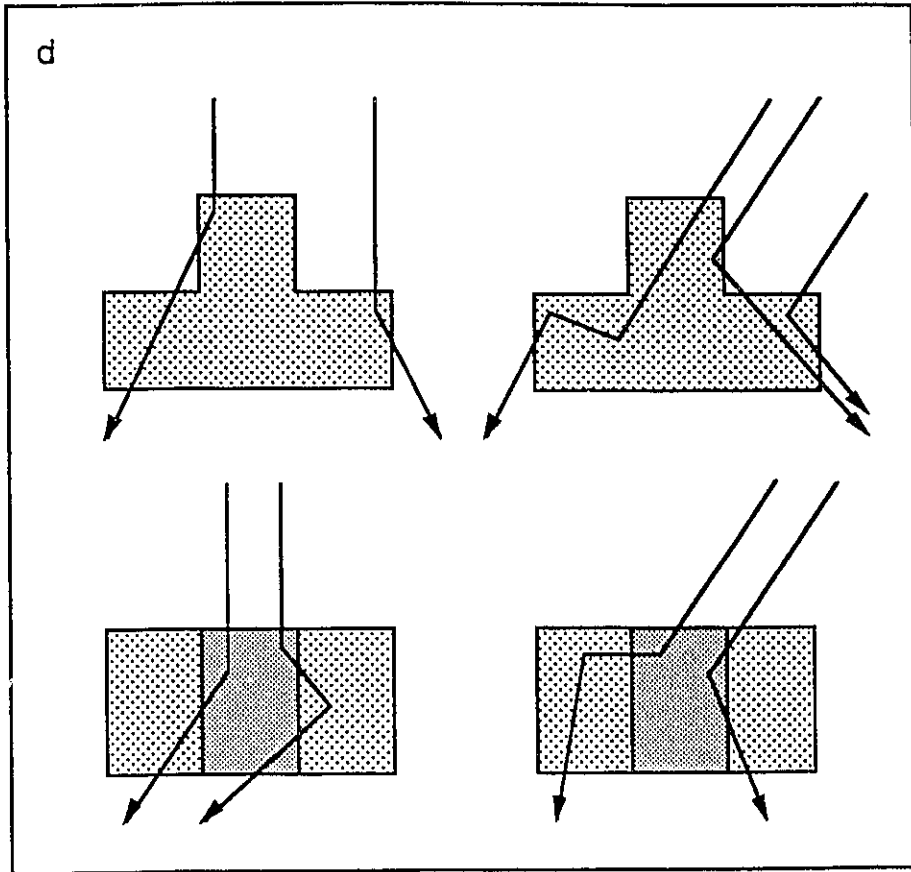


Figure 3.1.7. Paths of photons that experience 3-D IH effects in clouds having cloud top height and volume extinction coefficient variations: (a) upward trapping; (b) downward trapping; (c) upward escaping; (d) downward escaping. Denser shading indicates higher volume extinction coefficient.

⁷For plane-parallel clouds with horizontally variable VEC, Cannon (1970) named this effect channeling.







One can obtain the *overall 3-D IH* effect simply by adding up these four effects. Then the overall radiative effect of cloud inhomogeneities can be obtained by adding the 1-D IH effect and the overall 3-D effect.

Since some photons influenced by 3-D IH effects may end up the same way as they would have in a homogeneous cloud (Figure 3.1.8), one should distinguish between the amount of radiation affected by 3-D IH effects and the net influence of these effects. Both quantities can be determined through three subsequent Monte Carlo experiments that simulate what happens to the very same photons if 3-D IH effects are taken into account and if they are not. The first simulation predicts the $\tau_{(r_0)}^*$ values each photon will encounter in the 3-D field.⁸ The second one calculates radiative transfer based on the TIPA, assuming a plane-parallel cloud of thickness $\tau = \tau_{(r_0)}^*$ (chosen separately for each photon, according to the results of the first simulation). Finally, the third simulation calculates radiative transfer through the actual 3-D cloud field. A simple procedure can ensure that all three experiments simulate the very same photons in their respective cloud fields: setting the random number generator seed to identical values before simulating the paths of corresponding photons in the three experiments.⁹ This ensures that the generated pathlengths (in optical thickness units) and scattering angles are identical in both simulations. (The scattering angles generated using identical random numbers may be somewhat different in the TIPA and the 3-D calculations, if there are variations in the microphysical cloud properties. Nonetheless, the two experiments simulate the path of identical photons in their respective cloud fields, since the very same photons can be scattered differently, depending on the size of the droplets they encounter.)

The above method examines how photons are influenced by inhomogeneities as they move along their paths within the cloud layer. This approach is different from the one used in previous studies, which focused on how inhomogeneities influence the radiation field at various fixed locations. (For example, Davis (1992), Marshak et al. (1995a) and Gabriel and Evans (1996) examined the radiation at points of various densities within a

⁸Appendix A describes the way $\tau_{(r_0)}^*$ values can be obtained through Monte Carlo simulations.

⁹A convenient way to choose the random number seed is to make it equal to the index number of the photon to be simulated, i.e., to 1 for the first photon, to 2 for the second, and so on. In the case of the random number generator used in this study, the first generated random number depends systematically on the seed value, but this relationship quickly vanishes for subsequent random numbers. Hence the true randomness of the simulated photon paths can be ensured by first generating ten unused random numbers with each new setting of the random number seed, and then starting the simulation of each photon with the eleventh random number.

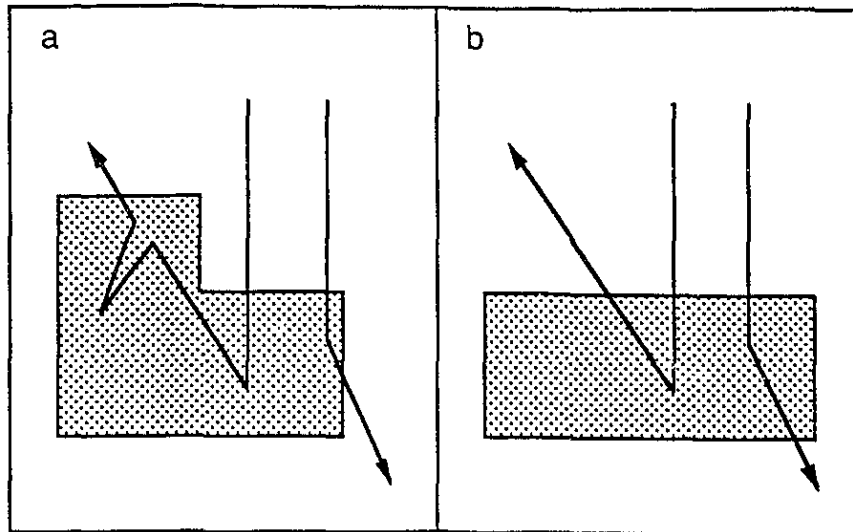


Figure 3.1.8. Photon paths within inhomogeneous and homogeneous clouds: (a) 3-D effects are present; (b) 3-D effects are not present.

cloud with VEC variations, while McKee and Cox (1974), Davies (1976, 1978), Aida (1977), Welch and Wielicki (1984) and Bréon (1992) studied the radiation that left cuboidal and cylindrical clouds through their tops and, separately, their sides.) The difference between the present approach and other ones is analogous to the difference between the Lagrangian and Eulerian approaches used, for example, in fluid dynamics. (The droplets encountered by a photon may be regarded as exerting a kind of "resistance force" on the photon. The present method examines how this force is influenced by inhomogeneities photons experience as they move along their paths ("total derivatives"), whereas previous studies focused on how local gradients in this force (i.e., cloud volume extinction coefficients at various fixed locations) affect the spatial distribution of the radiation field.)

At the end of the simulations, the amount of radiation influenced by 3-D IH effects can be obtained by counting the photons that left the cloud layer earlier (or later) in the 3-D than in the TIPA simulation. The net 3-D IH effects on the scene albedo can be obtained by using the formulas:

$$\begin{aligned}
\text{Upward trapping (UT):} & \quad UT = a / N_{total} \\
\text{Downward trapping (DT):} & \quad DT = b / N_{total} \\
\text{Upward escaping (UE):} & \quad UE = c / N_{total} \\
\text{Downward escaping (DE):} & \quad DE = d / N_{total},
\end{aligned}$$

where the symbols mean the following:

N_{total} : total number of simulated photons in each experiment,

a : number of photons that, having been influenced by upward trapping, leave the 3-D cloud field downward,

b : number of photons that, having been affected by downward trapping, get reflected in the 3-D simulation,

c : number of photons that are affected by upward escaping in the 3-D simulation, and get transmitted in the TIPPA simulation,

d : number of photons that are affected by downward escaping in the 3-D simulation, and get reflected in the TIPPA simulation.

The net effects on radiance, reflectance, or BRDF values can be calculated in two steps. First, the effects should be calculated in terms of photon numbers:

$$\begin{aligned}
\text{Upward trapping:} & \quad \frac{(a_{(\mu,\varphi)} - a_{(\mu,\varphi)}^*)}{N_{total}}, \\
\text{Downward trapping:} & \quad \frac{(b_{(\mu,\varphi)} - b_{(\mu,\varphi)}^*)}{N_{total}}, \\
\text{Upward escaping:} & \quad \frac{(c_{(\mu,\varphi)} - c_{(\mu,\varphi)}^*)}{N_{total}}, \\
\text{Downward escaping:} & \quad \frac{(d_{(\mu,\varphi)} - d_{(\mu,\varphi)}^*)}{N_{total}},
\end{aligned}$$

where $a_{(\mu,\varphi)}$ is the number of those photons affected by upward trapping that go to the angular bin (μ,φ) in the 3-D simulation, and $a_{(\mu,\varphi)}^*$ is the number of those photons influenced by upward trapping that go to bin (μ,φ) in the TIPPA-simulation. b , b^* , c , c^* , d , and d^* can be interpreted similarly for the other effects. In the second step, equations (2.2.1 - 2.2.3) should be used to transform the net effects from photon numbers to radiation units.

The net effects on the spatial distribution of reflected radiation can be calculated similarly, except that $a_{(\mu,\varphi)}$, $a_{(\mu,\varphi)}^*$, etc. should be replaced by $a_{(x,y,\mu,\varphi)}$, $a_{(x,y,\mu,\varphi)}^*$, etc., to keep track of the two (x,y) coordinates where each photon leaves the 3-D and TIPA fields, respectively. Finally, it should be noted that although this particular study examines the effects of cloud inhomogeneity only on reflection, the effects on absorption and transmission of radiation can also be calculated after appropriate modifications in the proposed scheme.

3.2 Quantitative Analysis of Radiative Inhomogeneity Effects

The main purpose of this section is to examine the mechanisms through which cloud inhomogeneities influence solar radiation, and to compare the effects of cloud top height (CTH) variability to those of volume extinction coefficient (VEC) variability.

In order to make the interpretation of numerical results easier, the effects of surrounding air and underlying surface are neglected throughout the section. Simulations are presented for 0.865 μm wavelength, assuming conservative scattering by clouds with a droplet size distribution representative of the top of Stratocumulus clouds (Section 2.2.2). The statistical uncertainty of Monte Carlo results can be estimated using equation (2.2.4), replacing A with the value in question (for example the ratio of photons affected by downward escaping), and considering that all experiments simulate the path of 100,000 photons.¹⁰

Section 3.2.1 studies inhomogeneity effects on cloud albedo for overhead sun, and Section 3.2.2 examines how these effects change with solar zenith angle. Finally, Section 3.2.3 investigates how cloud inhomogeneities affect nadir reflectance, and whether cloud inhomogeneities may explain the unexpected behavior observed by Loeb and Davies (1996b).

¹⁰The experiments presented in Section 3.2.3 simulate the path of 500,000 photons.

3.2.1 Overhead sun

First, the relative importance of various inhomogeneity effects is calculated for clouds with simple geometrical shapes. The results presented in Table 3.2.1 show that, as suggested by Harshvardhan and Thomas (1984), downward escaping is the dominant 3-D IH effect for a regular array of infinite slabs (Figure 3.2.1). This effect can be expected to become weaker if the slabs are placed on top of a plane-parallel cloud layer, resulting in a "turreted stratus" geometry (Figure 3.2.2), since the plane-parallel cloud reflects a large portion of the channeled radiation. This argument would seem to imply that the overall 3-D inhomogeneity effect gets weaker as the τ_{pp} optical thickness of the plane-parallel layer increases. This phenomenon has been observed by Davies (1976, p. 137). However, it can be argued that a thicker plane-parallel layer reflects more, and thus the amount of radiation that can potentially be affected by upward trapping increases with τ_{pp} . The results in Figure 3.2.3 show this increase in upward trapping to be so strong that, for a certain range of τ_{pp} values, the overall 3-D IH effect can even increase with τ_{pp} . These results imply that small CTH variations decrease cloud reflection most at the cloud edge ($\tau_{pp} = 0$), whereas large CTH variations decrease cloud reflection most at intermediate cloud thicknesses.

TABLE 3.2.1. 3-D Inhomogeneity effects in a regular array of infinite slabs

	Ratio of affected photons	Net effect on scene albedo
$\tau = 10$		
UT	0.010	-0.001
DT	0.007	0.001
UE	0.067	0.012
DE	0.157	-0.034
Total	0.241	-0.022
$\tau = 40$		
UT	0.021	-0.005
DT	0.006	0.001
UE	0.095	0.020
DE	0.612	-0.050
Total	0.734	-0.034

UT = upward trapping
 DT = downward trapping
 UE = upward escaping
 DE = downward escaping

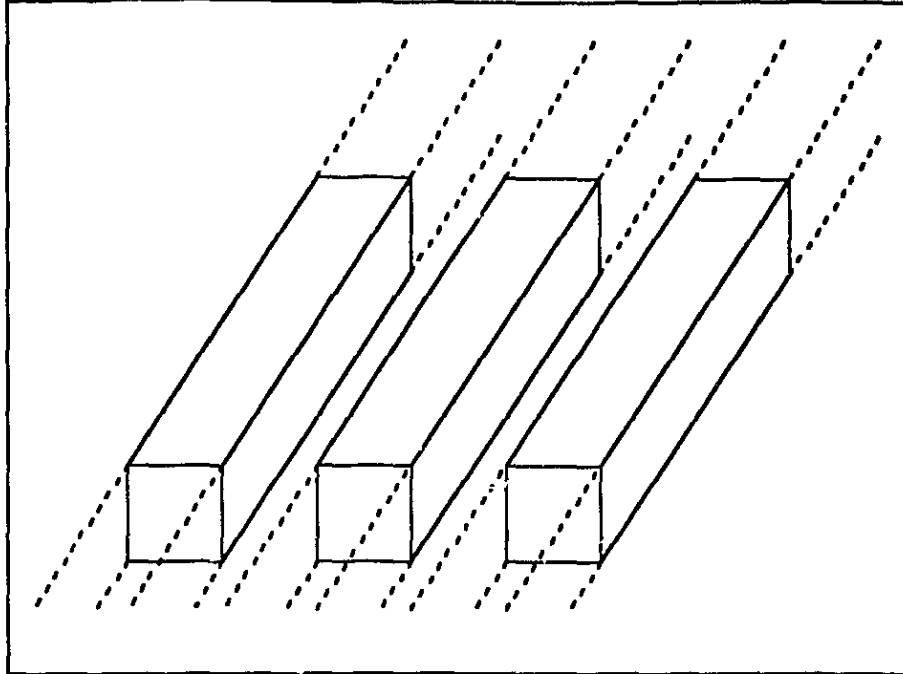


Figure 3.2.1. A regular array of infinite slabs.

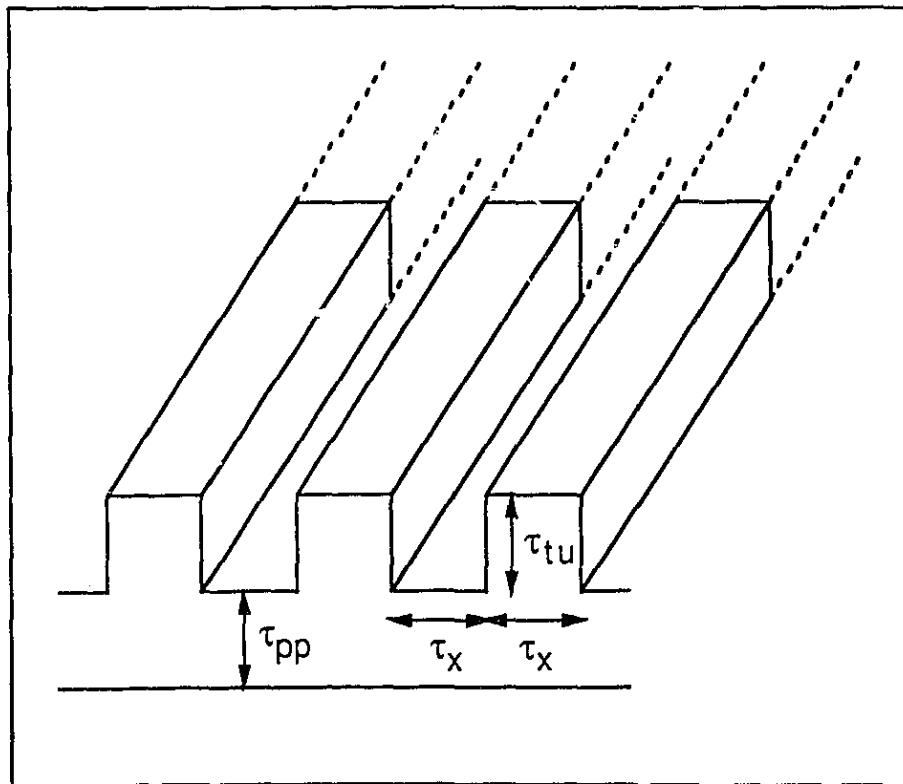


Figure 3.2.2. Turreted stratus geometry.

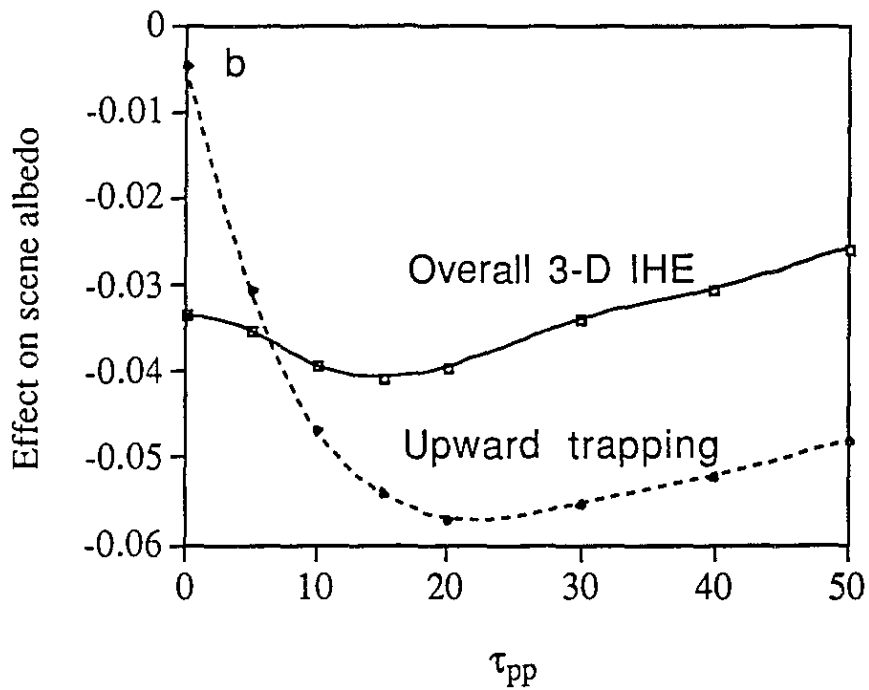
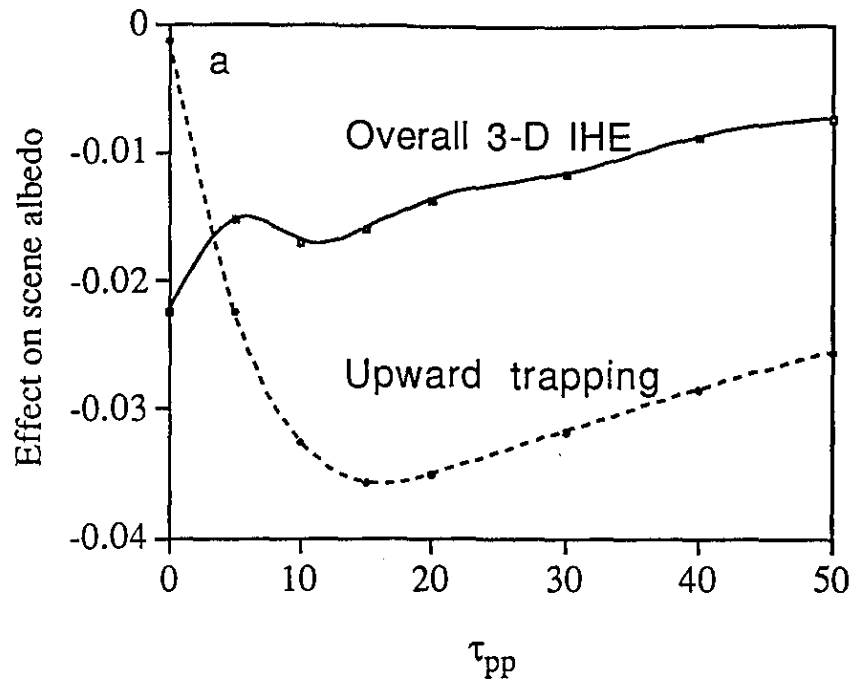


Figure 3.2.3. Sensitivity of 3-D effects to τ_{pp} for turreted stratus clouds: (a) $\tau_{lu} = \tau_x = 10$; (b) $\tau_{lu} = \tau_x = 40$.

The importance of various 3-D effects is examined by comparing the net effects of radiation flowing from thick to thin areas (i.e., DE + UE) and radiation flowing from thin to thick areas (i.e., UT + DT).¹¹ The results shown on Figure 3.2.4 reveal that the albedo is decreased less by radiation flowing from thick to thin areas than from thin to thick areas.

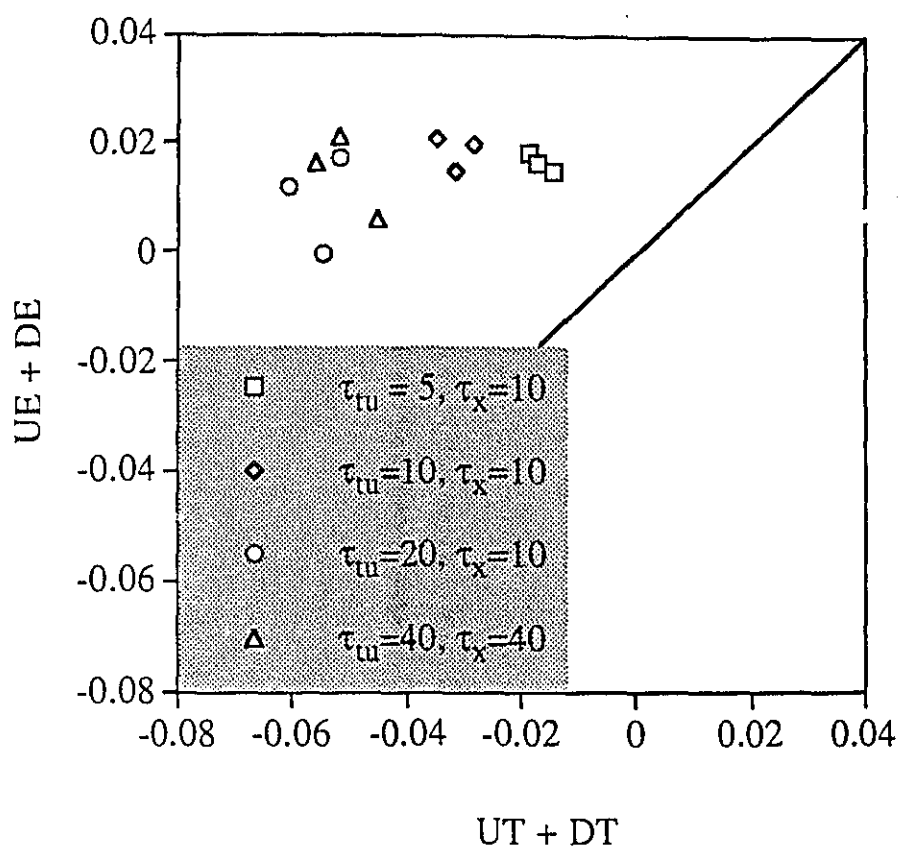


Figure 3.2.4. Influence of radiation flowing from thin to thick (UT + DT) and from thick to thin areas (UE + DE) on the albedo of turreted stratus clouds. The displayed values are for $\tau_{pp} = 10, 20,$ and 40 .

¹¹As Figures 3.i.7a and b show, some photons may experience upward trapping or downward trapping effect without ever moving to thicker cloud portions than where they entered the cloud. However, since this requires a photon to be turned back twice at suitable locations, this happens only for a negligible fraction of simulated photons.

The validity of this conclusion for more realistic cloud geometries can be examined using the Landsat scenes described in Section 2.1.2. In order to increase the variety of available scenes, 27 artificial cloud fields are also considered throughout this section. The artificial scenes are generated using the stochastic model described in Section 2.1.2, with the input parameters shown in Table 3.2.2. As the table shows, these scenes include a large variety of cloud structures from thin to thick and from nearly homogeneous to highly inhomogeneous broken cloud scenes. While this set of artificial scenes does not represent the full variety of real clouds, it allows the study of features that may not be very pronounced in the available Landsat scenes. Also, since it is not clear how representative the artificial fields are of real clouds, only the main features of the results are analyzed, and only qualitative conclusions are drawn from the numerical results.

Figure 3.2.5 shows that the flow of radiation from thin to thick areas always decreases the scene albedo, whereas the flow of radiation from thick to thin areas has a wider range of variability, and can either decrease or increase the albedo. In most cases, the scene albedo is decreased mainly by the thin to thick flow (rather than the thick to thin flow), except for

TABLE 3.2.2. Input parameters for a set of artificially generated cloud fields. A separate cloud field has been generated for each possible combination of input parameters.

Parameter	Input value(s)
VEC	30 km ⁻¹
Cloud fraction	0.98 0.75 0.5
Scaling parameters s_1, k^*, s_2	1.5, 6, 4 1, 10, 3.6 1, 12, 3
$\langle \tau \rangle$	5 15 30

VEC = volume extinction coefficient
 s_1 = scaling before break
 k^* = break wavenumber
 s_2 = scaling after break
 $\langle \tau \rangle$ = scene average optical thickness

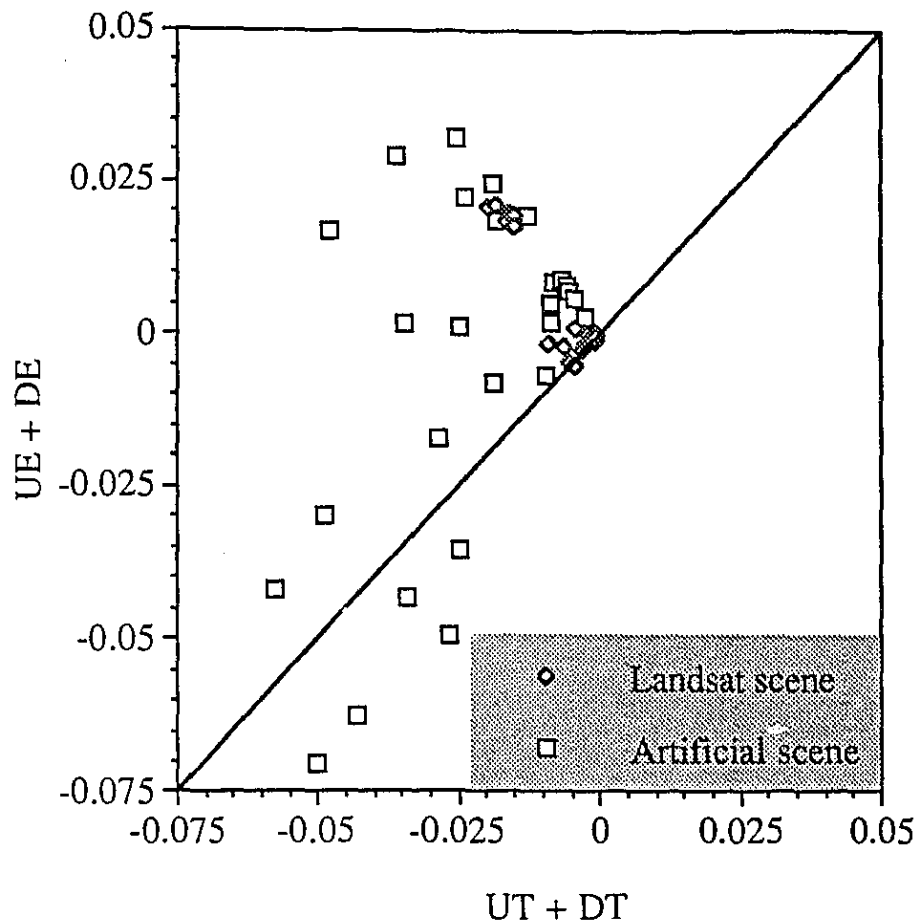


Figure 3.2.5. Influence of radiation flowing from thin to thick (UT + DT) and from thick to thin areas (UE + DE) on the albedo of cloud fields with irregular cloud top height variations.

the five most inhomogeneous scenes. These five scenes have both steep cloud sides (resulting in strong downward escaping) and low cloud fraction (resulting in weak upward trapping).

The four individual 3-D effects can be combined to examine whether the scene albedo is influenced more by 3-D effects which ease the transmission of downwelling photons (DT + DE) or which hinder the emergence of upwelling photons from the cloud field (UT + UE). Figure 3.2.6 shows that the albedo of all scenes is decreased more by making the

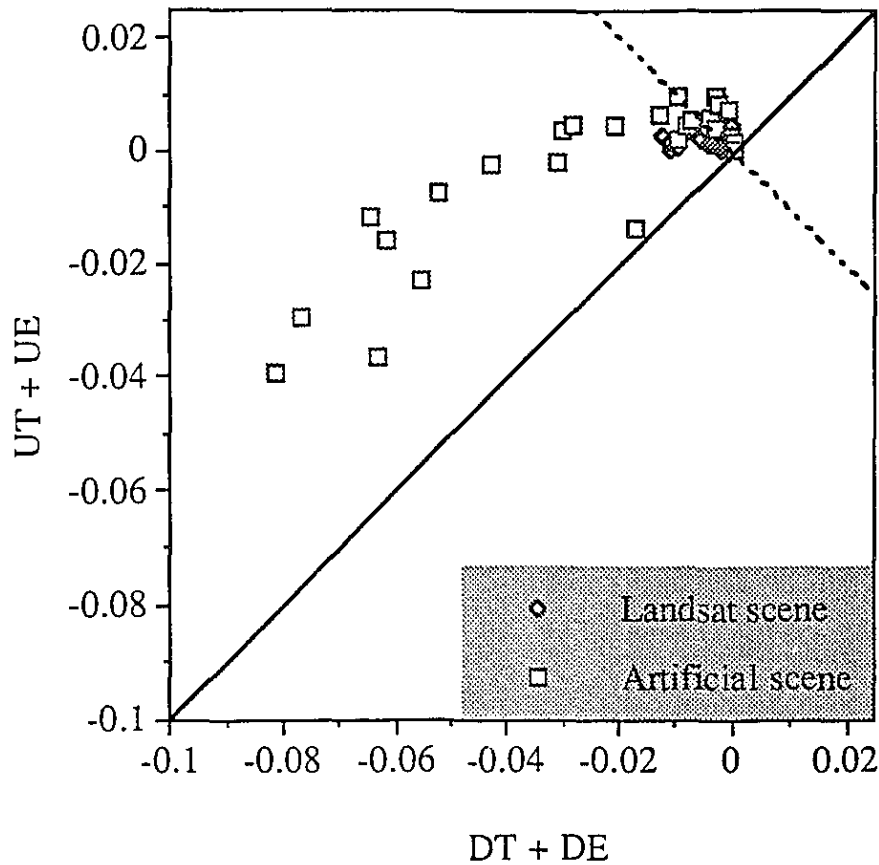


Figure 3.2.6. Influence of 3-D IH effects due to CTH variations on scene albedo by affecting transmission ($DT + DE$) and reflection ($UT + UE$). The dashed line separates cases with negative and positive overall 3-D IH effects.

transmission of some photons easier, than by making the reflection of upwelling photons more difficult ($DT + DE < UT + UE$). Since downward trapping is very weak, the position along the horizontal axis is determined mainly by the downward escaping effect, which is related to how structured a cloud field is. Thus the position along the horizontal axis can serve as a rough guide to the magnitude of cloud inhomogeneities. Figure 3.2.6 therefore suggests that upward escaping is stronger than upward trapping for small inhomogeneities, whereas the situation reverses for very large inhomogeneities.

The figure also shows that overall 3-D effects can sometimes increase the albedo even for overhead sun. This finding contradicts the argument of Zuev and Titov (1995) who argued that horizontal photon transport always decreases the cloud albedo for overhead sun, if no absorption and surface reflection is considered. Since, as Figure 3.2.7 demonstrates, downward trapping is very weak, this occasional increase is due to a relatively strong upward escaping effect.

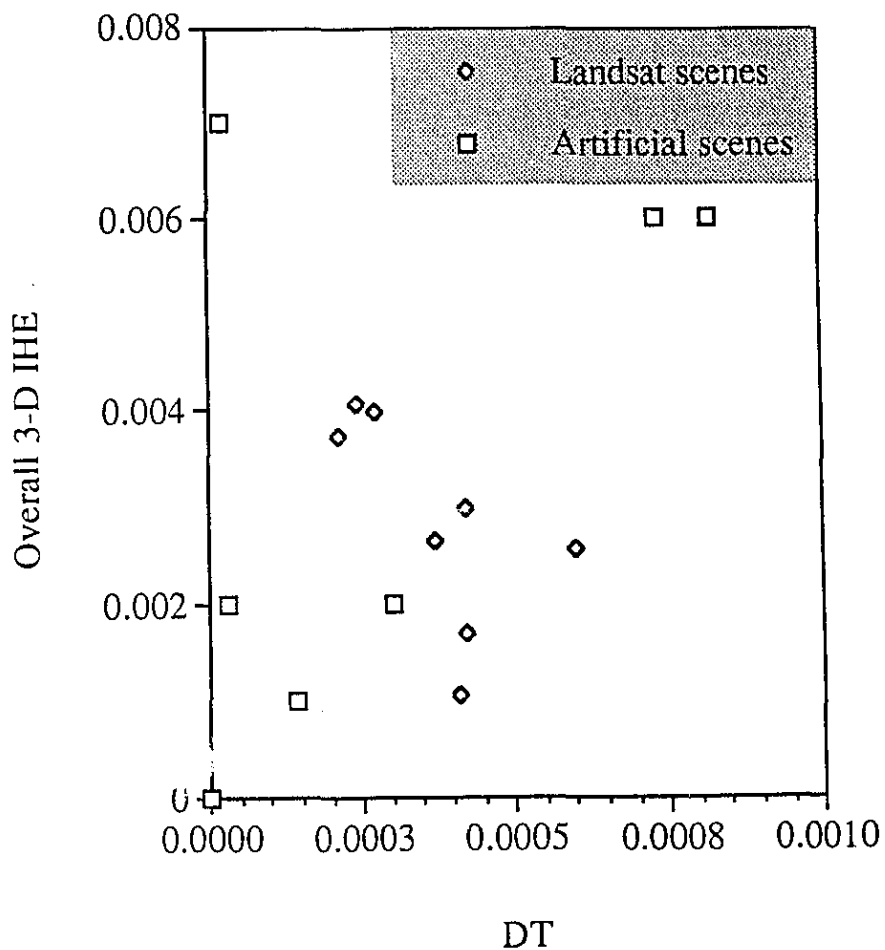


Figure 3.2.7. Influence of downward trapping on the albedo of scenes with a positive 3-D IH effect.

The next question addressed is whether cloud reflection changes markedly if, as in previous studies, the geometrical cloud thickness is kept constant and the optical thickness variations observed in Landsat scenes are attributed to variations in the VEC. The most appropriate way to compare these two representations of cloud inhomogeneities (i.e., the assumption of CTH and VEC variations) is to consider the same τ -distributions, average cloud geometrical thicknesses and cloud VEC's for both approaches.

For overhead sun, the 1-D IH effect depends only on the optical thickness distribution, and is thus the same for both approaches. However, the results shown in Figure 3.2.8 indicate that CTH variations cause much stronger 3-D effects than VEC variability. The reasons CTH variations decrease the albedo more effectively than VEC variations can be illustrated through the example of a particular τ -field shown in Figure 2.1.1. The differences in the individual 3-D effects (Table 3.2.3) can be explained as follows.

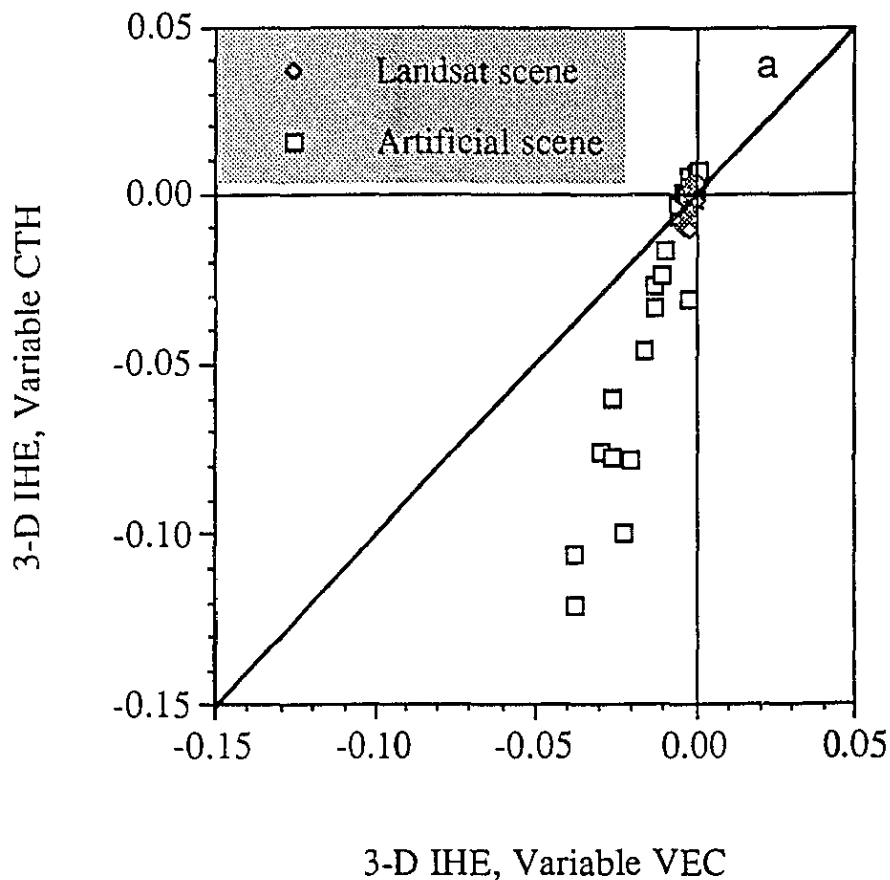


Figure 3.2.8. Overall 3-D IH effects due to CTH and VEC variations for overhead sun. (a) all scenes; (b) Landsat scenes only.

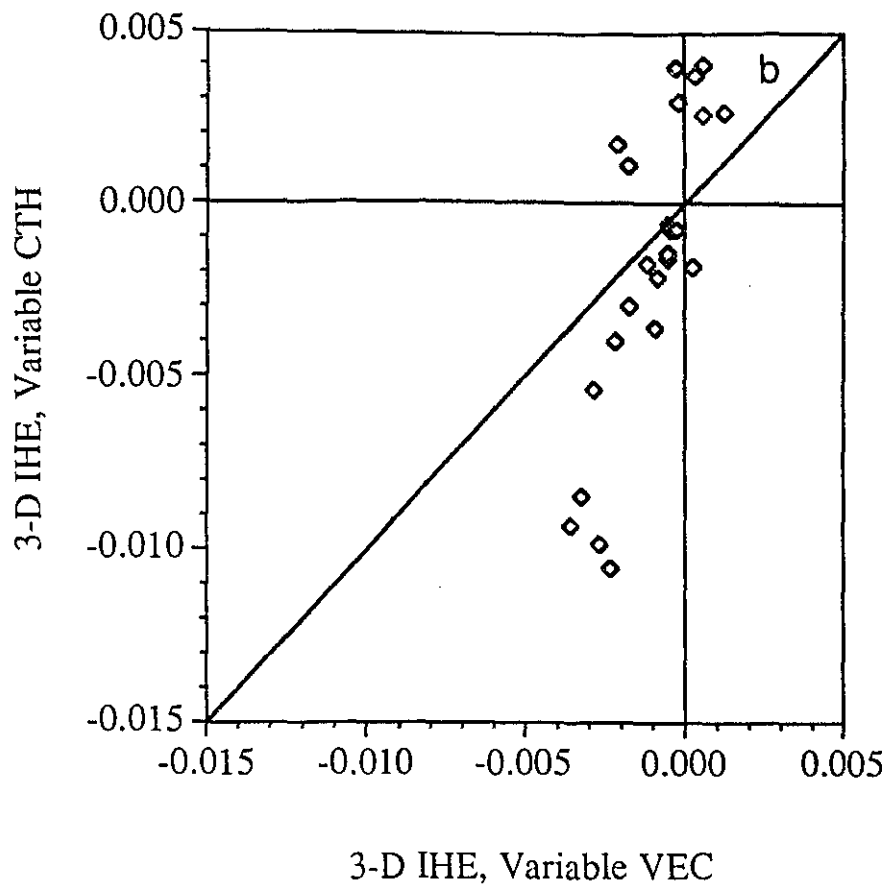


TABLE 3.2.3. 3-D inhomogeneity effects for the cloud field shown in Figure 2.1.1. The 1-D inhomogeneity effect on scene albedo is -0.127.

Inhomogeneity effect	CTH variations		VEC variations	
	Ratio of affected photons	Net effect on scene albedo	Ratio of affected photons	Net effect on scene albedo
UT	0.162	-0.026	0.146	-0.010
DT	0.019	0.002	0.150	0.017
UE	0.192	0.031	0.179	0.016
DE	0.134	-0.030	0.205	-0.034
Total	0.544	-0.023	0.680	-0.011

CTH = cloud top height
 VEC = volume extinction coefficient
 UT = upward trapping
 DT = downward trapping
 UE = upward escaping
 DE = downward escaping

Upward trapping

The effects of upward trapping can be studied by considering a photon that enters a thin pixel of optical thickness τ_1 , descends in that pixel through an optical distance τ_d , and then moves to a neighboring pixel in which $\tau_2 > \tau_1$ (Figure 3.2.9a, b). The fact that upward trapping affects only about 11 % more radiation for CTH than for VEC variations, whereas the difference in the net effects is about 270 %, indicates that the main difference is not in the amount of radiation that goes from pixel 1 to pixel 2, but in the different efficiency of upward trapping once the radiation moves to pixel 2. This efficiency, defined as

$$\text{Efficiency} = \frac{|net\ effect|}{amount\ of\ radiation\ influenced} \quad ,$$

depends on the τ_{up} net optical thickness through which radiation must ascend to emerge from the cloud layer. The larger the τ_{up} , the more radiation gets turned downward again and gets transmitted to the underlying surface, which results in a stronger net upward trapping effect. For CTH variations, τ_{up} is

$$\tau_{up}^{CTH} = \tau_2 - (\tau_1 - \tau_d) \quad ,$$

whereas for VEC variations,

$$\tau_{up}^{VEC} = \tau_2 - (\tau_1 - \tau_d) \frac{\beta_2}{\beta_1} \quad .$$

Since $\beta_2 > \beta_1$, $\tau_{up}^{CTH} > \tau_{up}^{VEC}$, which implies a stronger upward trapping effect for CTH than for VEC variations.

Downward trapping

Table 3.2.3 shows that downward trapping is a very weak effect for CTH variations. The reason for this is that radiation has to turn around twice, and go over the cloud top between its two "U-turns" (Figure 3.2.9c), which does not happen very often. In the case of VEC variations, however, even a slight change in a photon's direction may result in downward trapping (Figure 3.2.9d). That is why downward trapping is much stronger for VEC than for CTH variations.

Upward escaping

As Table 3.2.3 shows, the amount of radiation affected by upward escaping is similar for both CTH and VEC variations. Thus the explanation for the two-fold difference in their net effects should be sought by considering whether the affected photons would also be reflected without the inhomogeneities. This depends mainly on the $\tau_s = \tau_d - \tau_{up}$ optical thickness that, due to inhomogeneities, is "skipped" by the affected photons. A larger τ_s value means that more of the affected photons would be turned downward again if there were no inhomogeneities. For CTH variations (Figure 3.2.9e),

$$\tau_{up}^{CTH} = 0, \quad \text{if } \tau_d < (\tau_2 - \tau_1), \text{ and}$$

$$\tau_{up}^{CTH} = \tau_2 - (\tau_1 - \tau_d), \quad \text{if } \tau_d > (\tau_2 - \tau_1).$$

For VEC variations (Figure 3.2.9f),

$$\tau_{up}^{VEC} = \tau_2 - (\tau_1 - \tau_d) \frac{\beta_2}{\beta_1} = \tau_2 - (\tau_1 - \tau_d) \frac{\tau_2}{\tau_1}.$$

Since $\tau_2 < \tau_1$, $\tau_{up}^{VEC} > \tau_{up}^{CTH}$ for any τ_d value. In turn, $\tau_s^{CTH} > \tau_s^{VEC}$, which means that ascending photons "skip" more cloud particles in the case of CTH variations. Thus for VEC variations, most of the photons affected by upward escaping would get reflected anyway, whereas CTH variations enable the reflection of many photons that would have been turned downward to the surface, if they had not skipped τ_s^{CTH} . This explains why upward escaping is more efficient for CTH than for VEC variations.

Downward escaping

Table 3.2.3 shows that downward escaping affects more radiation for VEC than for CTH variations. The reason for this is that for VEC variability, downward escaping can influence photons that move horizontally at any altitude, whereas for CTH variability, it can affect only those photons that move horizontally above the cloud top (Figure 3.2.9g and h).

Table 3.2.3 also indicates that downward escaping is more efficient for CTH than for VEC variations. This means that in clouds with variable CTH, a larger portion of the affected photons would be reflected without inhomogeneities. The efficiency depends on the τ_s optical thickness that is skipped due to downward escaping: the larger the τ_s , the

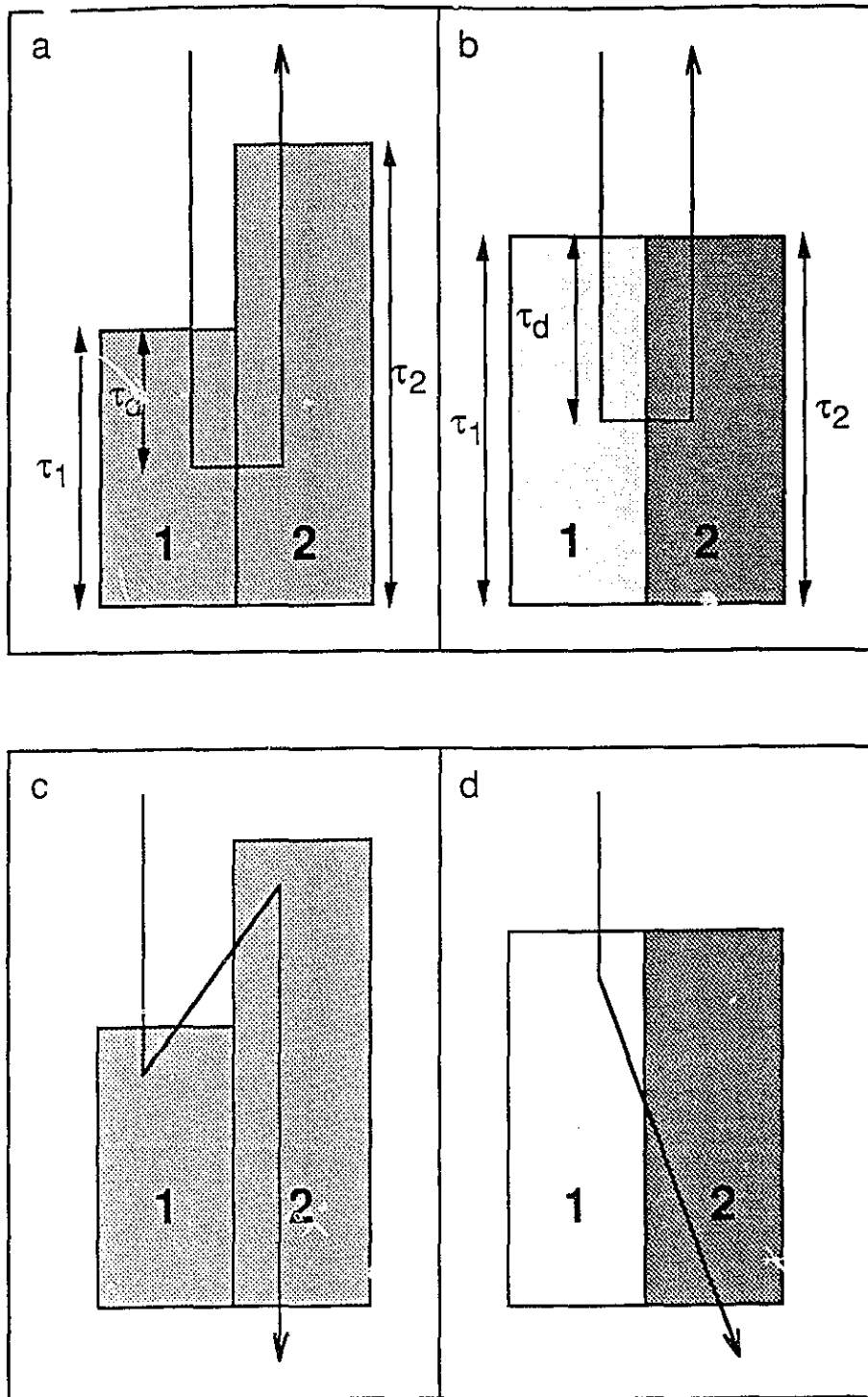
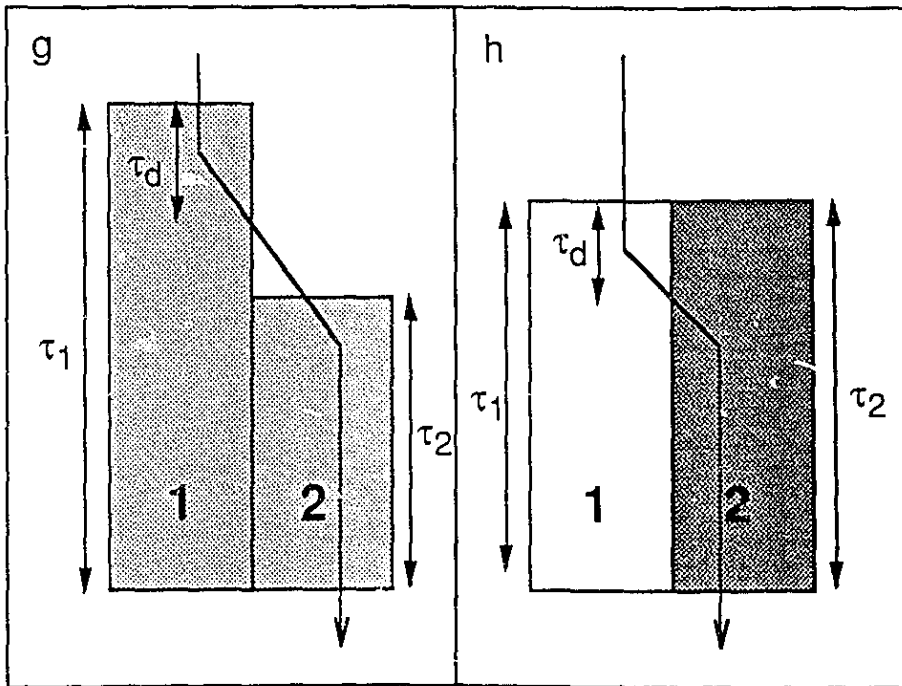
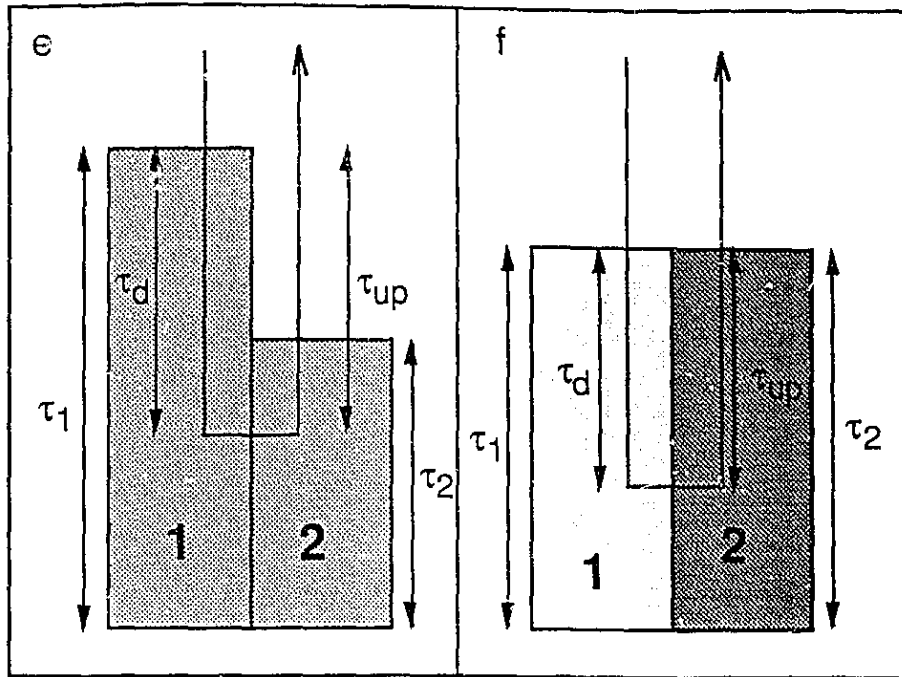


Figure 3.2 9. Two-column models for 3-D IH effects due to CTH and VEC variations. (a)-(b) upward trapping; (c)-(d) downward trapping; (e)-(f) upward escaping; (g)-(h) downward escaping.



more of the transmitted photons would be reflected without downward escaping. τ_s can be calculated using $\tau_s = \tau^* - \tau_v$, where τ^* is the optical thickness of the pixel where the photon enters the cloud layer (determined using the TIPA), and τ_v is the vertical optical thickness the photon actually passes through. The value of τ_v can be obtained using

$$\tau_v = \int_{r_0}^{r_a} \beta(x, y, z) dz \quad ,$$

where $r_0 = (x_0, y_0, z_{top})$ indicates the point at which the photon entered the cloud layer, and $r_a = (x_a, y_a, z_a)$ refers to the photon's actual position. The integration should be performed along the photon's path (instead of along a straight line connecting r_0 and r_a) to calculate the current value of τ_v before each scattering event.

For the sample cloud field, the average τ_s is 7.06 for CTH variations, and 4.83 for VEC variations. The fact that $\tau_s^{CTH} > \tau_s^{VEC}$ is consistent with the higher efficiency for CTH variations. However, this higher efficiency is not straightforward to explain. According to the two-column model used for explaining other 3-D effects,

$$\begin{aligned} \tau_s^{CTH} &= 0, \quad \text{if } \tau_d > (\tau_2 - \tau_1), \\ \tau_s^{CTH} &= (\tau_1 - \tau_d) - \tau_2, \quad \text{if } \tau_d < (\tau_2 - \tau_1), \text{ and} \\ \tau_s^{VEC} &= (\tau_1 - \tau_d) - (\tau_1 - \tau_d) \frac{\beta_2}{\beta_1} = (\tau_1 - \tau_d) - (\tau_1 - \tau_d) \frac{\tau_2}{\tau_1}. \end{aligned}$$

Since $\tau_2 < \tau_1$, τ_s^{VEC} is always positive. This implies that $\tau_s^{VEC} > \tau_s^{CTH}$, if $\tau_d > (\tau_2 - \tau_1)$. If $\tau_d < (\tau_2 - \tau_1)$, the difference between the two τ_s values is

$$\tau_s^{CTH} - \tau_s^{VEC} = (\tau_1 - \tau_d) - \tau_2 - \left[(\tau_1 - \tau_d) - (\tau_1 - \tau_d) \frac{\tau_2}{\tau_1} \right] = -\tau_2 + (\tau_1 - \tau_d) \frac{\tau_2}{\tau_1} = \frac{\tau_2}{\tau_1} (-\tau_d) < 0.$$

This result, based on the two-column model, is opposite to the situation for actual cloud fields, where $\tau_s^{CTH} > \tau_s^{VEC}$. This apparent contradiction can be resolved by considering the horizontal distance traveled by photons that experience the downward escaping effect. Since these photons tend to move toward thinner regions, it can be expected that as they

travel farther, they go to even thinner areas and hence experience a stronger downward escaping effect (i.e., τ_s is larger for them). In the case of CTH variations, since photons affected by downward escaping start moving horizontally at high altitudes, they can travel large horizontal distances by the time they reach the bottom of the cloud layer. In the case of VEC variations, however, photons can experience downward escaping even if they start moving horizontally only near the cloud base. Since these photons have little room to travel large horizontal distances before reaching the cloud base, they do not experience large τ -variations that would cause strong downward escaping effects. Hence, downward escaping can be expected to be more efficient for CTH than for VEC variations.

The above hypothesis can be evaluated by calculating the average horizontal distance traveled by photons that experience downward escaping. For the cloud field shown in Figure 2.1.1, the average distance is 0.92 km for CTH and 0.59 km for VEC variations. The ratio of these two distances, $\frac{0.92}{0.59} = 1.56$ is similar to the ratio $\frac{7.08}{4.83} = 1.47$ of the average τ_s values for the two cloud representations, suggesting that the differences in traveled distances may be the main reason for the differences in the efficiency of the downward escaping effect.

Overall

Since CTH and VEC variations cause very different radiative effects, the question may arise whether 3-D effects due to VEC variability always decrease cloud albedo, or, similarly to CTH variations, sometimes increase it. Figure 3.2.8 indicates that overall 3-D effects decrease the albedo for all scenes, even those with τ -variations for which 3-D effects due to CTH variability increase the albedo.¹² This can be explained by considering that upward escaping increases the albedo much less for VEC than for CTH variations.¹³

Since, as shown in Table 3.2.3, downward escaping is by far the strongest 3-D LH effect for all the scenes with VEC variations, horizontal photon transport decreases the scene albedo mainly through radiation flowing from thick to thin areas (i.e., UE + DE), even for

¹²The positive values for VEC variations on Figure 3.2.8 are smaller than the statistical uncertainty of the Monte Carlo simulations.

¹³There is one situation in which overall 3-D effects of VEC variations are found to increase cloud albedo: that of overcast cloud fields with extreme small-scale variability in horizontal directions. In this case, 1-D radiative transfer (IPA or TIPA) would assume a very inhomogeneous cloud, whereas multiple scattering effectively smoothes out the effects of horizontal variations. Therefore the main process responsible for increasing cloud reflection is not upward trapping (as for CTH variations), but very strong downward trapping. However, the variability must be so large for this phenomenon to occur, that it probably is highly atypical in the atmosphere.

those scenes in which the opposite flow dominates for CTH variations (Figure 3.2.10). The strong downward escaping effect also ensures that the albedo is lowered mainly by making the transmission of downwelling radiation easier, as opposed to making the reflection of upwelling radiation more difficult (Figure 3.2.11). (This finding confirms previous studies (e.g., Cannon 1970; Davis 1992, which focused on downward escaping as the main inhomogeneity effect in clouds with internal VEC variability.)

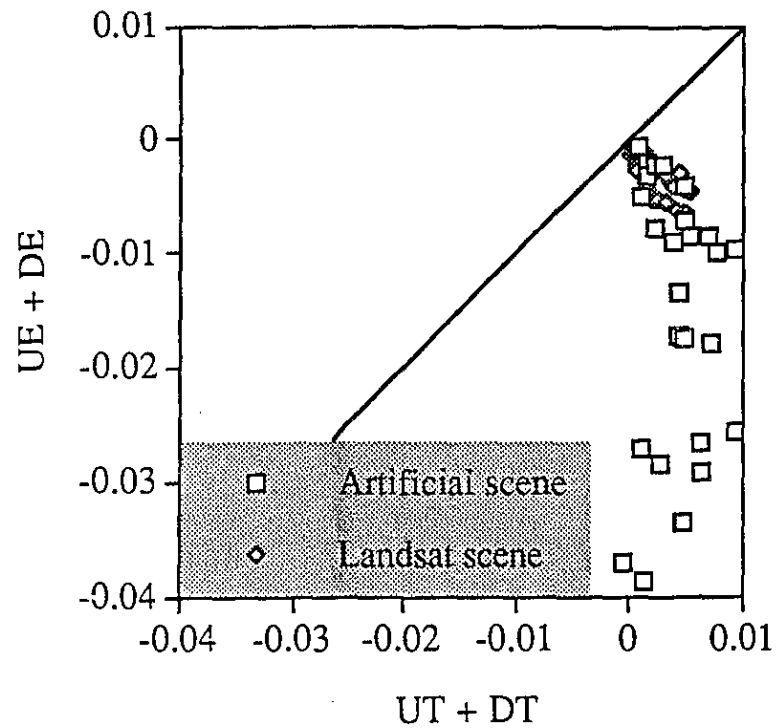


Figure 3.2.10. Effects of radiation flowing from thick to thin (UE + DE) and from thin to thick areas (UT + DT) for clouds with VEC variations.

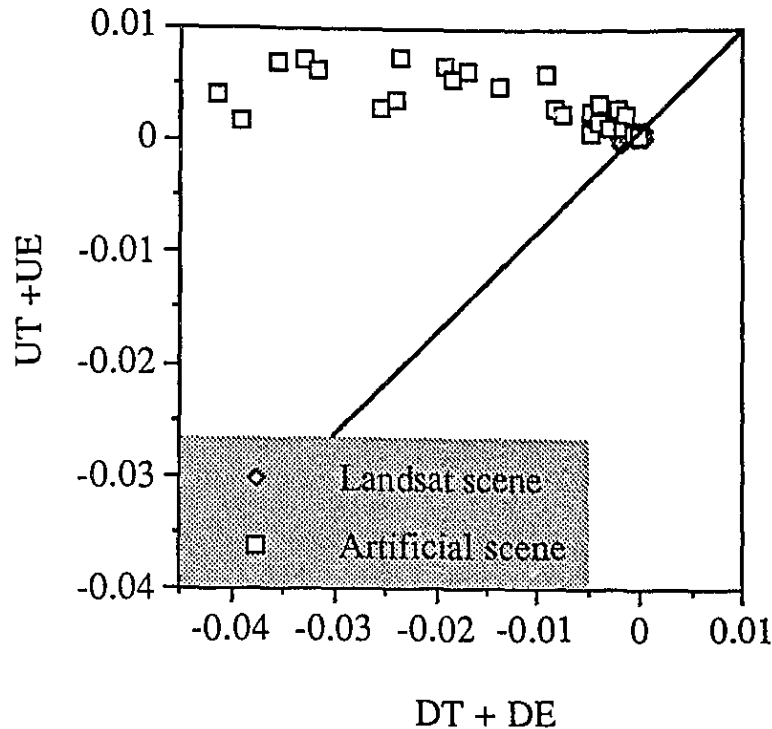


Figure 3.2.11. Influence of 3-D IH effects due to VEC variations on the scene albedo by affecting transmission (DT + DE) and reflection (UT + UE).

3.2.2 Oblique sun

Numerous previous studies indicate that the radiative effects of cloud inhomogeneities change significantly with solar zenith angle (SZA). This section examines how cloud inhomogeneities affect solar radiation for oblique sun.

Since, as noted in Section 3.1.1, cloud fields appear more homogeneous from oblique directions than from above, the 1-D IH effect decreases with increasing SZA (Figure 3.2.12). Figure 3.2.12 demonstrates that for the cloud field shown in Figure 2.1.1, the overall 3-D IH effect, especially for CTH variations, is not very sensitive to the solar zenith angle. However, Figure 3.2.13 shows that this insensitivity is a rare case, and that the overall 3-D IH effect can either increase or decrease with the SZA. Figure 3.2.14 indicates that the relative stability of the overall 3-D IH effect on Figure 3.2.12 seems to

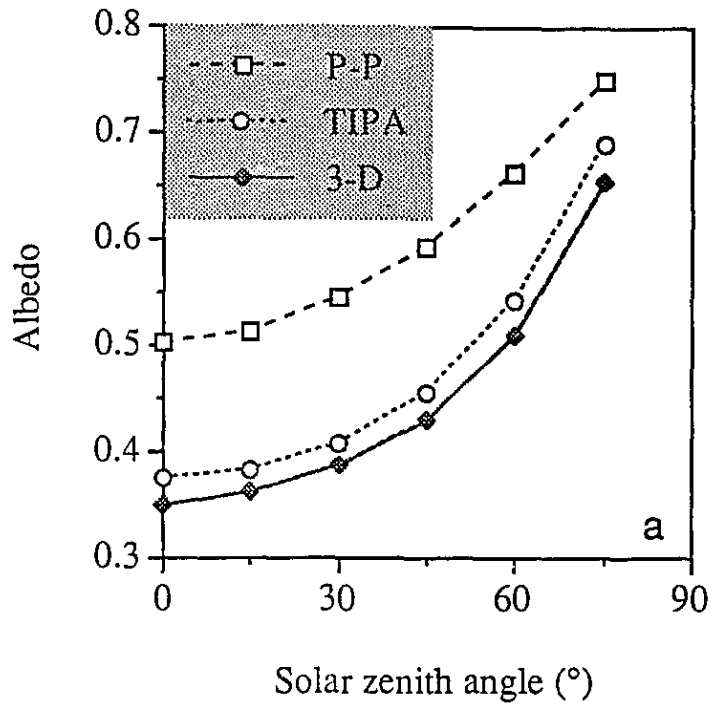
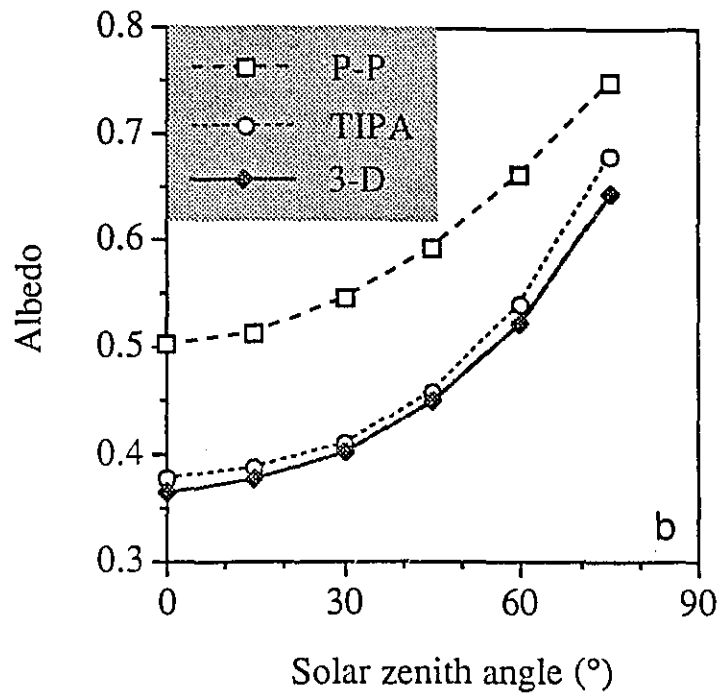


Figure 3.2.12. Solar zenith angle dependence of albedos obtained for the cloud field shown in Figure 2.1.1. The albedos are calculated using the homogeneous, plane-parallel assumption, the TIPA, and 3-D Monte Carlo simulations: (a) for CTH variations; (b) for VEC variations.



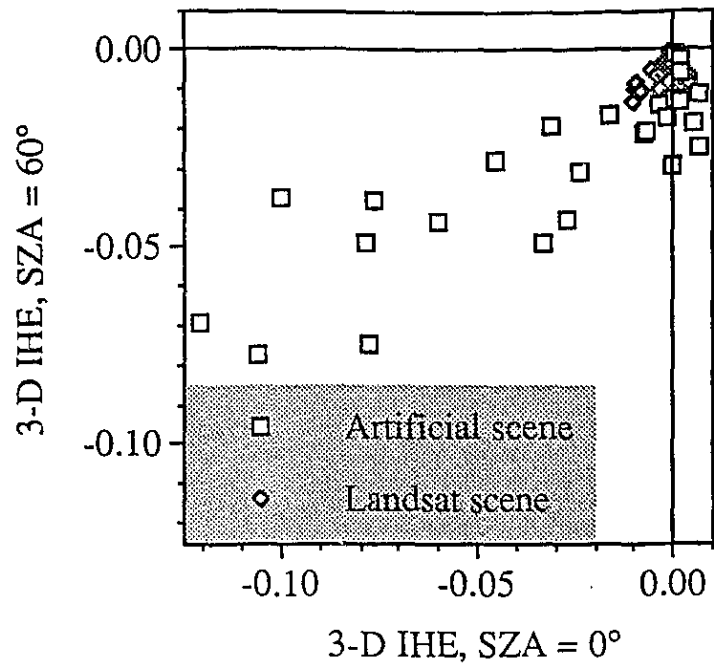


Figure 3.2.13. Overall 3-D IH effects for scenes with CTH variations.

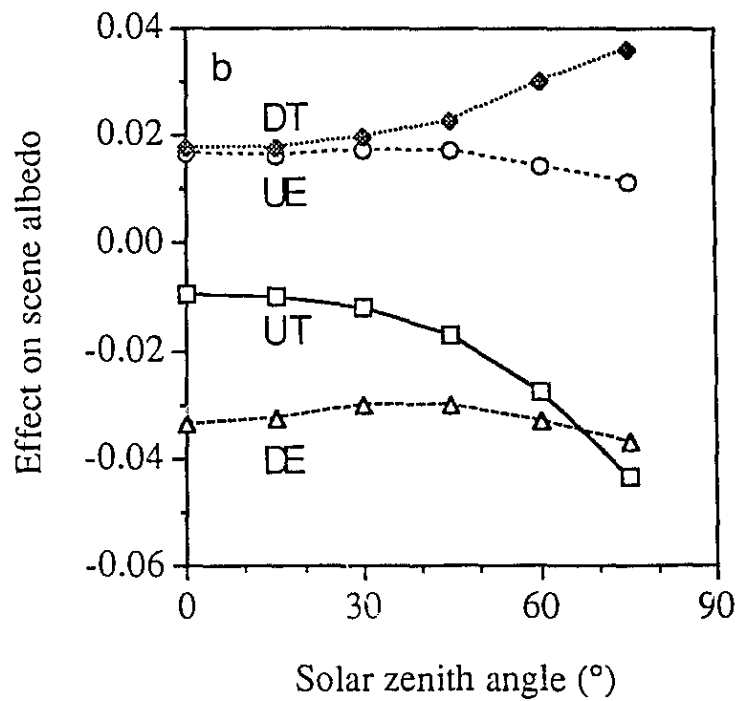
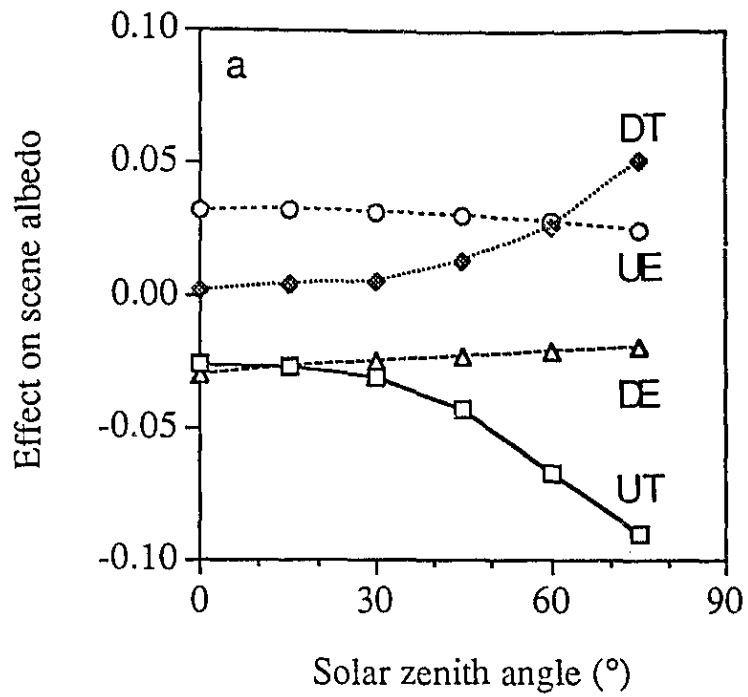
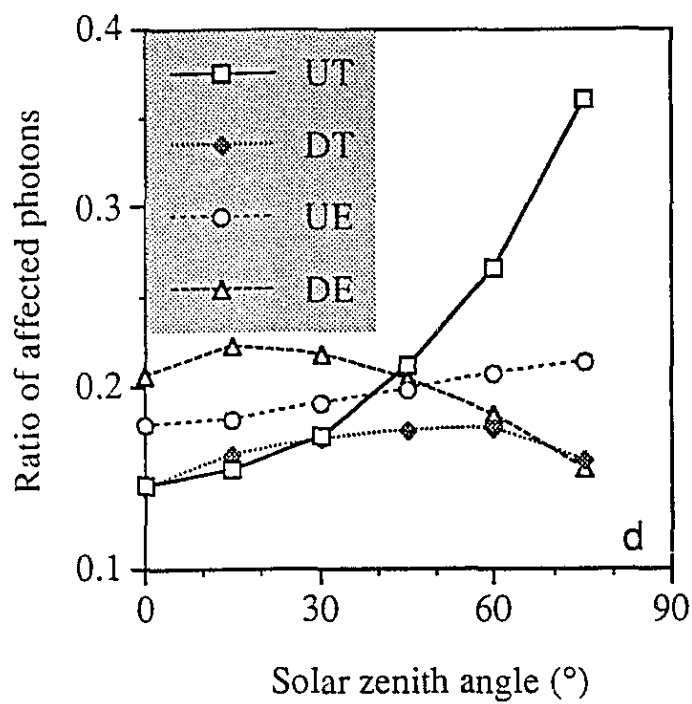
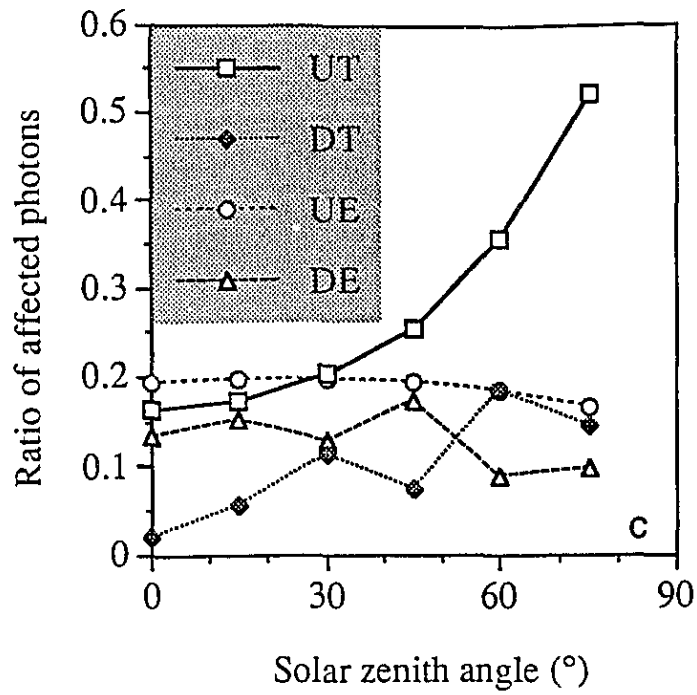


Figure 3.2.14. 3-D IH effects for the cloud field shown in Figure 2.1.1: (a) effect on scene albedo for CTH variations; (b) effect on scene albedo for VEC variations; (c) ratio of affected photons for CTH variations; (d) ratio of affected photons for VEC variations.



be a rare case in which changes in the individual 3-D effects nearly cancel each other out. As the figure shows, the changes are due mainly to variations in the amount of radiation influenced by each effect, rather than to variations in the efficiency of 3-D effects. As a general trend, this amount can be expected to increase with SZA, since clouds intercept more radiation for oblique sun, and thus make more radiation potentially available for the individual 3-D effects.^{14,15} However, other factors also influence the way 3-D effects depend on solar elevation. The main factors for the individual effects are as follows.

Upward trapping

The radiation that is potentially available for upward trapping is that which would be reflected in the TIPA. This amount increases with SZA because more radiation is intercepted by clouds, but also because the reflection of even a homogeneous, plane-parallel cloud increases with SZA. However, as Figure 3.2.12 shows, these effects could increase upward trapping by a factor of only $\frac{0.54}{0.38} = 1.42$ if the SZA increased from 0° to 60°. This would increase the radiation affected by upward trapping to 23% and 21% for CTH and VEC variations, respectively. Since in actuality, however, upward trapping affects 35% and 26%, respectively, another process must be responsible for the remainder of the increase.

The main process responsible for the remaining increase is probably that, as the SZA increases, cloud sides tilted toward the sun intercept increasing portions of the total incoming radiation, whereas cloud sides tilted away from the sun intercept less radiation, i.e., $Y_{CTH} > X_{CTH}$ on Figure 3.2.15a. Since cloud particles scatter predominantly in forward directions, this increased number of photons moves to thicker cloud portions by the time it starts ascending, and hence experiences the upward trapping effect. For moderate cloud variability, the part of cloud which gets thicker in the forward direction intercepts less radiation for VEC than for CTH variations; i.e., $\frac{Y_{VEC}}{X_{VEC}} < \frac{Y_{CTH}}{X_{CTH}}$ in Figure 3.2.15b. Hence, this process can be expected to increase upward trapping less for VEC than for CTH variations, in accordance with the tendency in Figure 3.2.14. For very strong inhomogeneities (i.e., horizontally small clouds with steep sides), however, upward trapping increases at about the same rate for both CTH and VEC variations

¹⁴This trend exists only up to a certain solar zenith angle, where the apparent cloud fraction reaches saturation.

¹⁵Since the intensity of solar illumination decreases with $\cos(\text{SZA})$, the actual amount of radiation intercepted by clouds may also decrease with increasing SZA. Thus, the term "amount of radiation" refers to radiation after a normalization by $\cos(\text{SZA})$.

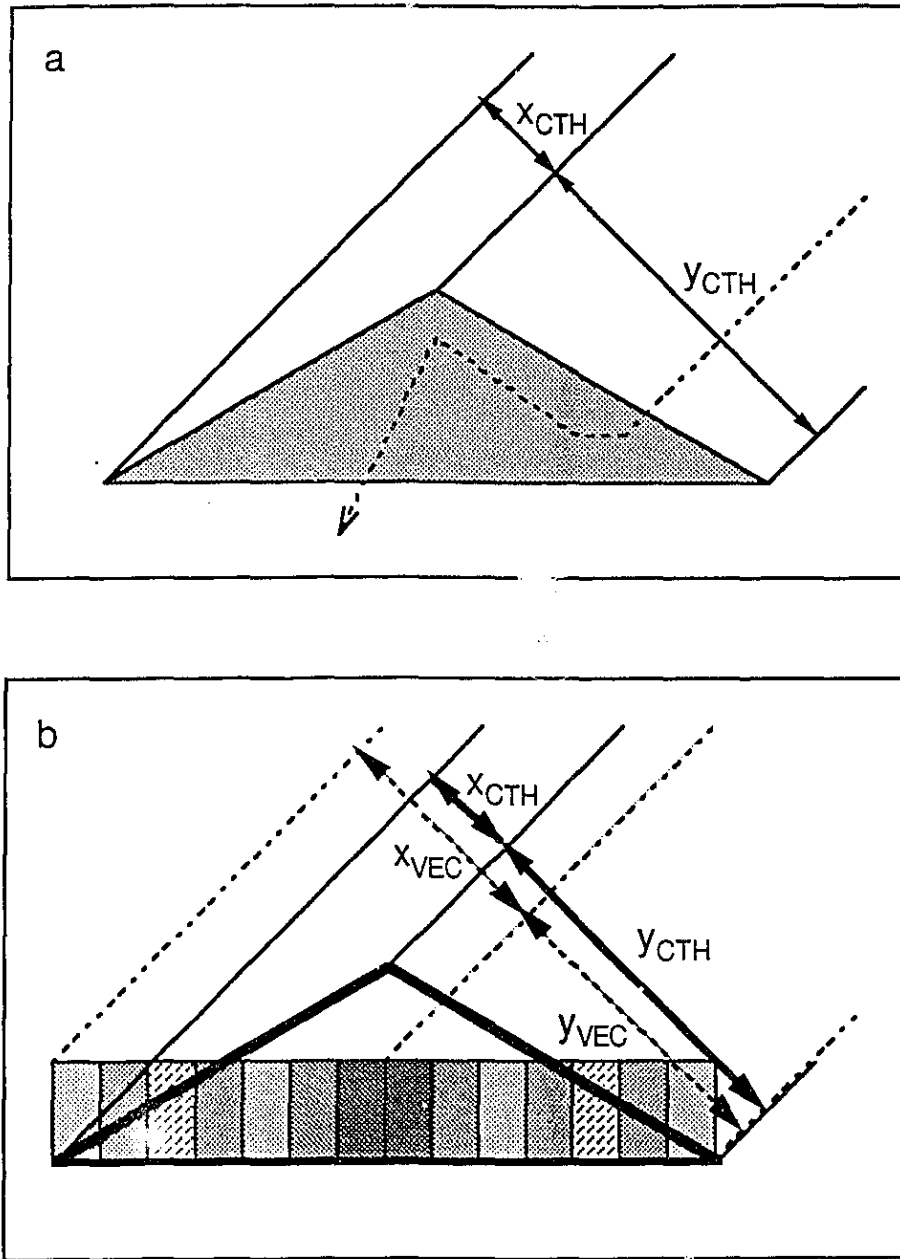


Figure 3.2.15. Amount of solar radiation intercepted by the two sides of simple clouds. The optical thickness increases linearly toward the cloud center. (a) cloud with CTH variations. The dashed line indicates the path of a photon that experiences upward trapping; (b) clouds with CTH (thick line) and VEC variations (shaded rectangle). These two clouds have the same τ -distribution and average geometrical thickness.

(Figure 3.2.16a, b). In such cases, the extra increase for CTH variations (expected from Figure 3.2.15b) is limited by the fact that if photons enter a cloud near its center, they may move to its other side by the time they start ascending, and hence experience a weaker upward trapping effect, or even upward escaping (Figure 3.2.17a). In the case of moderate CTH variations, for example, if all reflected photons started to ascend after having descended through the same τ_d optical thickness, most of the extra radiation that is intercepted by the right hand side of a large triangular cloud would be available for an extra increase in upward trapping ($= Y_b$ in Figure 3.2.17b). For a small, steep cloud, however, only a small portion of the extra amount would experience upward trapping ($= Y_c$ in Figure 3.2.17c). Hence, upward trapping for CTH and VEC variations can be expected to change more similarly with SZA for very inhomogeneous scenes, which agrees with the tendency in Figures 3.2.16a and b.

Downward trapping

The radiation that is potentially available for downward trapping is the portion of radiation that is intercepted by clouds and would be transmitted without 3-D IH effects. This radiation can be calculated by subtracting $(I - CF_{app})$ from the scene's transmission as calculated by the TIPA. As Figure 3.2.18 indicates, this amount decreases with increasing SZA for both CTH and VEC variations.

However, Figures 3.2.14 and 3.2.16c indicate that for CTH variations, downward trapping increases steeply with the SZA. This happens because, for overhead sun, two U-turns are required for a photon to experience downward trapping, whereas for oblique sun, even a slight change in a photon's direction may result in downward trapping (Figure 3.1.7b). The amount of radiation that can be influenced by this effect, after being scattered at some particular angle, increases with SZA (e.g., $x_b > x_a$ in Figure 3.2.19), thus resulting in stronger downward trapping for more oblique sun.

For clouds with VEC variations, on the other hand, any small scattering-angle can cause downward trapping regardless of SZA. For overhead sun, about half of the radiation transmitted through an idealized symmetric cloud is influenced by downward trapping (Figure 3.2.20a). For oblique sun, diffusion caused by multiple scattering pushes the average transmitted radiation below the direct beam to a degree which increases as the radiation sinks deeper into the cloud (Figure 3.2.21).¹⁶ Thus, downward trapping can be expected to increase with SZA on the side farther from the sun, and decrease on the side

¹⁶The reflected radiation, on the other hand, tends to move above the direct beam.

closer to it (Figure 3.2.20b). However, radiation scattered below the direct beam may experience downward trapping even if it entered the cloud to the right of the cloud center (Figure 3.2.20c). Hence, as SZA increases, the radiation affected by downward trapping takes up a slightly increasing portion of the total radiation transmitted through clouds.

The comparison of Figures 3.2.14b and d reveals that for VEC variations, the efficiency of downward trapping increases with SZA. This can be explained by considering that multiple scattering tends to push photons below the direct beam to a degree that increases with SZA (Figure 3.2.22). Therefore, the difference between τ^* and the τ_v that photons actually encounter also increases with SZA, thus implying a more efficient and hence stronger downward trapping (Figures 3.2.14b and 3.2.16d).

Upward escaping

The radiation potentially available for upward escaping is simply that which is intercepted by clouds, regardless of whether it would be reflected or transmitted without 3-D IH effects. Figures 3.2.14, and 3.2.16e and f show that, although this potential radiation increases with SZA, upward escaping nevertheless remains fairly constant. For CTH variations, this is because the increase in the potentially available radiation is counteracted by the very same effect which enhances upward trapping. That is, the fact that the intercepted photons tend to move forward into thicker cloud portions (Figure 3.2.15a) increases upward trapping at the expense of upward escaping.

Upward escaping tends to remain fairly constant for VEC variations as well. This can be explained by considering that the amount of potentially available radiation (i.e., radiation intercepted by clouds) increases due to the extra radiation intercepted by cloud sides. Most of this potentially available radiation, however, moves forward, toward denser regions, and hence tends to experience upward trapping rather than upward escaping. The upward escaping effect thus tends to influence only parts of the fraction of incoming solar radiation that enters through the cloud top. (This fraction remains constant at the value of the nadir cloud fraction.)

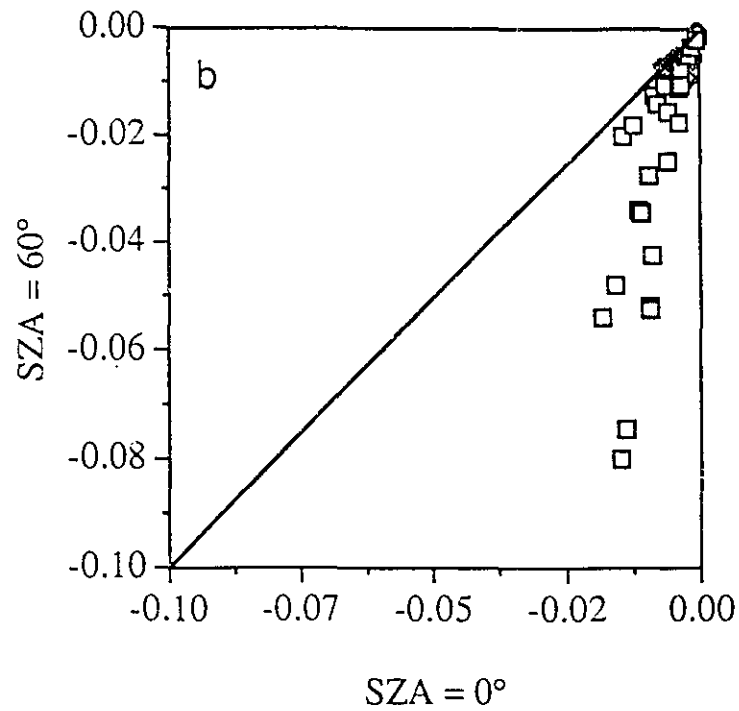
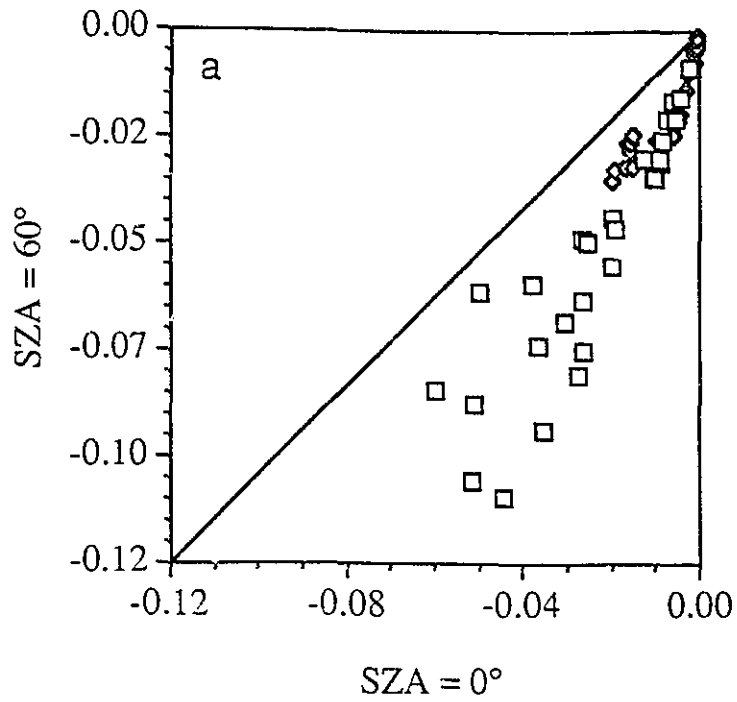
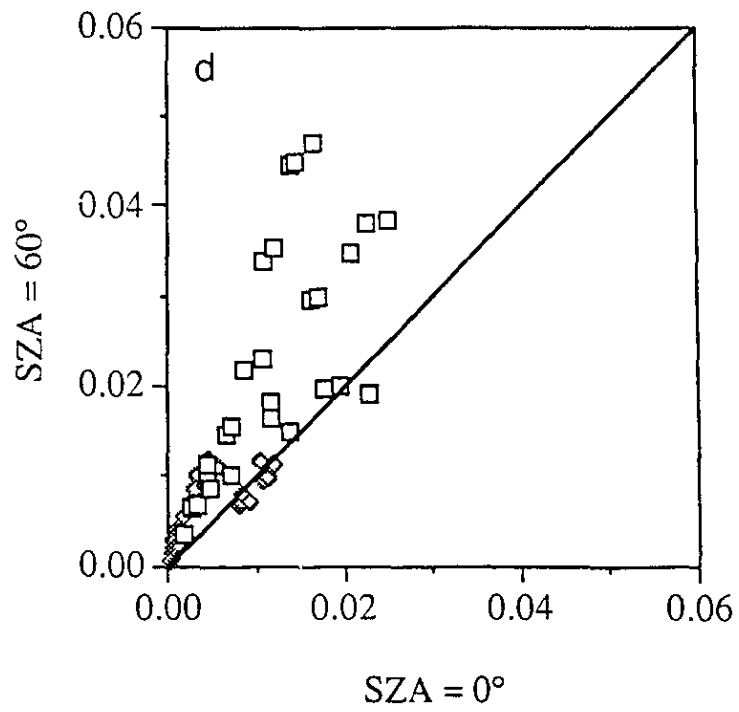
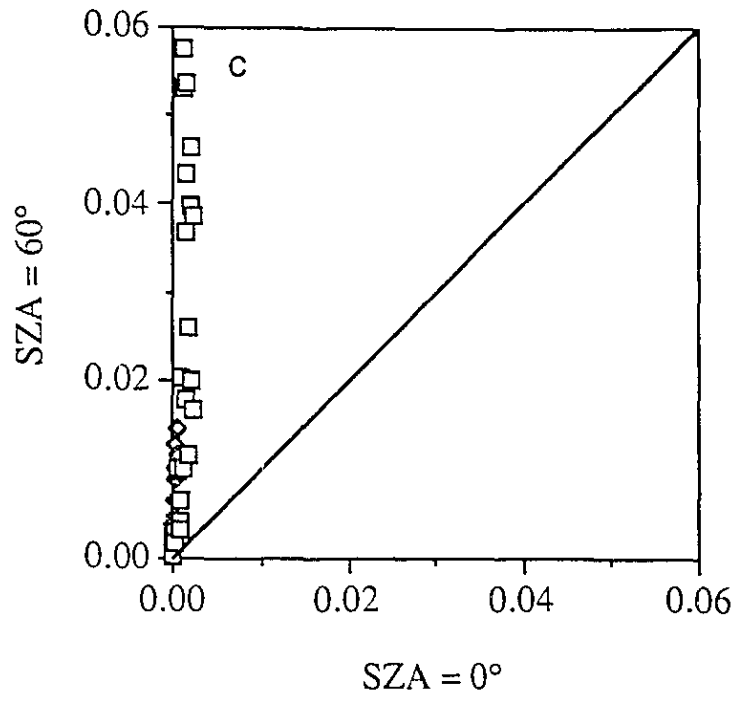
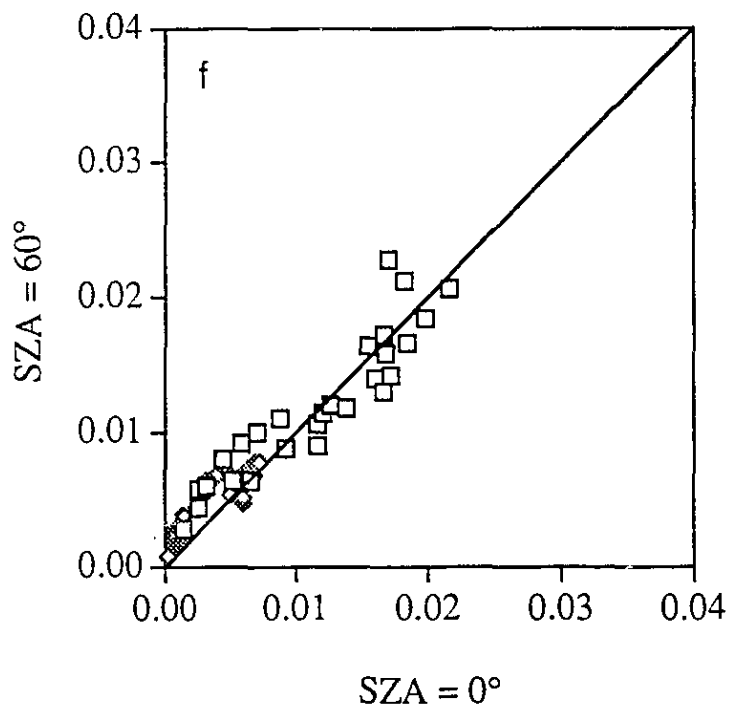
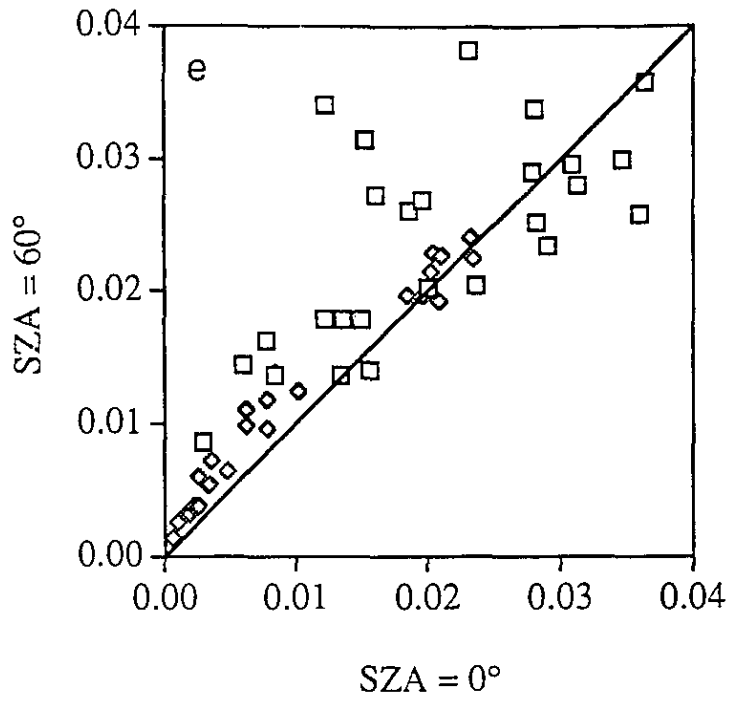
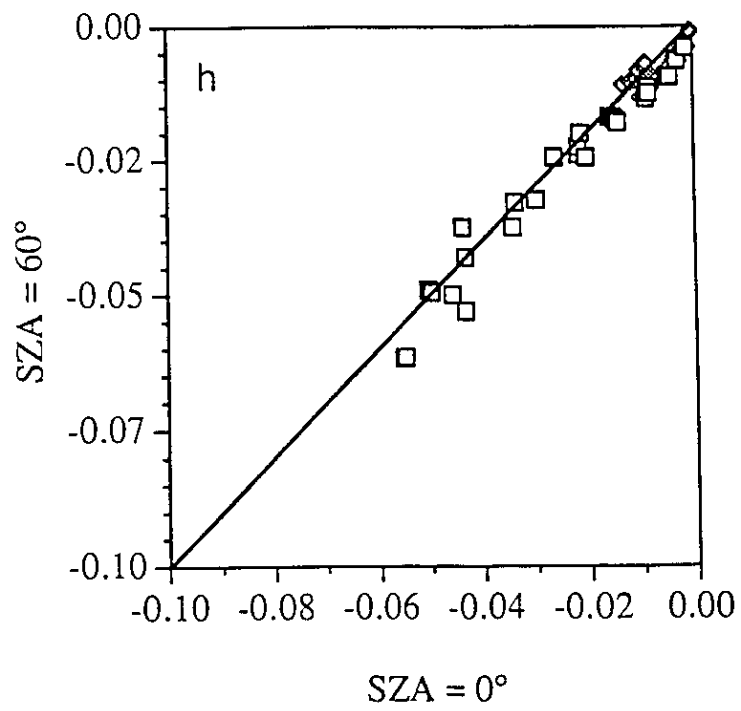
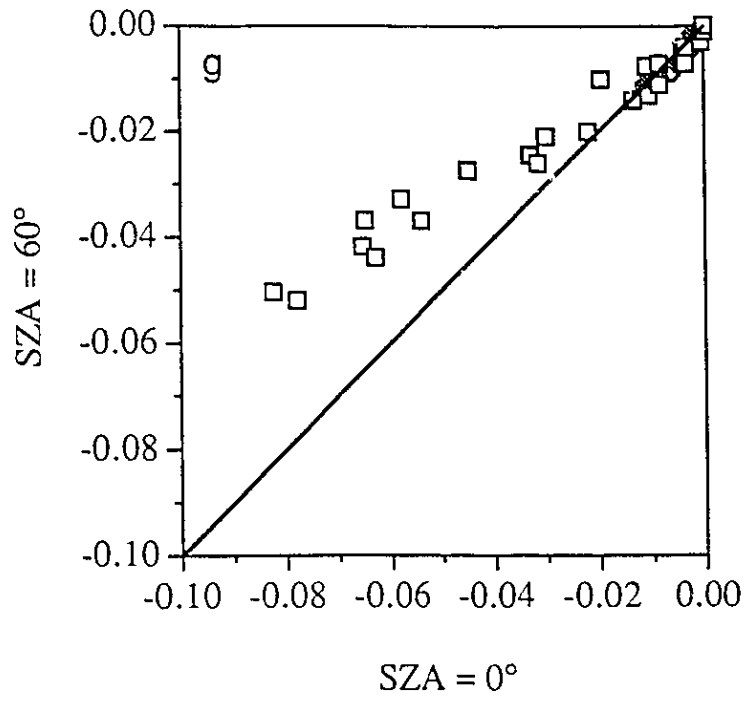


Figure 3.2.16. Influence of 3-D IH effects on scene albedo: (a) upward trapping for CTH variations; (b) upward trapping for VEC variations; (c) downward trapping for CTH variations; (d) downward trapping for VEC variations; (e) upward escaping for CTH variations; (f) upward escaping for VEC variations; (g) downward escaping for CTH variations; (h) downward escaping for VEC variations.







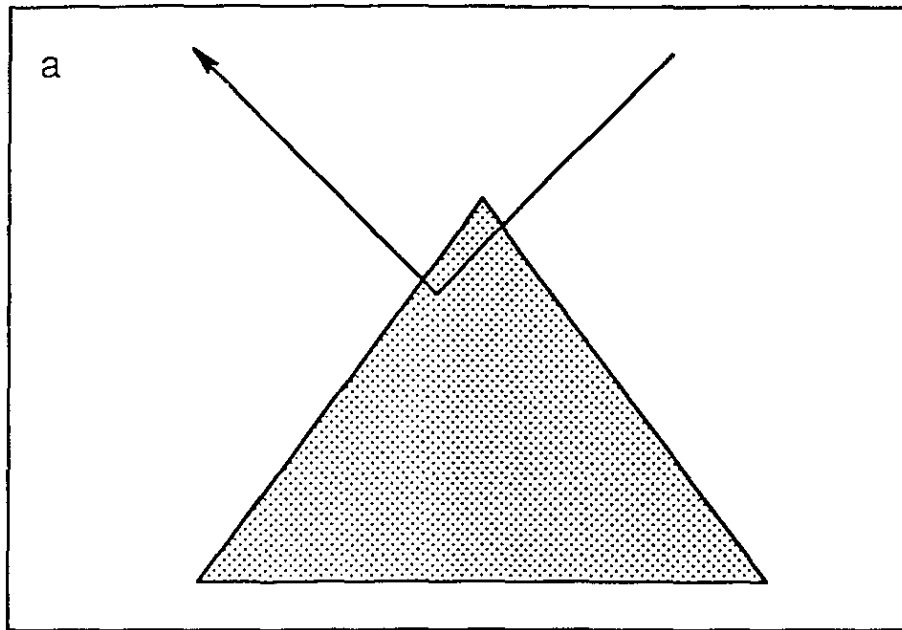
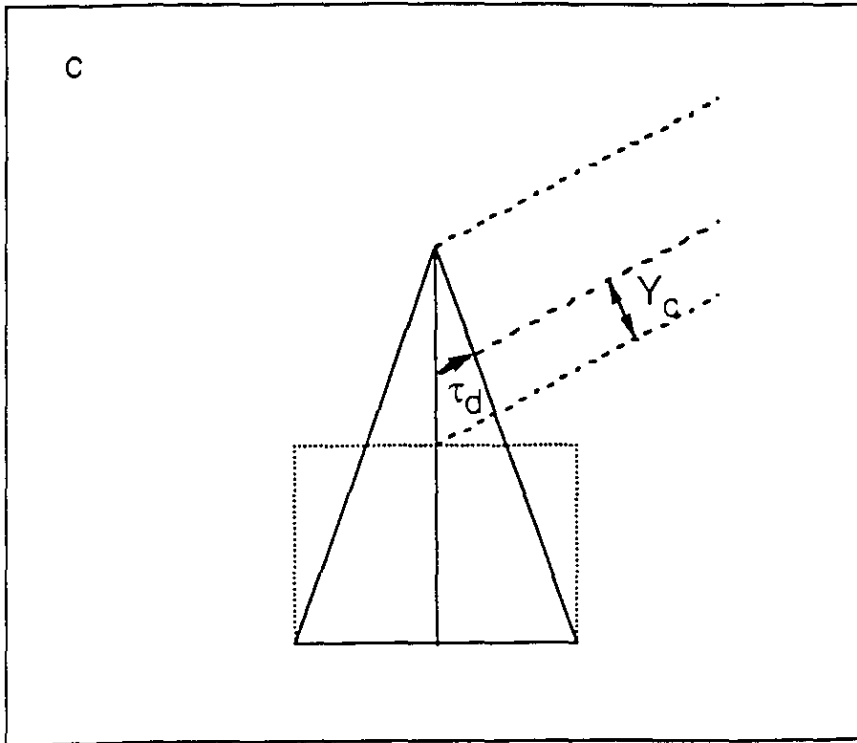
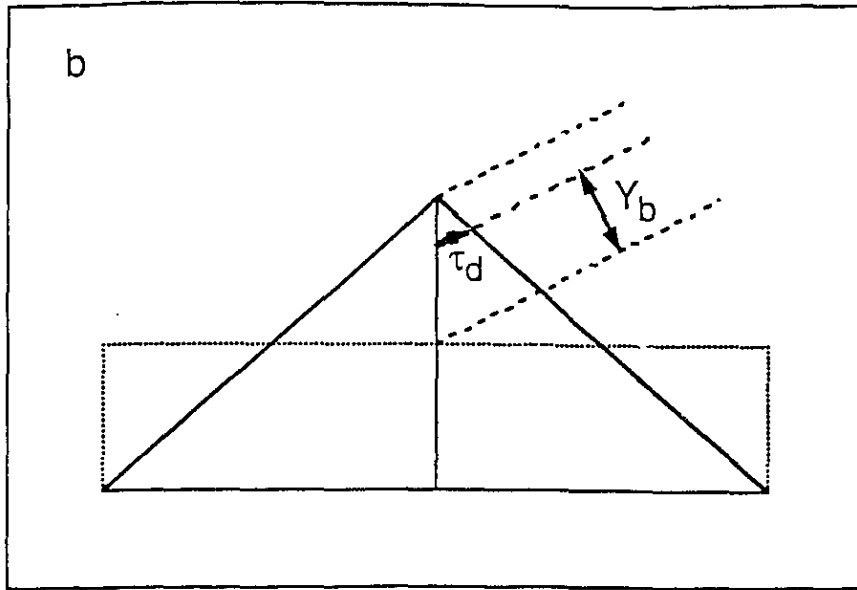


Figure 3.2.17. Influence of cloud side slope on the magnitude of the upward trapping effect: (a) the path of a photon experiencing upward escaping (and not upward trapping) effect; (b) amount of radiation Y_b that is affected by upward trapping if a cloud has CTH variations (thick line), but is not, if a cloud has VEC variations (dotted rectangle). Photons are assumed to descend through τ_d before ascending at the same angle as they reached the cloud: (c) same as (b), but for steeper cloud sides.



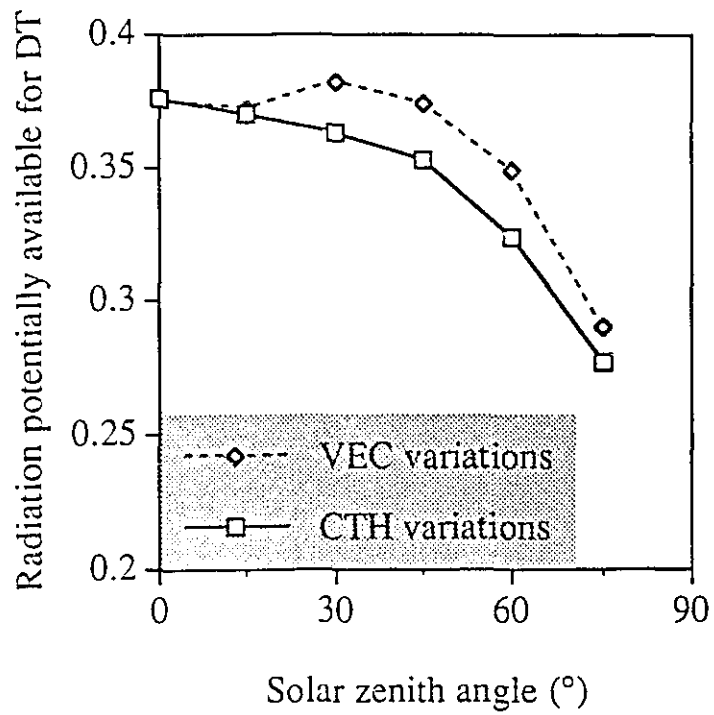


Figure 3.2.18. Amount of radiation potentially available for downward trapping in the case of the cloud field shown in Figure 2.1.1.

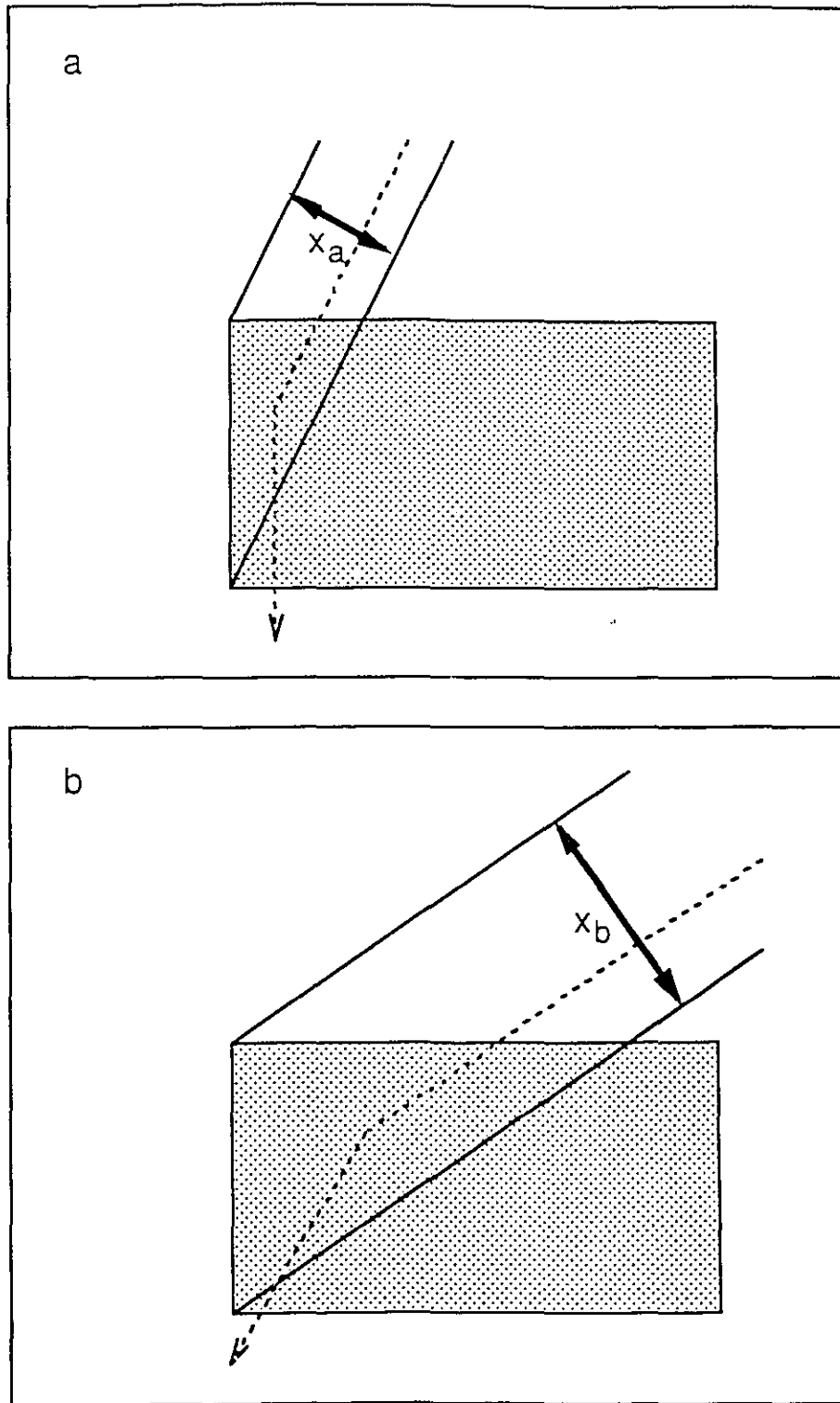


Figure 3.2.19. Amount of radiation (X) that is affected by downward trapping after being scattered at a particular angle: (a) small SZA; (b) large SZA.

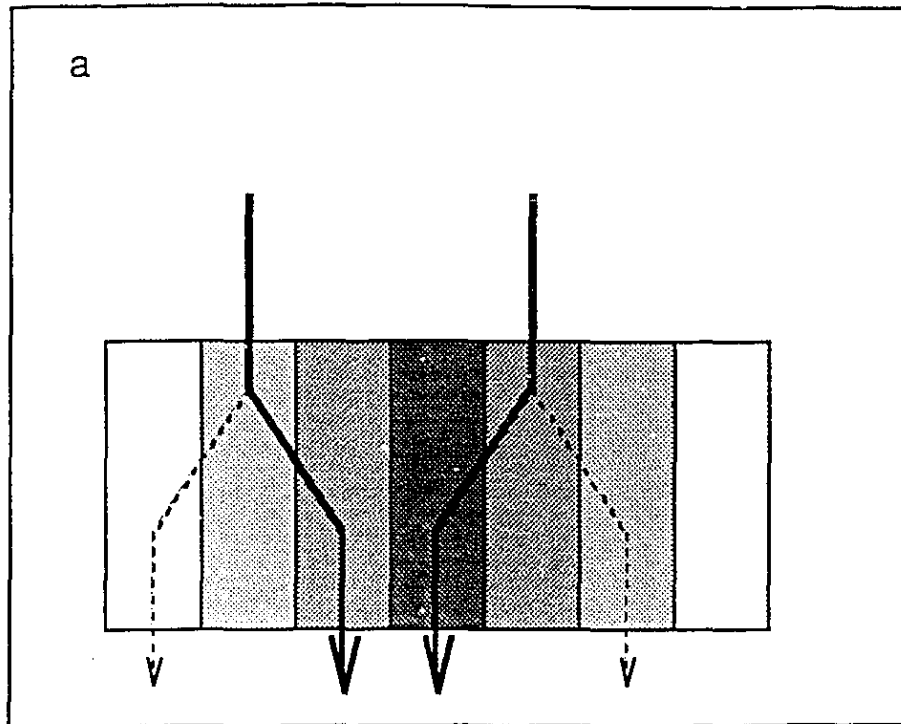
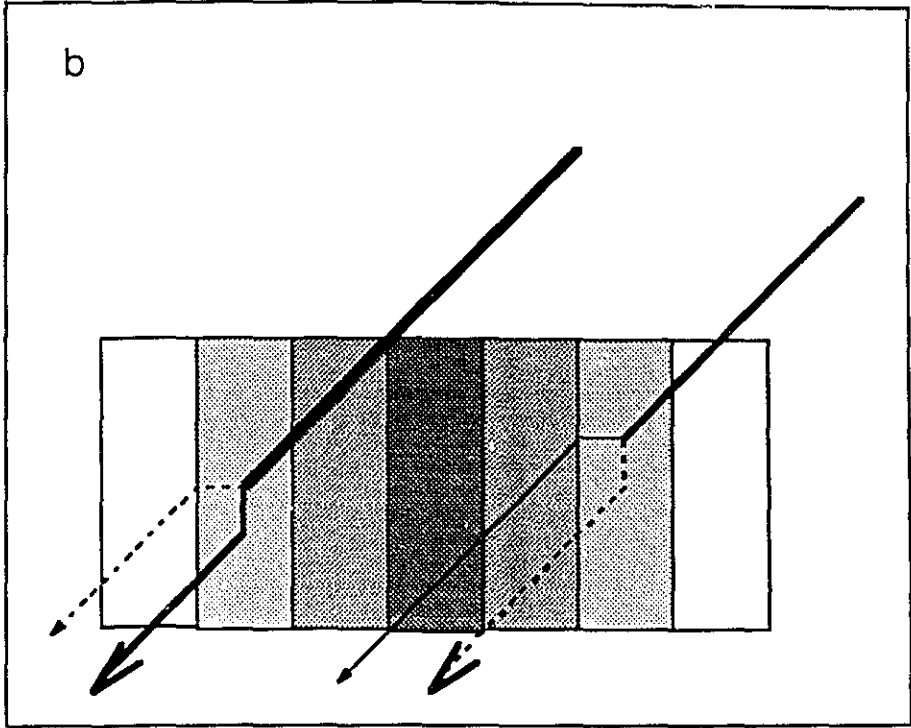
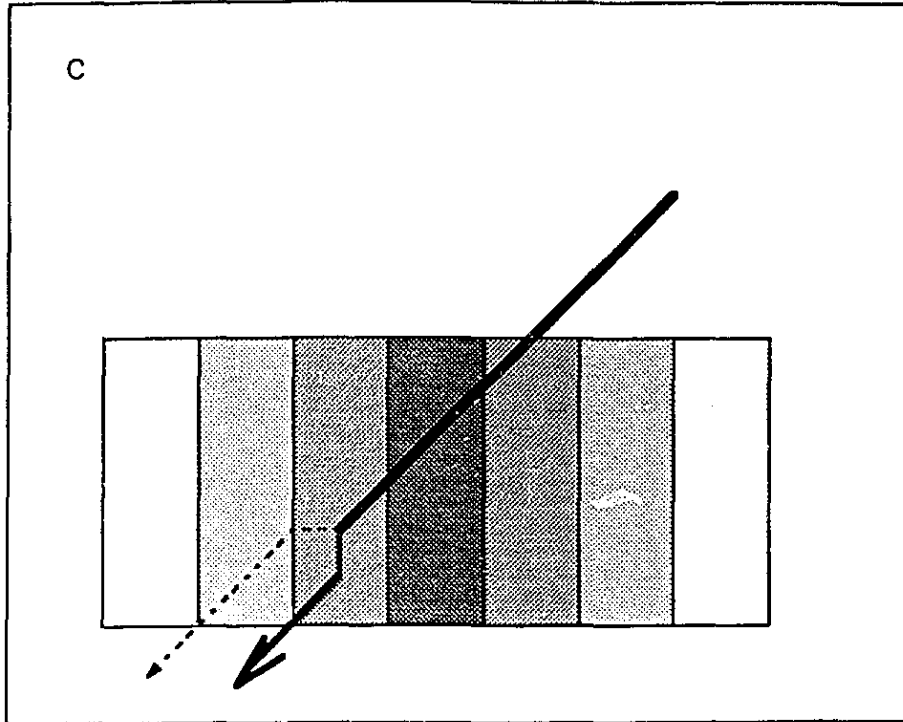


Figure 3.2.20. Downward trapping in clouds with VEC variations. The solid line indicates paths of photons that are affected by downward trapping, the dashed lines, paths of photons that are not. The thickness of each line is related to the number of photons that follows each type of paths: (a) overhead sun; (b) and (c) oblique sun.





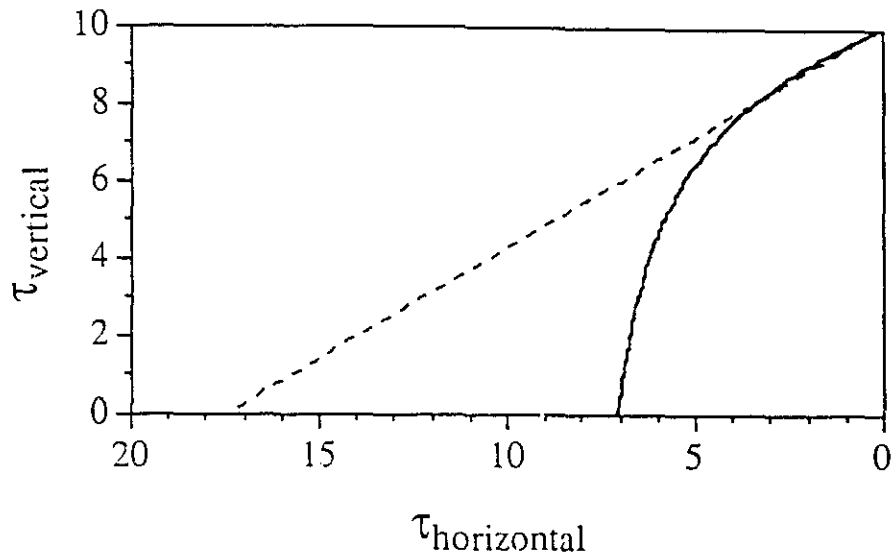


Figure 3.2.21. Forward motion of radiation in a homogeneous cloud. The dashed line indicates the path assumed in the TIPA; the solid line, the average x -coordinate of photons that are eventually transmitted through the cloud (relative to the point where they entered the cloud). The average positions are calculated by 3-D radiative transfer calculations for a cloud with $\tau = 10$ and SZA = 60° . Photons enter the cloud top in a direction parallel to the x -axis.

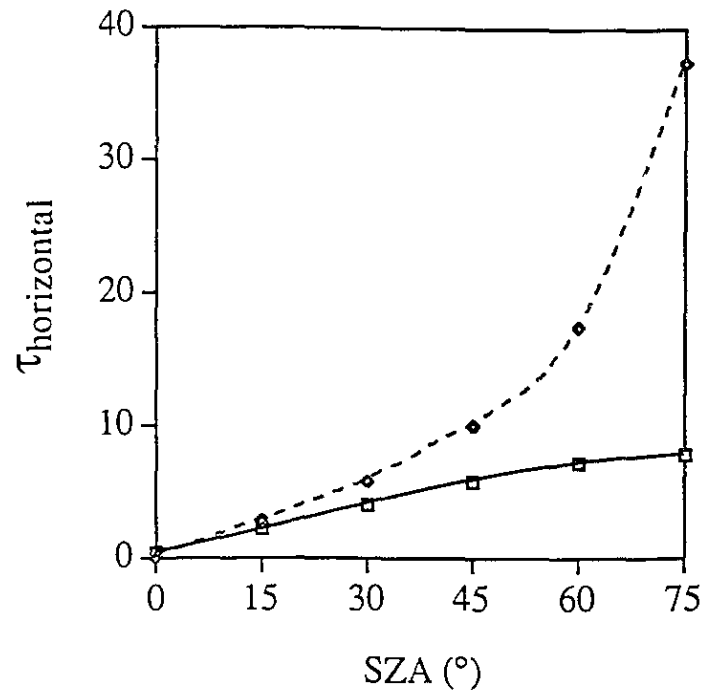


Figure 3.2.22. Average distance between the x -coordinates of points where transmitted photons enter the cloud top and leave the cloud base. The dashed line is the distance assumed by the TIPA, the solid line is obtained through 3-D Monte Carlo simulations for a homogeneous cloud with $\tau = 10$.

Downward escaping

As with upward escaping, the radiation potentially available for downward escaping is that which is intercepted by clouds (regardless of whether it would be reflected without 3-D IH effects), which increases with SZA. Downward escaping, however, affects downward radiation only. Since photons tend to sink into clouds less for larger SZA's, the downward radiation in clouds does not increase with the amount of intercepted radiation; this is probably why downward escaping does not change much with SZA (Figures 3.2.14a and b, and 3.2.16g and h). The slight decrease observed in the case of very inhomogeneous scenes with CTH variations (Figure 3.2.16g) may be explained by considering the scattering angles required for downward escaping. For CTH variations, the minimum scattering angle required for downward escaping increases on the sunlit side of clouds (the side which intercepts a large portion of the total intercepted radiation) (Figure 3.2.23a).¹⁷ In the case of large inhomogeneities (i.e., steep cloud sides) and overhead sun, downward escaping requires forward scattering, whereas for oblique sun, the range of suitable scattering angles shifts toward backscatter directions (Figure 3.2.23b). Since cloud particles scatter predominantly in forward directions (Figure 3.2.24), this backward shift results in a decrease in downward escaping. For smaller inhomogeneities (i.e., less steep cloud sides), the required scattering angles are fairly large even for overhead sun (Figure 3.2.23c), and their backward shift therefore decreases downward escaping much less. Hence, as the SZA increases, downward escaping can be expected to decrease more for the very inhomogeneous than for the moderately inhomogeneous scenes, which is consistent with the tendency in Figure 3.2.16g.

Overall

Here, the influences of SZA on individual 3-D IH effects are synthesized. The first conclusion that can be drawn is that in the case of oblique sun, the overall 3-D IH effect always decreases albedo, even in scenes for which it increases the reflection in the case of overhead sun (Figure 3.2.13). For VEC variations, the dominant effect responsible for this decrease remains the flow of radiation from thick to thin regions (i.e., UE + DE), for all SZA's (Figure 3.2.25a). For CTH variations, however, the flow from thin to thick regions (UT + DT) becomes dominant for oblique sun, even in those scenes where the flow from thick to thin regions dominates for overhead sun (Figure 3.2.25b).

¹⁷For VEC variations, channeling can occur for any scattering angle.

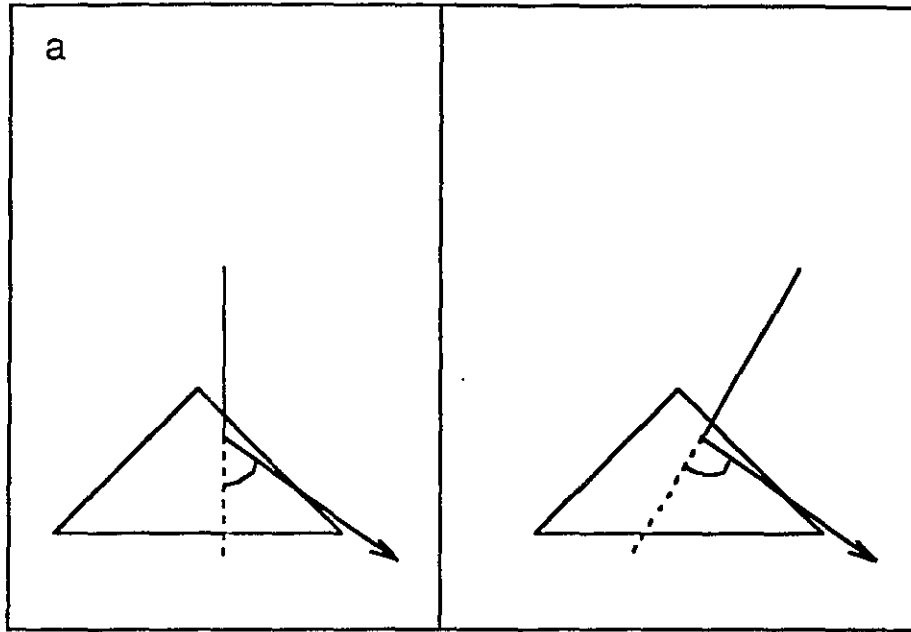
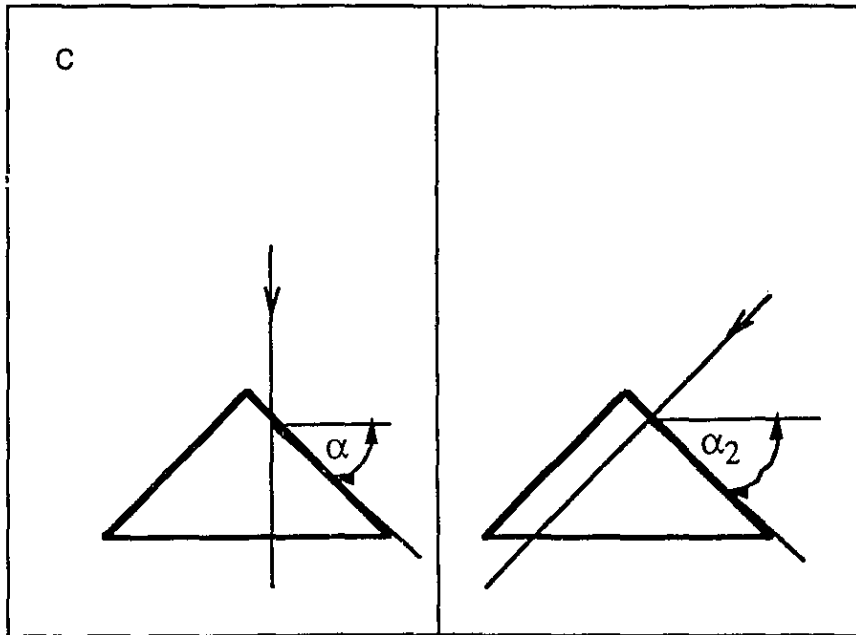
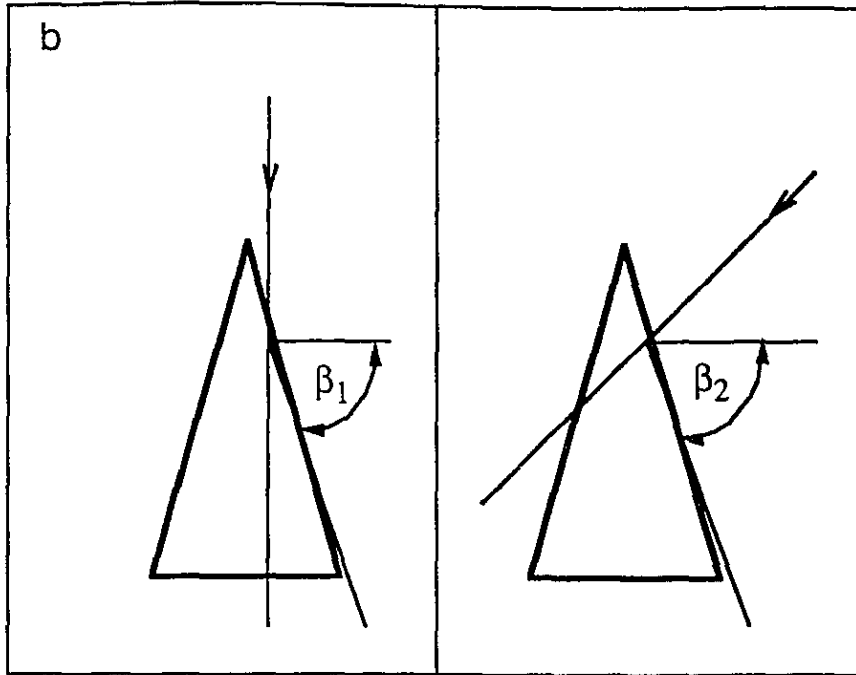


Figure 3.2.23. Scattering angles suitable for downward escaping in the case of CTH variations. (a) minimum required scattering angle; (b) range of scattering angles suitable for overhead and oblique sun (β_1 and β_2); (c) same as (b), but for moderate cloud inhomogeneities.



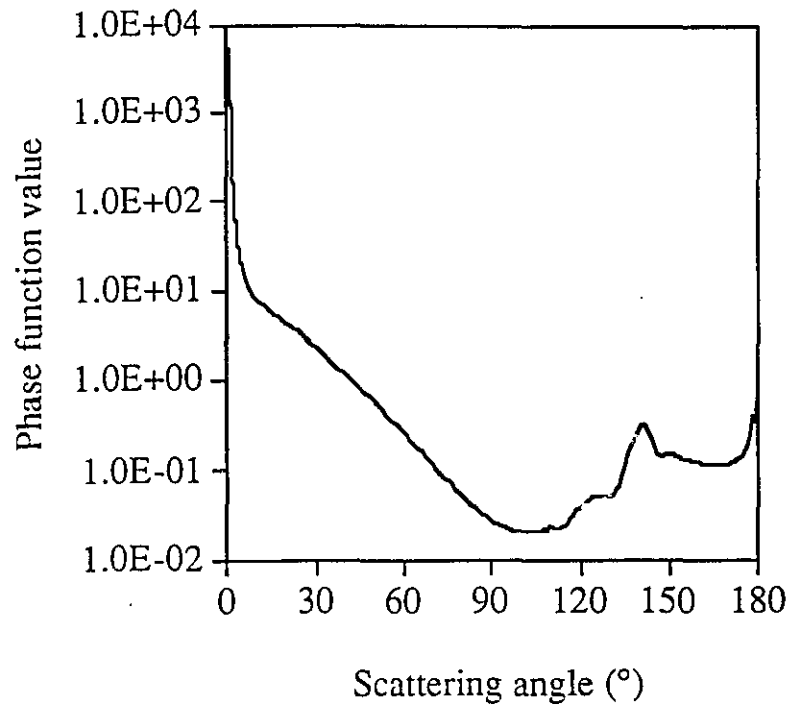


Figure 3.2.24. Mie scattering phase function at 0.865 μm wavelength for a droptype distribution representative of the top of stratocumulus clouds ($r_{\text{modal}} = 10.2 \mu\text{m}$).

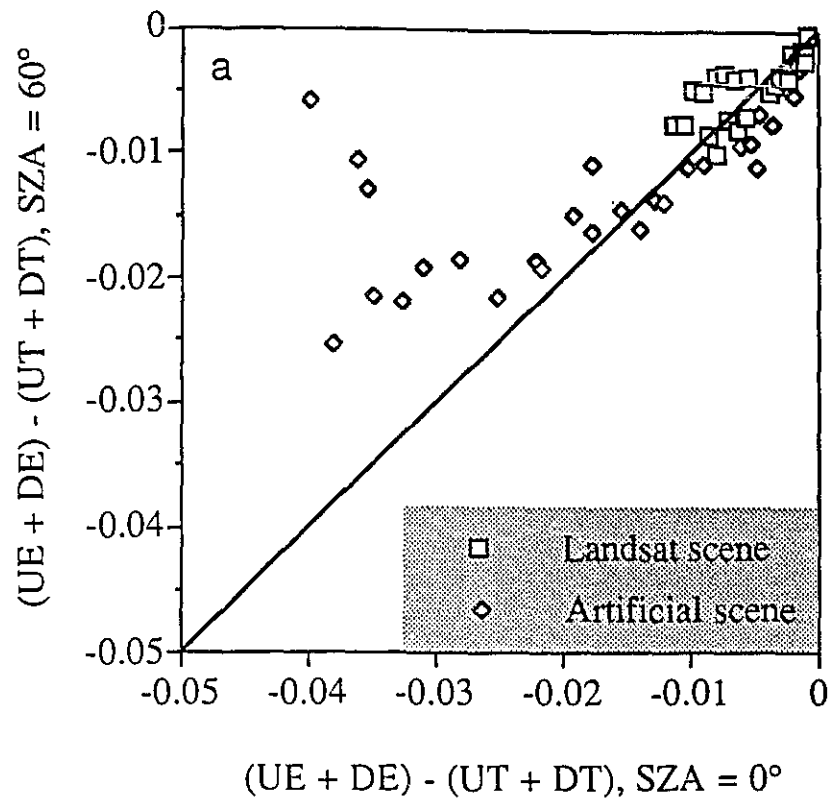
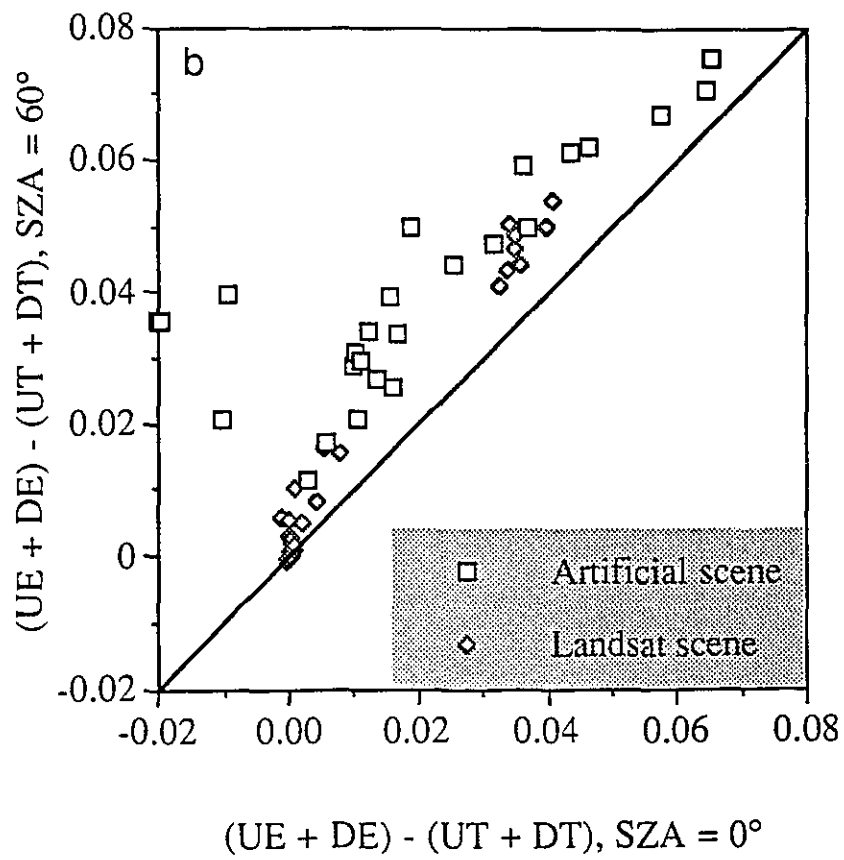


Figure 3.2.25. Comparison of the effects of radiation flowing from thick to thin (UE + DE) and from thin to thick areas (UT + DT). Negative values indicate that the former flow has a larger effect; positive values, that the latter one decreases the scene albedo more. (a) VEC variations; (b) CTH variations.



While for overhead sun, the overall 3-D effect decreases the albedo predominantly by making the transmission of downwelling photons easier (i.e., $DT + DE < 0$), and not by making the reflection of upwelling photons more difficult (i.e., $UT + UE < 0$), this situation tends to reverse for oblique sun (Figure 3.2.26).¹⁸

Figure 3.2.27 shows that, while the overall 3-D effects caused by CTH and VEC variations may differ significantly for oblique sun, the differences tend to be smaller than they are for overhead sun (Figure 3.2.8). These differences are smaller since as the SZA increases, the overall 3-D effect due to CTH variations tends to decrease (Figure 3.2.13), whereas the effects of VEC variations increases (Figure 3.2.28). This opposite behavior can be explained by the fact that, as described above, downward trapping and downward escaping change differently with SZA for the two types of cloud inhomogeneities (Figures 3.2.16c, d, g and h).

3.2.3 Effects of cloud inhomogeneities on nadir reflectance

Numerous studies have shown that cloud inhomogeneities affect not only the amount of radiation reflected, but also its angular distribution (see Section 1.3). Therefore, cloud inhomogeneities may affect reflection in various directions differently. This section examines how inhomogeneities affect nadir reflectance in particular.

Loeb and Davies (1996b) used measurements of the Earth Radiation Budget Satellite Narrow Field of View (ERBS NFOV) instrument to examine how nadir reflectance of real clouds varies with SZA. According to 1-D radiative transfer theory, nadir reflectance (BRF) should decrease as the SZA increases. The reason for this decrease is that cloud particles scatter light predominantly in near-forward directions, and thus for high SZA, plane-parallel clouds tend to reflect the most radiation into oblique forward directions. However, when Loeb and Davies (1996b) averaged all water clouds observed over the oceans between latitudes 30° North and 30° South, they found that nadir reflectance does not decrease, but increases with SZA (Figure 3.2.29, their Figure 4). Loeb, Várnai and Davies (1996) have suggested that this unexpected behavior may be due to cloud inhomogeneities. This section examines whether CTH and / or VEC variations can cause

¹⁸Figure 3.2.29b shows that the situation does not reverse for some scenes with VEC variations. However, the overall 3-D effect is very small, i.e., less than 0.0025 for all such scenes. Hence, the above conclusion is still valid for all scenes in which the albedo is affected significantly by 3-D IH effects.

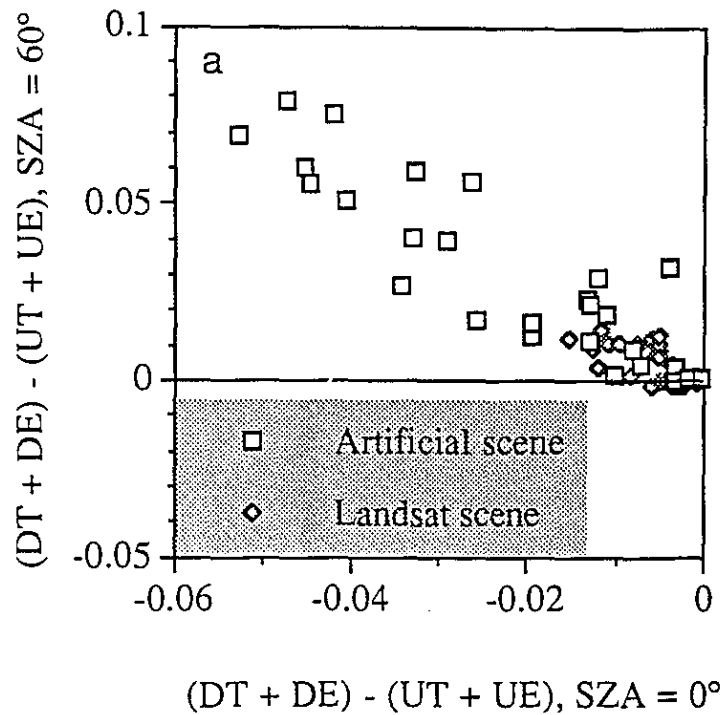
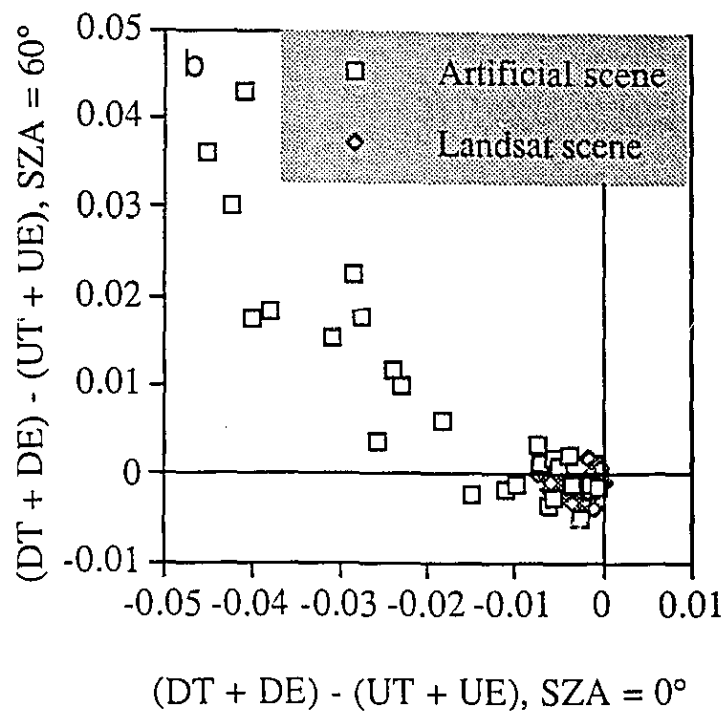


Figure 3.2.26. Comparison of the influence of 3-D IH effects on scene albedo by affecting transmission (DT + DE) and reflection (UT + UE). Negative values indicate that the albedo is decreased mainly by 3-D IH effects easing the transmission of radiation; positive values, that the albedo is decreased mainly by 3-D IH effects making cloud reflection more difficult. (a) CTH variations; (b) VEC variations.



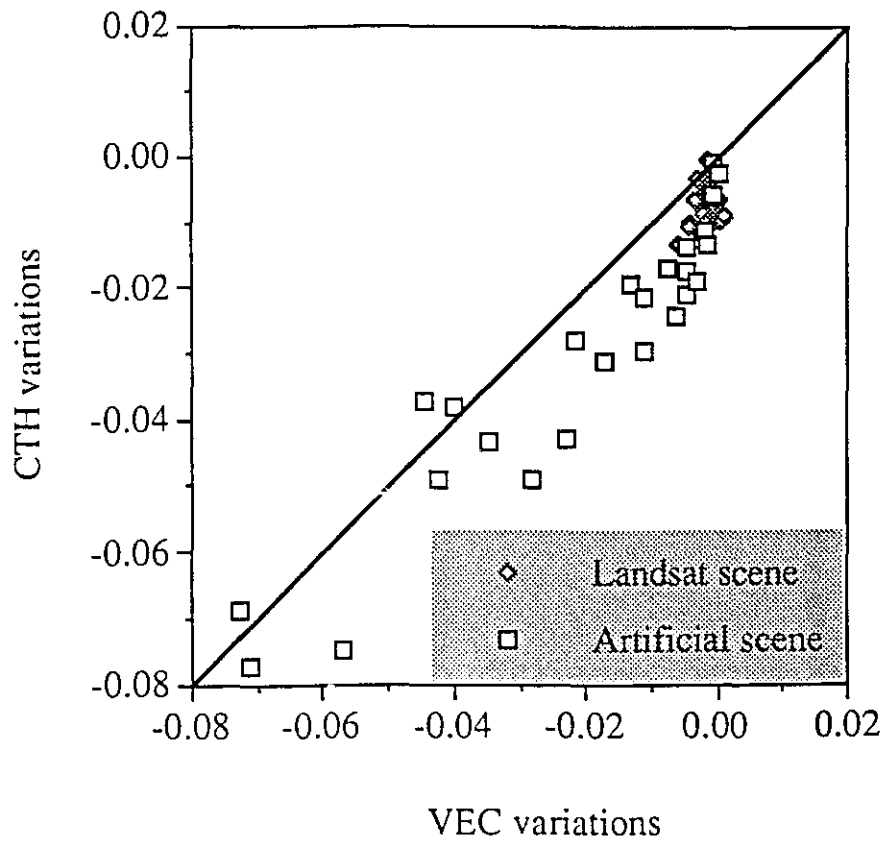


Figure 3.2.27. Overall 3-D IH effects due to CTH and VEC variations at $SZA = 60^\circ$.

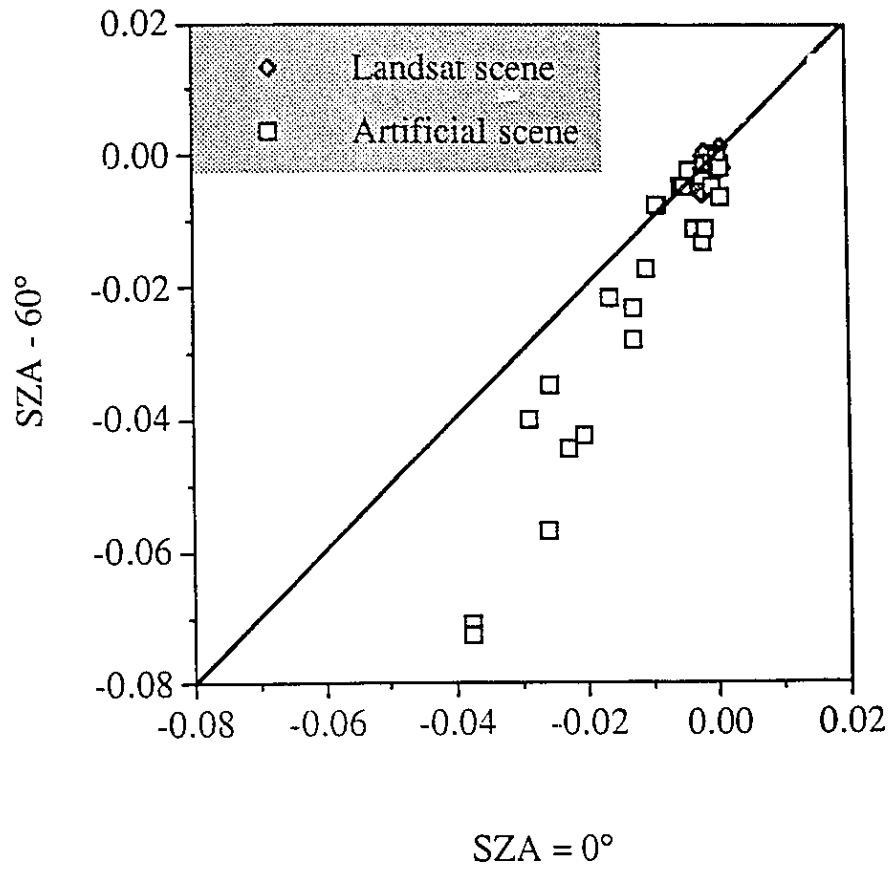


Figure 3.2.28. Overall 3-D IH effects caused by VEC variations at SZA = 0° and 60°.

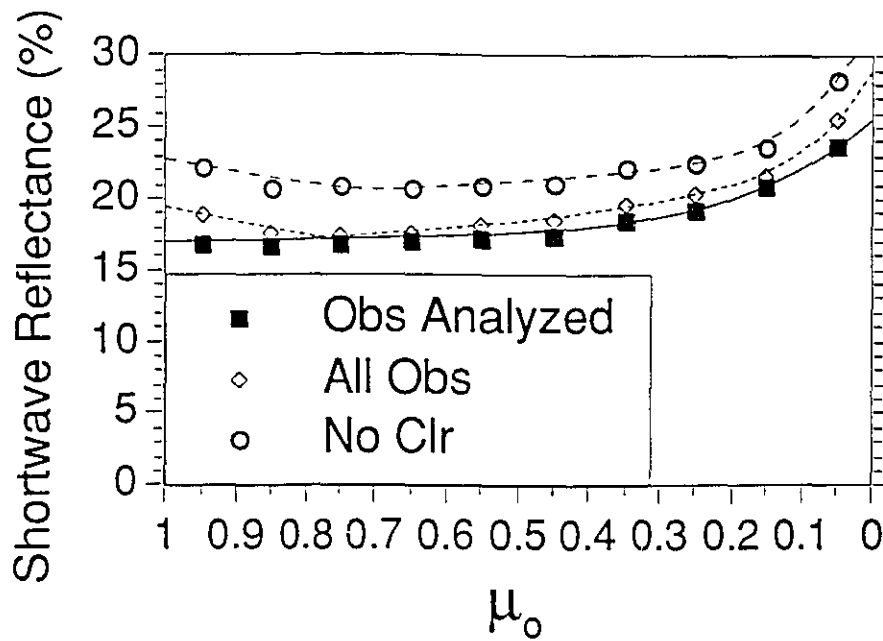


Figure 3.2.29. One-year average observed shortwave reflectances versus μ_0 (= $\text{COS}(\text{SZA})$) for pixels that were not rejected as either being clear or containing thick ice clouds (“Obs Analyzed”), and for all observations throughout the year (“All Obs”). Figure copied from Loeb and Davies (1996b).

such an increase, and if so, through what mechanisms. This question is addressed through the example of a cloud field generated using the same input parameters as in Loeb, Várnai and Davies (1996): $CF = 0.75$, $\langle \tau \rangle = 10$, $VEC = 30 \text{ km}^{-1}$, $s_{(k)} = 1$ if $k \leq 6$, and $s_{(k)} = 3.6$ if $k > 6$.¹⁹

The results shown on Figure 3.2.30 indicate that nadir reflectance increases sharply with SZA for CTH variations, increases much less for VEC variations, and, as expected, decreases for homogeneous clouds. One reason for the differences is that as the SZA increases, inhomogeneous clouds intercept more and more solar beams, and thus make more radiation potentially available for nadir reflection. Figure 3.2.31 shows that when $\text{COS}(SZA)$ decreases from 1 to 0.15, this effect (calculated using the TIPA) is responsible for about 15 and 20% of the nadir reflectance's deviation from a single homogeneous cloud layer for CTH and VEC variations, respectively. The rest of the differences are due to changes in 3-D IH effects, especially a large increase in upward trapping and a smaller increase in downward trapping (Figure 3.2.32). Both these effects act to scatter radiation after it would have already left a plane-parallel cloud; they reduce the radiation that goes in the forward direction, and distribute it in all directions, thereby increasing nadir reflectance.²⁰ Section 3.2.2 discusses the reasons these two effects increase more for CTH than for VEC variations, and the other two effects (upward escaping and downward escaping) remain fairly constant.

Downward trapping and the sum of two other 3-D effects (upward escaping and downward escaping) change fairly similarly for both CTH and VEC variability. As described in Section 3.2.2, however, upward trapping increases much more for CTH than for VEC variations. Therefore, one can say that for this cloud field, downward trapping and the 1-D IH effect counterbalance the decrease in nadir BRDF expected for homogeneous clouds, while changes in upward trapping cause the various increases obtained for the two inhomogeneity types.

Comparison of Figures 3.2.29 and 3.2.30 could suggest that the observed behavior in nadir cloud reflection is most similar to the behavior of clouds with VEC variability. However, since the observational results include many measurements of truly homogeneous cloud scenes, the decrease for these homogeneous scenes must be

¹⁹Since the generation process uses some random numbers that are different in the two studies, using the same input parameters does not result in identical, only statistically very similar, cloud fields.

²⁰For oblique sun, upward trapping affects nadir reflectance and albedo in opposite ways: it enhances the former, while it decreases the latter, predominantly by reducing reflection in the forward direction.

counteracted by a strong increase for the inhomogeneous scenes. Thus it appears more likely that CTH, rather than VEC variations are responsible for the behavior observed by Loeb and Davies (1996b).

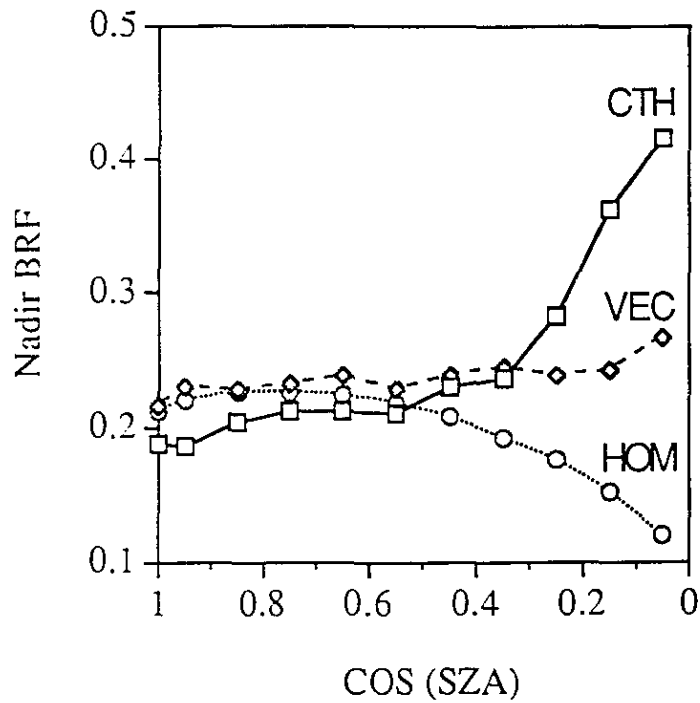


Figure 3.2.30. Nadir reflectance (BRF) as a function of SZA for scenes with CTH (solid line) and VEC variations (dashed line), and for a scene that contains a homogeneous cloud (dotted line).

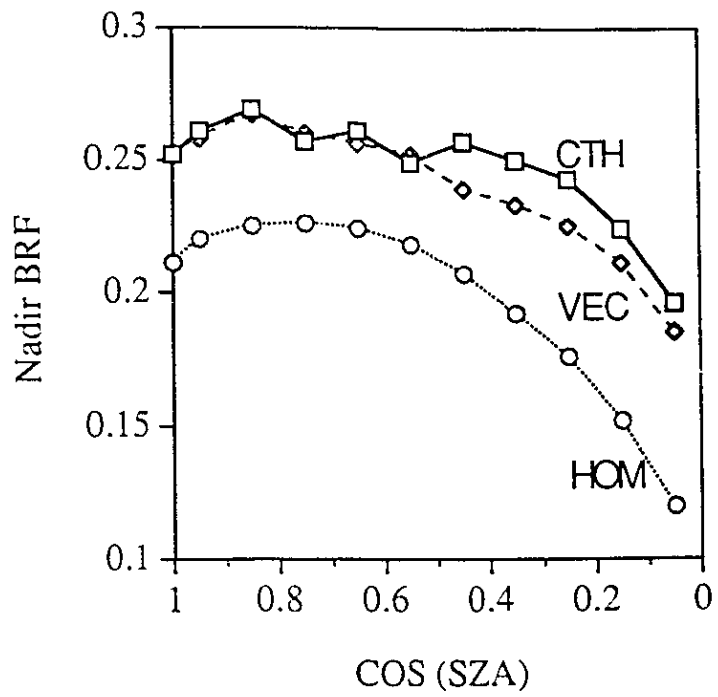


Figure 3.2.31. Nadir reflectance for the same scenes as in Figure 3.2.30., but calculated using the TIPA instead of 3-D Monte Carlo simulations.

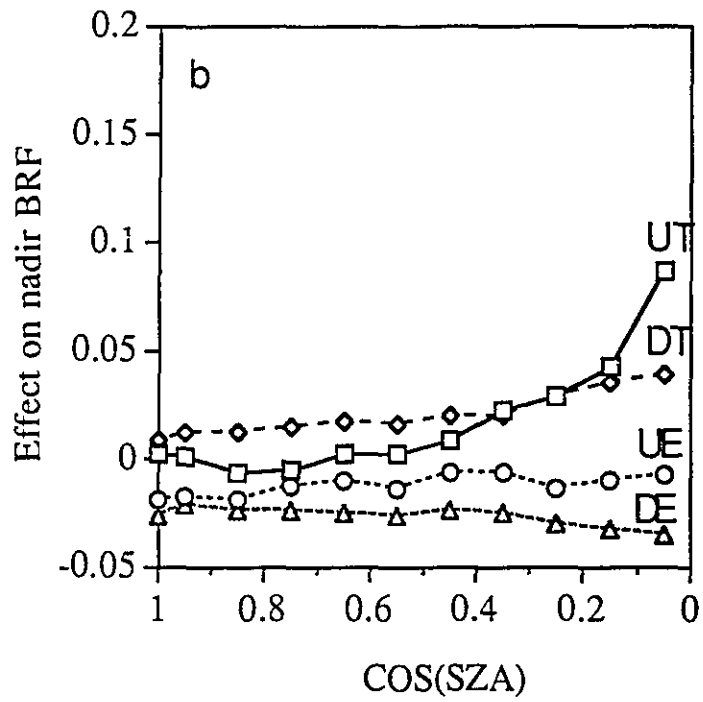
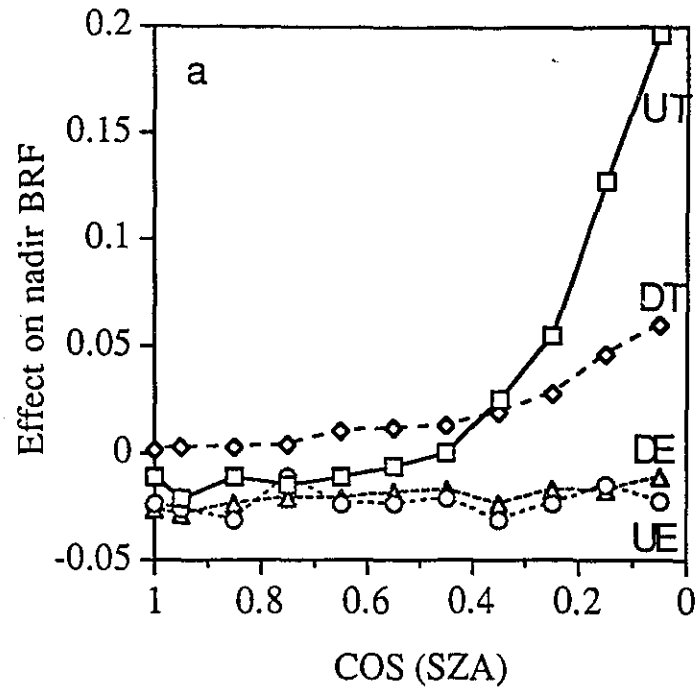


Figure 3.2.32. Influence of 3-D IH effects on nadir reflectance. (a) CTH variations; (b) VEC variations.

Chapter 4

An Algorithm for Albedo Retrievals using Multi-View Satellite Data

One of the main goals of the work presented in this thesis is to improve our ability to measure the albedo of inhomogeneous clouds. In particular, a new algorithm has been developed to take advantage of the multi-view capability of the future satellite instrument MISR. Although the algorithm has been developed with MISR in mind, it can be adapted easily to other future multi-view instruments. This chapter describes this algorithm and examines the improvements it may offer over present albedo-estimation methods. The outline of the chapter is as follows.

Section 4.1 describes the albedo products that will be generated during the routine processing of MISR data. The general approach of the proposed albedo-retrieval method is outlined in Section 4.2. Section 4.3 describes the database built for the retrievals, while Section 4.4 outlines the way appropriate coefficients from the database can be assigned to actual measurements. Finally, Section 4.5 presents some preliminary estimates about how much the new algorithm can be expected to decrease the uncertainties of present albedo estimates.

4.1 Standard MISR Albedo Products

The Earth Observing System (EOS) will provide the scientific community not only with raw measurements, but also with various products generated through routine processing of satellite data. The goal of this processing is to make the measurements easier to use by freeing potential users of some basic processing tasks.

For the MISR instrument, the standard products will include calibrated and geographically registered reflectance (BRF) values, cloud masks, and various surface, aerosol and cloud properties. As part of the routine data processing, three separate albedo values will be

produced for each MISR-wavelength. The three albedos can be interpreted through another standard product, the Reflecting Layer Reference Altitude (RLRA), i.e., the altitude at which the main part of solar reflection in a 2.2×2.2 km area occurs.

The concept of the RLRA is needed to match up data from the nine cameras so that they show the same objects, and hence make full use of MISR's multi-view capability. As Figure 4.1.1 shows, this process requires knowledge of the altitude from which the radiation comes. Strictly speaking, the concept of RLRA does not imply that almost all reflection occurs at the same level. It only assumes that the reflection above and below the RLRA does not vary significantly in horizontal directions. This assumption avoids the complication that some of the radiation measured by the nine cameras comes from different objects for each camera. For clear pixels, the RLRA is set to the surface elevation, and for cloudy pixels, to the cloud top height. The way the RLRA will be calculated is described in detail in Diner et al. (1995c).

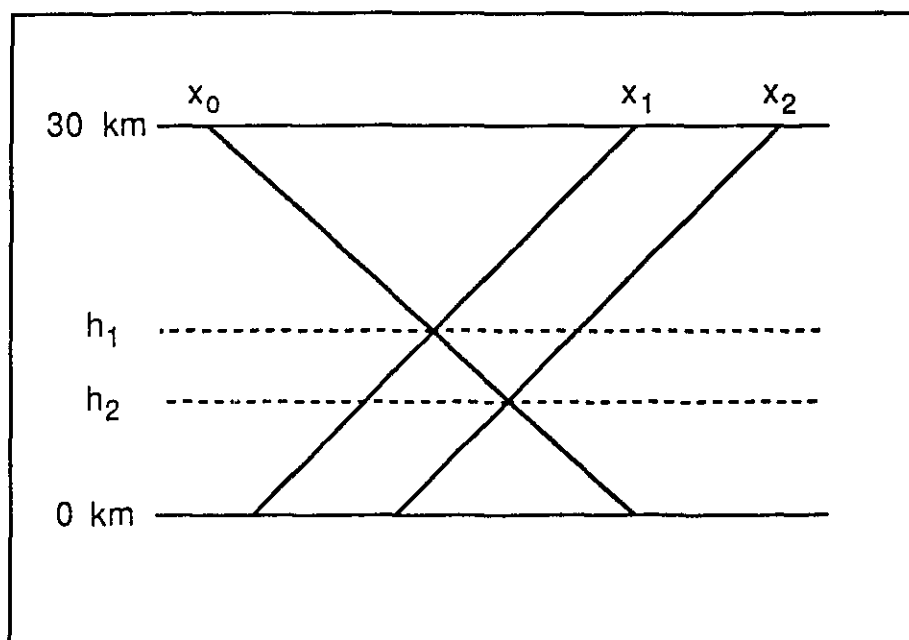


Figure 4.1.1. The matching of multi-angle measurements using the concept of RLRA. Depending on whether the RLRA is at level h_1 or h_2 , the measurement of the C_{fwd} camera taken at point x_0 is matched with the measurement taken by the C_{aft} camera at points x_1 or x_2 , respectively.

Since single-view instruments do not face the problem of matching various cameras, their observations are usually registered to some constant reference altitude, for example, 30 km above sea level. This feature has been used by the MISR science team in defining the three standard albedo products.

The first product, *fine albedo*, is intended mainly for small-scale and local studies. It is calculated at 2.2 km spatial resolution and is registered at the RLRA. The exact definition of this product is

$$A_{fine} = \frac{b+c}{d},$$

where d is the downward solar flux through a 2.2 x 2.2 km area at the top of atmosphere (TOA), b is the portion of d that is reflected back to space by air above the RLRA, and c is the portion of d that emerges through the RLRA and subsequently leaves the atmosphere to space (without passing through any other RLRA's).

The second product, *coarse restrictive albedo*, is intended mainly for regional and global climate studies, and is most comparable to albedos produced by single-view instruments.¹ Like the fine albedo, this albedo is registered to the variable level of the RLRA, but it is calculated at a coarser, 35.2 km resolution. However, it is not equal to the average of fine albedos over the same area. The difference is that fine albedos only include radiation that leaves through the top of columns which reach from the surface to the RLRA, whereas the coarse albedo also includes the radiation that leaves through the sides of these columns. The exact definition of the coarse restrictive albedo is

$$A_{restrictive} = \frac{b}{d},$$

where d is the downward solar flux through a 35.2 x 35.2 km area at the TOA, and b is the portion of d that is reflected to space by any object within a 35.2 x 35.2 km column reaching from the surface to the TOA.

¹Vonder Haar (1983) emphasizes the importance of the continuity of satellite radiation measurements.

The main purpose of the third albedo product is to be compared to albedos produced by single-view instruments. This *coarse expansive albedo* is also calculated at a 35.2 km resolution, but registered to a constant 30 km altitude. Its exact definition is

$$A_{\text{expansive}} = \frac{b}{d},$$

where d and b are downward and upward solar fluxes through a 35.2 x 35.2 km area at the TOA (assumed to be 30 km above sea level). Although this definition is closest to the albedo definitions used by some single-view instruments (for example, ERBE), the expansive albedo has much smoother spatial variations. The lack of sharp contrasts is due to interactions among nearby regions. For example, parts of the radiation reflected from a bright cloud may go over nearby dark areas by the time the radiation reaches the 30 km altitude (Figure 4.1.2).² To account for this interaction, expansive albedos are calculated in two steps. First, the reflection is calculated at the RLRA, and then it is projected upward to the appropriate 30 km level pixels.³

The main goal of Chapter 4 is to investigate a problem essential to retrieving all three albedos. This problem is that of angular integration, i.e., how to use knowledge of radiation reflected in nine directions to infer the total radiation reflected in all directions.

4.2 General Approach

A convenient form of angular integration for all three MISR albedo retrievals is linear regression:

$$A = \sum_{k=1}^9 a_k BRF_k + \varepsilon \quad k = 1, 2, \dots, 9 \quad (4.2.1)$$

²Since the coarse restrictive albedo does not consider these interactions, its values are more similar to albedos produced by single-view instruments.

³Parts of the radiation crossing the 30 km altitude near the swath edge come from outside the swath measured by MISR. This radiation can be accounted for by assuming that areas just outside the swath reflect the same way as areas just inside.

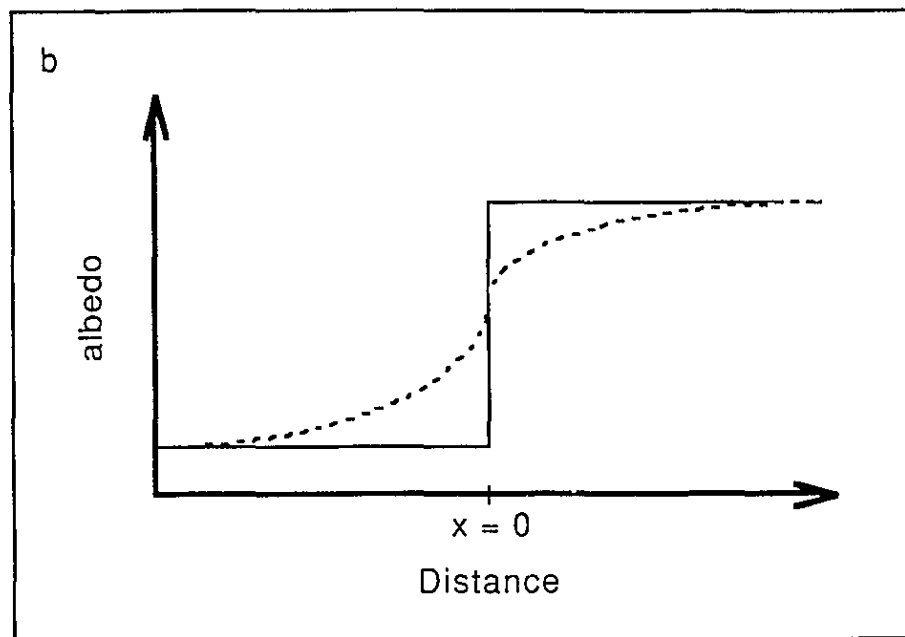
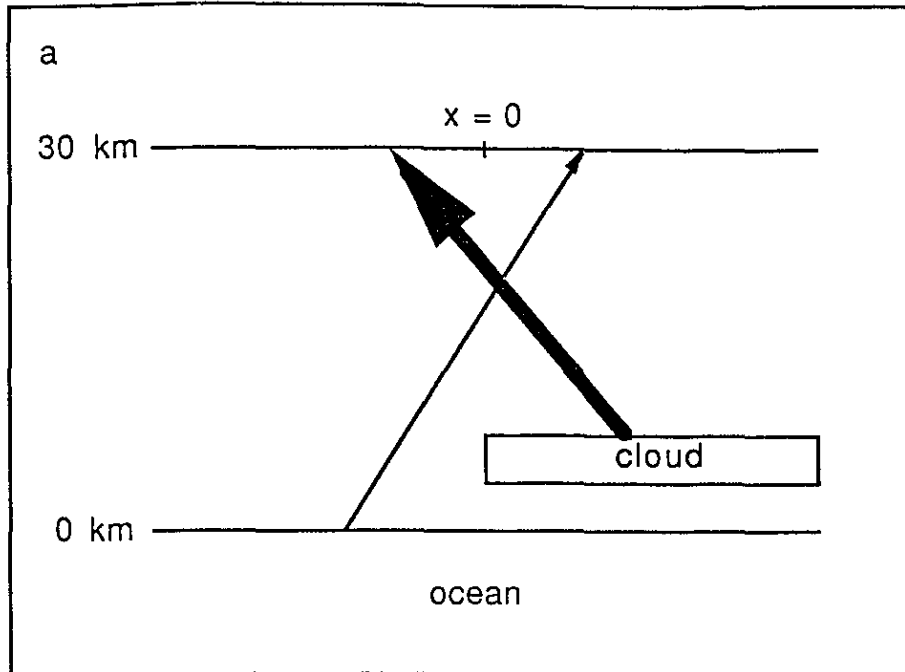


Figure 4.1.2. Radiative interactions among neighboring regions: (a) cross section of a scene (the arrows represent reflected solar radiation); (b) restrictive albedo registered at the RLRA (solid line) and expansive albedo registered to 30 km altitude (dashed line).

where k is the MISR camera index number,⁴ BRF_k is the reflectance measured by each camera, and a_k and ε are empirical coefficients. The simplest way to obtain these coefficients is to divide the upward hemisphere into nine segments so that each segment contains one MISR camera view, and assume Lambertian reflection within each segment. A convenient way is for each segment (except the top one) to be a half-ring on either side of the solar plane. These half-rings can be separated about halfway between the viewing zenith angles of neighboring MISR cameras, at $\mu = 0.4, 0.6, 0.8$ and 0.96 (Figure 4.2.1). In this case, ε is zero and the a_k values depend only on the solid angles covered by each segment, i.e., on the energy that would be reflected into each segment by a Lambertian reflector with an albedo of 1. Unfortunately, this *energy weighting scheme* can lead to large biases in retrieved cloud albedo values. The reason for the biases can be understood from the following argument.

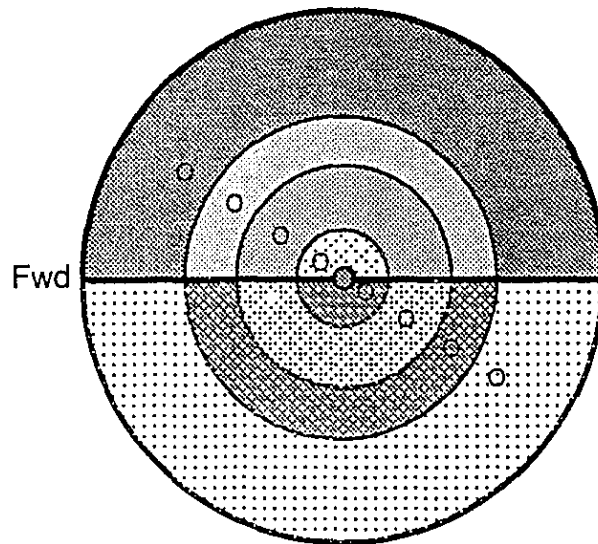


Figure 4.2.1. Division of the upward hemisphere into nine segments for the energy weighting scheme. The distance from the center is proportional to the cosine of the viewing zenith angle μ , and the direction from the center indicates the azimuth relative to the solar plane (forward scattering is on the left side). The small circles identify the view angles measured by MISR at 30° relative azimuth.

⁴ $k = 1$ indicates the D camera which measures forward reflection from a scene, $k = 2$ the C camera next to it, ..., and $k = 9$ the D camera which measures backward reflection.

Since the nine MISR measurements are taken along a fairly constant azimuthal plane, the reflection's zenith angle dependence along this azimuth can be measured fairly well. Thus the main uncertainty of angular integration is in estimating how reflected radiation varies with azimuth (Figure 4.2.2). A comparison of Figures 4.2.2a and b shows that the azimuthal variation is influenced substantially by cloud properties. The main factors determining the azimuthal dependence of cloud reflection are solar elevation, cloud thickness and structure, and the single-scattering properties of cloud particles. But comparison of Figures 4.2.2a and b also reveals features common to most clouds: reflection peaks in forward and/or backscatter directions. These peaks are due to respective peaks in the scattering phase function of cloud particles and, if present, to cloud inhomogeneities (Davies 1984). The biases of the energy weighting scheme are due mainly to these peaks. For example, if MISR measures near the solar plane, the scheme assumes that the high reflectance values detected by oblique cameras occur over all azimuths, and thus overestimates the true albedo. If, however, MISR measures far from the solar plane, the scheme completely ignores the existence of peaks, and thus underestimates the real albedo (Figure 4.2.3).⁵

These biases can be avoided only by using more realistic angular models for cloud reflection. There are two main approaches for generating such models. The first approach is to use theoretical cloud models. This strategy has been followed by the International Satellite Cloud Climatology Project (ISCCP), which used plane-parallel cloud models in satellite retrievals (Rossow et al. 1985). The second approach is to combine large numbers of observations from various view angles to obtain "average" angular distributions. This statistical approach has been chosen in the Earth Radiation Budget Experiment (ERBE) (Taylor and Stowe 1984).

The sun-synchronous orbit of EOS-AM satellites prohibits using the statistical approach. The problem is the correlation between solar elevation and the relative azimuth of MISR-measurements. For example, all MISR measurements for 60° solar zenith angle will be about 20° - 30° off the solar plane, while reflection to larger azimuths will never be measured. Thus, there would be no data with which to construct a reflection model for oblique views at large azimuth angles.

⁵Some simple azimuthal models lead to the same result as solid angle integration. Such models include the assumption of linear or cosine-like azimuthal variations [$BRF_{(\mu,\varphi)} = c_{(\mu)} + d_{(\mu)}\cos(\varphi)$].

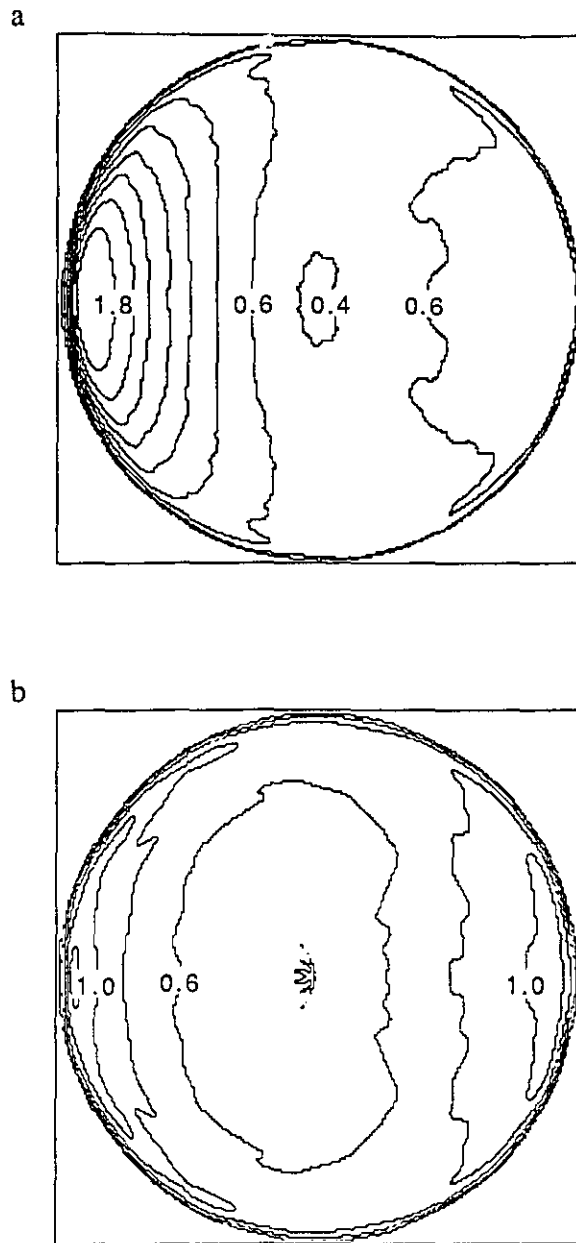


Figure 4.2.2. Angular dependence of the reflected radiation for 60° solar zenith angle: (a) plane-parallel cloud with $\tau = 7.5$ and albedo = 0.55, (b) broken cloud field with the same scene-average albedo. The values are in BRF units and the coordinates are the same as in Figure 4.2.1.

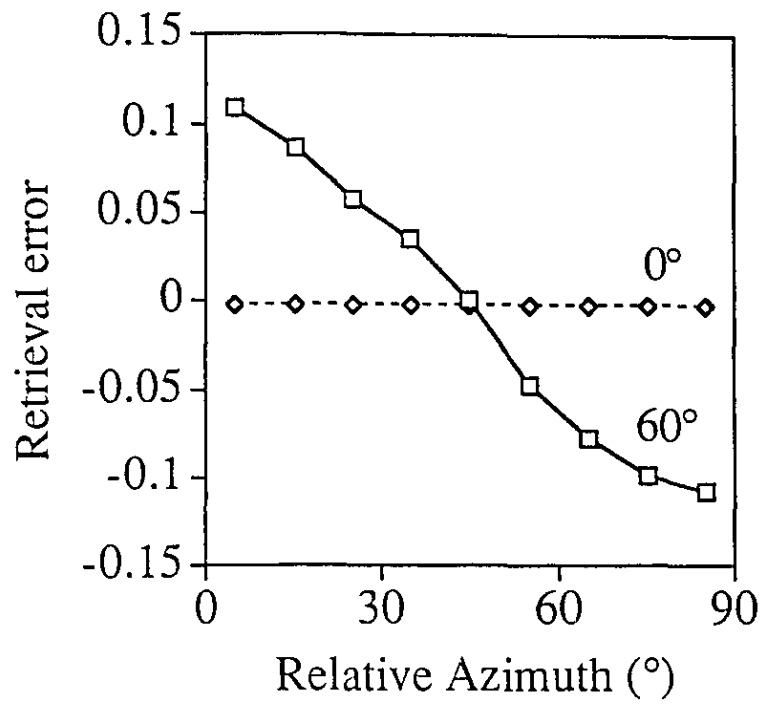


Figure 4.2.3. Azimuth-dependent bias of the energy weighting scheme for a plane-parallel cloud with $\tau = 7.5$. The solar zenith angles are 0° and 60° for the two curves, respectively.

The main danger of the other approach, the use of theoretical models, is "overmodeling," i.e., using a model which is not appropriate for a particular scene. This danger can be minimized by adopting a three-step strategy:

1. If the cloud type is known exactly, the appropriate model should be used. Due to the large variety of cloud inhomogeneities, this deterministic weighting of measured BRF values will initially be used only for homogeneous, plane-parallel clouds.
2. If the measurements do not fit any cloud model exactly, but agree with basic cloud reflection properties, a generic cloud model should be used. Such a model takes into account basic cloud properties, but is not specific to any particular cloud type. In this case, the measurements taken by separate cameras are combined using a stochastic weighting scheme described in Section 4.3.2.
3. If the measurements do not fit even basic cloud properties, the use of any cloud-specific angular model would be unjustified. Thus, the energy weighting scheme should be used.

Although the basic approach is theoretical, future MISR measurements could still be used to improve the accuracy of albedo retrieval methods. One way to incorporate future measurements into the derivation of regression coefficients is outlined in Section 4.3.1.

4.3 Azimuthal Model Database

The determination of a_k and ϵ coefficients for equation (4.2.1) involves two main steps: calculating the radiative properties of a large variety of cloud scenes, and using the results to generate the required coefficients. These steps are described in the following two subsections.

4.3.1 Cloud database

The main purpose of generating the cloud database is to obtain the radiative properties of a wide variety of cloud fields. The scenes in the database are specified by satellite retrievals and by a stochastic cloud model described in Section 2.1.2. The scenes, at 68-meter resolution, cover 35.2 x 35.2 km areas (the resolution of coarse MISR albedos), and include a large variety of

- cloud thicknesses (optical depths ranging from 1.5 to 50),
- cloud structures (including homogeneous, plane-parallel clouds and broken cloud fields with both cloud top height and VEC variations), and
- cloud microphysical properties (based on various droplet size and ice crystal distributions).

Cloud radiative properties are calculated using the Monte Carlo model described in Section 2.2.2. Presently, the database includes results for 84 cloud fields at 0.443 μm and 0.865 μm wavelengths (blue and near-infrared MISR channels). At this time, results have been generated for 0°, 30°, 60° and 80° solar zenith angles, but simulations for other solar elevations will be necessary in the future. Simulations include atmospheric effects as described in Section 2.2.2. A technique similar to the adding-doubling method ensures that the available Monte Carlo results can be used to calculate cloud reflection above any surface in a matter of seconds. For the sake of simplicity, however, all results presented in this chapter are for non-reflecting surfaces (which might be regarded as a first-order approximation for oceans). Cloud reflection is calculated at an angular resolution of 10° along the azimuth and 0.04 along the cosine of the viewing zenith angle. In order to obtain fairly high accuracies (with errors typically less than 0.01 in reflectance and 0.0003 in albedo values), each Monte Carlo experiment has simulated at least four million photons. Thus the main uncertainties of the cloud dataset are not in calculating radiative transfer, but in specifying the cloud fields in a realistic way. In particular, the main limitations, in approximate decreasing order of importance, are that

- the dataset is based largely on artificial cloud structures, and it is unknown how representative each cloud field is of real ones,
- the microphysical properties of ice crystals are poorly known and hence may not be well represented,
- the large variety of underlying surfaces is not fully represented,
- water cloud microphysics is simplified by using only a few droplet size distributions,
- the dataset is based on LOWTRAN model atmospheres which are not representative of all atmospheric conditions,
- light polarization and atmospheric refraction are neglected.

Future MISR measurements may be used to reduce the uncertainties due to the first and most important problem. Currently, there is no reliable way to tell the degree to which particular artificially generated cloud fields are representative of real cloud fields, and thus each one is given equal weight in various calculations based on the dataset. However,

these equal weights may be modified using future MISR measurements. For example, a large number of MISR measurements could each be assigned to the most similar cloud model in the dataset. Then each cloud field in the dataset would be given a weight proportional to the number of measurements assigned to it. Once these weights were calculated, the new dataset could be used to refine the albedo retrieval method. However, since no MISR measurements are presently available, the details of such possible improvements have not yet been developed.

Until MISR data become available, the use of other satellite measurements is planned to improve the representativeness of the cloud dataset. Monte Carlo simulations for a large number of cloud fields obtained from AVHRR data have just begun. The original 1.1 km resolution of the nadir AVHRR data is enhanced four-fold to 275 m by including randomly generated small-scale variations that follow the power law scaling of the original image. These small-scale variations are generated using a simple procedure based on the stochastic cloud model described in Section 2.1.2.

4.3.2 Azimuthal models

Once the cloud dataset is set up, the next task is to generate azimuthal models (AZM's), i.e., to determine the integration coefficients for equation (4.2.1). An important requirement is that the method should work even if measurements are not available from all nine MISR cameras. This can happen, for example, if a high level cloud obscures oblique views to nearby lower-level clouds. Therefore, separate sets of integration coefficients are required for each possible configuration of camera-obscurances.

As mentioned in Section 4.2, the coefficients for the energy weighting scheme method can be determined easily, based on simple geometrical considerations.⁶ After various methods were tested, a five-step algorithm proved to be the best for both plane-parallel and generic cloud models. (In order to improve retrieval accuracy, separate plane-parallel models should be used for clouds in various brightness intervals.) The approach is to use each available camera to give an individual albedo estimate, and then combine these estimates. The algorithm is as follows:

⁶If all nine cameras are available, the coefficients are: *D* cameras: 0.08, *C* cameras: 0.1, *B* cameras: 0.14, tilted *A* cameras: 0.1312, nadir *A* camera: 0.096.

Step 1.

All the relevant scenes from the cloud dataset should be used to calculate the ratio r_k :

$$r_k = \frac{\sum_{i=1}^{N_{clouds}} A_i}{\sum_{i=1}^{N_{clouds}} BRF_{ki}}, \quad k = 1, 2, \dots, 9$$

where N_{clouds} is the total number of relevant scenes in the dataset.

Step 2.

For each camera, the appropriate r_k value should be used to estimate the albedo of each cloud scene:

$$A_{i,k} = r_k BRF_{i,k}, \quad i = 1, 2, \dots, N_{clouds}, \quad k = 1, 2, \dots, 9.$$

These estimations will have a certain σ_k root mean square (RMS) error:

$$\sigma_k = \frac{1}{N_{clouds}} \left[\sum_{i=1}^{N_{clouds}} (A_{i,k} - A_{i,true})^2 \right]^{1/2}.$$

Step 3.

The nine r_k values should be weighed inversely proportionally to their individual σ_k values:

$$r'_k = r_k w_k = r_k \frac{\frac{1}{\sigma_k}}{\sum_{k=1}^9 \frac{1}{\sigma_k}}. \quad (4.3.1)$$

Step 4.

A first-order albedo estimate, A' , should be obtained:

$$A' = \sum_{k=1}^9 r'_k BRF_k.$$

This is equivalent of assuming that a_k in equation (4.2.1) equals r'_k , and ε is zero.

Step 5.

The calculation of A' in Step 4 does not take into account that cloud reflection becomes more isotropic as clouds become thicker. Thus, the estimated A' values are biased downward for thin clouds, and upward for thick clouds. The results presented in Figure 4.3.1 show that this bias can be eliminated if the A' values are corrected through a simple linear regression:

$$A^* = \gamma A' + \eta$$

Then the coefficients required for equation (4.2.1) can be obtained by simply taking $a_k = r_k \gamma$, and $\varepsilon = \eta$.

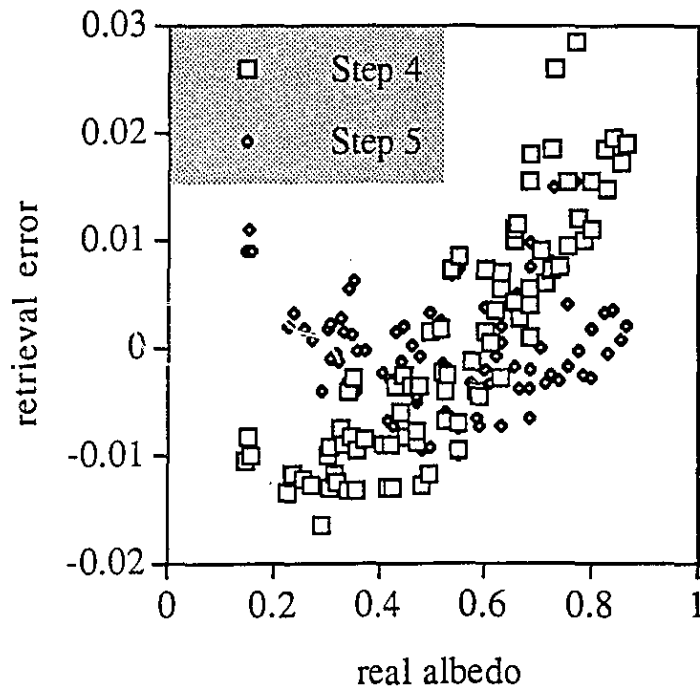


Figure 4.3.1. Albedo retrieval errors for inhomogeneous clouds. SZA = 60°, and relative azimuth = 30°.

4.4 Choosing an Azimuthal Model for Observed Scenes

Once the azimuthal database (containing regression coefficients for equation (4.2.1)) is set up, the main task of angular integration is to choose which azimuthal model should be used for a particular measurement. The following procedure can be used to choose the index numbers which identify the most appropriate azimuthal model:

- Select the relevant solar elevation- and view angle index numbers.
- For retrievals at 0.443 and 0.555 μm , select the appropriate index number for the RLRA. The index number is important for taking into account the magnitude of Rayleigh scattering that occurs above the main reflecting layer.
- Select an index number according to the configuration of oblique camera views that are obscured.
- Based on the geographical location, time of year and other sources (for example, the SSM/I global snow-ice coverage map), choose the appropriate surface scene type (for example, ocean, vegetated land, non-vegetated land, and snow or ice).
- Use the nadir cloud mask to decide whether a cloud or a surface azimuthal model should be used. For cloudy scenes, carry out the following steps:
 1. Based on geographical location, time of year, and RLRA, guess the cloud phase (ice, liquid or unknown). Though the "unknown" category will probably be chosen very often, fairly safe guesses can be made for many cases (low-level equatorial clouds, polar clouds, etc.).^{7,8}
 2. Decide whether or not a homogeneous, plane-parallel cloud model can be applied. For the decision, consider
 - i*) whether small-scale variations of nadir reflectance, as given by the standard deviation of all 275 x 275 m areas within a 2.2 km pixel (a standard MISR product), exceed a certain threshold value.
 - ii*) whether larger-scale variations of nadir reflectance, as determined from the standard deviation of a 5 x 5 array of 2.2 km pixels, exceed a certain threshold.
 - iii*) whether camera-to-camera changes in the measurements agree with plane-parallel cloud reflection models. If the RMS difference between

⁷In later phases of the MISR mission, these guesses can be improved by using a standard product of the MODIS instrument (also on board the EOS-AM satellite), which describes cloud phase. However, this product cannot be used in MISR retrievals until approximately a year after the launch, when the MODIS science team evaluates its reliability.

⁸The use of current meteorological temperature data is also considered for estimating the cloud phase.

the measurements and the best-fitting plane-parallel model is large, the homogeneous model cannot be used.

3. If a plane-parallel model can be applied, choose the model with the smallest RMS difference from the measurements (as determined in Step 2iii).
4. If a plane-parallel model cannot be applied, decide whether a generic cloud model can be used. This choice should be based on whether or not the measured BRF values are consistent with general cloud reflection properties. Unexpected features would indicate that the scene cannot be represented by a generic cloud model, and thus the energy weighting scheme must be used. Specifically, the following questions should be considered:
 - Is any camera's BRF value very different from the average of its neighboring cameras' values? (i.e., Do the camera-by-camera variations follow a relatively smooth curve?)
 - Are the nadir to most oblique camera variations within reasonable bounds? These bounds are defined as the smallest and largest changes in the relevant portion of the cloud dataset.

In some cases the reflection from a 2.2 x 2.2 km area may appear irregular only because the pixel contains a small portion of a cloud. For example, reflections to the right and left are markedly different if only an area at the right edge of a cloud is considered. In this case, a lot of radiation can escape through the cloud side to the right, whereas only reflection from the cloud top goes to the left. If the energy weighting scheme were applied to such pixels, the average of retrieved albedos over entire broken cloud fields (i.e., the coarse albedos) could have biases similar to the effect shown on Figure 4.2.3. (The biases would be somewhat weaker than on Figure 4.2.3, since, as Figure 4.2.2 demonstrates, the reflection of broken cloud fields tends to be less azimuthally anisotropic than the reflection of plane-parallel clouds.) Therefore, in deciding whether the generic cloud model can be used, Step 4 does not consider individual pixels, but rather, the average reflection of 5 x 5 pixel areas around them. This way the energy weighting scheme is chosen only if the reflection of this area (which contains more entire clouds) behaves irregularly.

Once this procedure is completed, the index numbers obtained identify the a_k and ϵ values that can be used in equation (4.2.1) to estimate the albedo.

4.5 Uncertainty Estimations

Since no measurements similar to MISR are available, the uncertainties of the albedo-retrieval method can be estimated only from the present cloud dataset. However, since this dataset is largely made up of artificially generated cloud fields, uncertainty estimates should only be considered as guides, not as quantitatively reliable values. It is nonetheless worthwhile to make estimates to test whether the retrieval algorithms behave reasonably, and to demonstrate the potential benefits of using multiple views for albedo retrievals. These two tasks are addressed in the sections below by using the azimuthal models derived from the cloud dataset to retrieve albedos for various scenes in the dataset.

The error estimates are presented for the 0.865 μm MISR channel. Over ocean, the most important difference between the four channels is in the magnitude of Rayleigh scattering. The main effect of this scattering is to smooth out the differences among the angular distributions of radiation reflected by various cloud types, thus making albedo retrievals slightly easier. Therefore, MISR cloud albedo retrievals are expected to be most accurate for the 0.443 μm and least accurate for the 0.865 μm channel. The difference between retrieval accuracies at these two wavelengths is demonstrated at the end of Section 4.5.2.

4.5.1 Testing the behavior of retrieval algorithms

The logic of plane-parallel and generic cloud albedo retrieval methods ensures that they are free from an overall bias. That is, given a perfect cloud database, they can correctly determine the global average albedo of their respective scenes. The lack of overall bias does not, however, necessarily imply that they could not have systematic biases for various cloud types. For example, such a bias could be a systematic over- and underestimation of albedo values according to various cloud droplet size distributions. Such a bias would mean, for example, that the albedos obtained for fogs (made up of very small droplets) would all be biased upward or downward. The average errors for various droplet size distributions, shown on Figure 4.5.1, however, indicate that this is not the case: neither plane-parallel nor generic cloud retrievals lead to significant droplet-size-dependent biases.⁹

⁹Since only two ice phase functions are presently available, and it is not clear how representative they are of real ice clouds, the effects of cloud phase cannot yet be estimated in a reliable way. Therefore, the problem of ice clouds should be addressed in future studies.

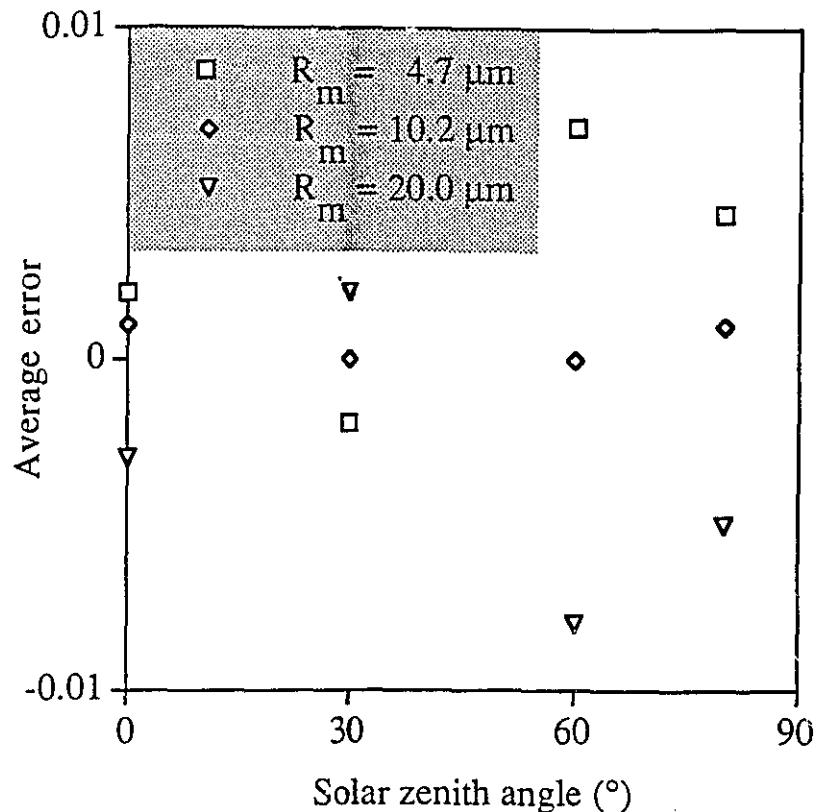


Figure 4.5.1. Average albedo retrieval errors for plane-parallel clouds having modified gamma droptime distributions with various modal radii. MISR's relative azimuth is 60° for $\text{SZA} = 30^\circ$, and 30° for $\text{SZA} = 60^\circ$ and 80° . These azimuth values are representative of the orbit of the EOS-AM satellite and are used in subsequent figures as well.

Another bias in generic cloud retrievals could be over- or underestimation of cloud albedos, depending on whether a scene was nearly plane-parallel or very inhomogeneous. The possibility of such a bias is examined by using coefficients from generic cloud models to estimate the albedos of plane-parallel clouds. It is expected that if the albedo values for plane-parallel clouds are biased either way, albedos for very broken cloud scenes must be biased in the opposite direction in order to allow the overall average to remain correct. The results shown on Figure 4.5.2 suggest this bias to be fairly small, and certainly much smaller than it would be for single-view instruments.

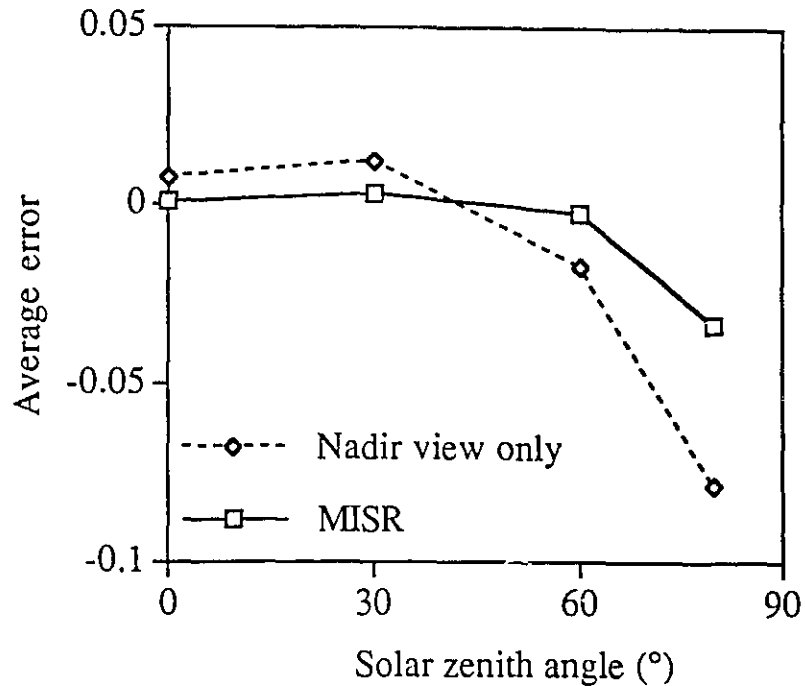


Figure 4.5.2. Average error if the albedo of plane-parallel clouds is retrieved using generic cloud models.

4.5.2 Benefits of using multiple views

Multiple views can improve retrieval accuracies in two ways. First, knowledge of the angular variation of reflected radiation helps decide whether or not plane-parallel or generic cloud models can be used, and thereby prevents the use of inappropriate models in certain cases (Figure 4.5.3). Second, multiple views also decrease errors once the appropriate retrieval method is selected. To examine this effect, the RMS errors of albedo estimations based on all nine views are compared to errors that would occur if the nadir view alone were available.¹⁰ For plane-parallel clouds, the accuracy of angular integration cannot improve significantly, since for such scenes even nadir-only

¹⁰The maximum encountered errors are not examined, since it is doubtful that all scenes in the cloud dataset are realistic. (A single unrealistic cloud could increase the maximum error significantly, while it could affect the RMS error to a much smaller degree.)

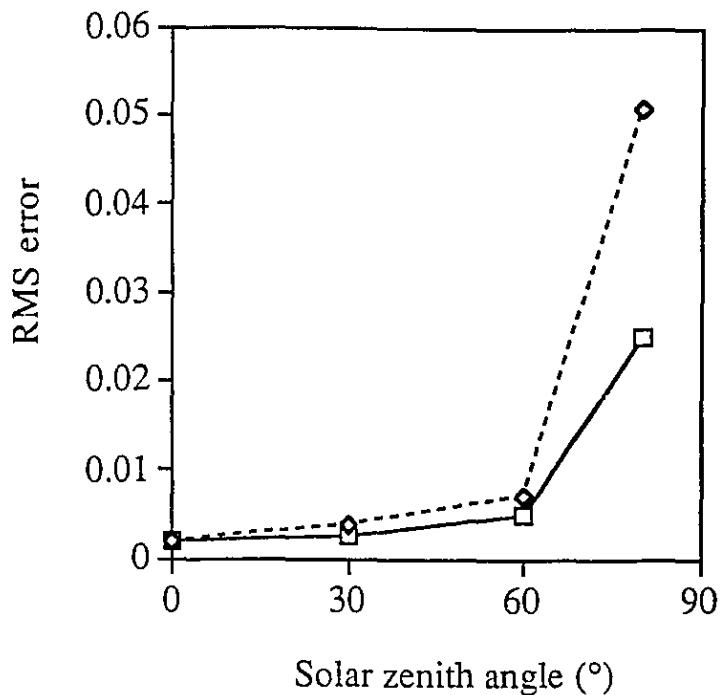


Figure 4.5.3. RMS error of estimates for inhomogeneous cloud albedos obtained using various cloud models and all nine cameras. The dashed line indicates results if plane-parallel models are used for the retrievals; the solid line, if the generic cloud model is used.

measurements can give accurate results (for water clouds with RMS errors less than 0.005). Hence, for homogeneous scenes, multiple views can decrease albedo retrieval errors mainly by reducing calibration errors and random noise in the measurements. For inhomogeneous clouds, however, multiple views can improve the accuracy of angular integration significantly (Figure 4.5.4). This result is very important, since it indicates that MISR will be able to achieve one of its main goals, to improve the accuracy of albedo retrievals for inhomogeneous clouds. The figure also shows that the improvement is greatest for oblique sun cases—exactly where single-view retrievals are least accurate.

The question may arise, which additional views make this improvement possible. One way to address this question is to look at the weights assigned to each camera, i.e., the w_k values in equation (4.3.1). Figure 4.5.5 shows that the *B* cameras have the highest

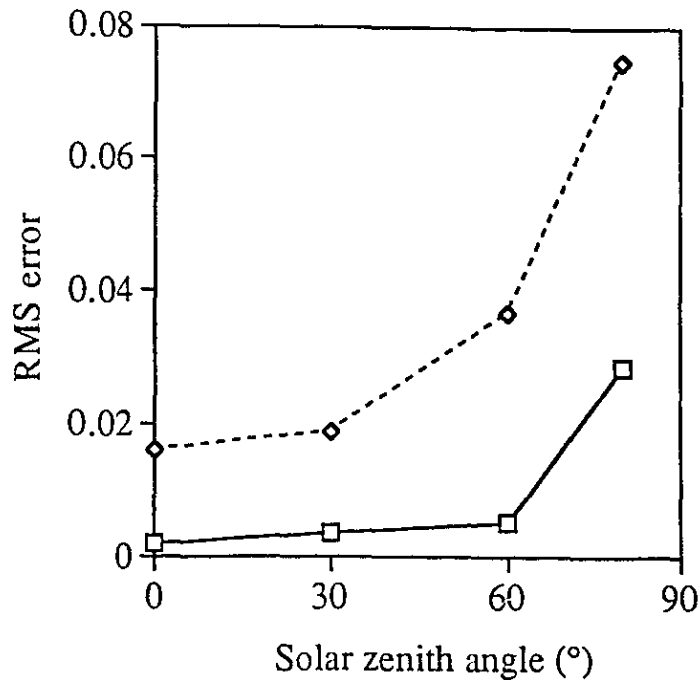


Figure 4.5.4. RMS error of stochastic albedo retrievals using a single nadir view (dashed line) and nine views (solid line). Since the results are obtained for 35.2 x 35.2 km areas, they represent the accuracy of coarse albedos.

weights and thus contribute most to the final albedo estimates. This implies that on the orbit of EOS-AM satellites, viewing zenith angles close to 45° are optimal for single-view albedo estimations. This is somewhat smaller than the 60° angle Davies (1984) found to be most suitable. The difference is probably due to the fact that Davies modeled inhomogeneous clouds as cubes with equal horizontal and vertical dimensions, whereas the present cloud dataset contains more complex cloud structures.

Another way to look at how each camera affects final retrieval accuracy is to examine how errors change as more and more oblique cameras are obscured. Figure 4.5.6 indicates that even if only the *A* and *B* cameras can be used, the accuracy is still significantly higher than that of nadir-only instruments.

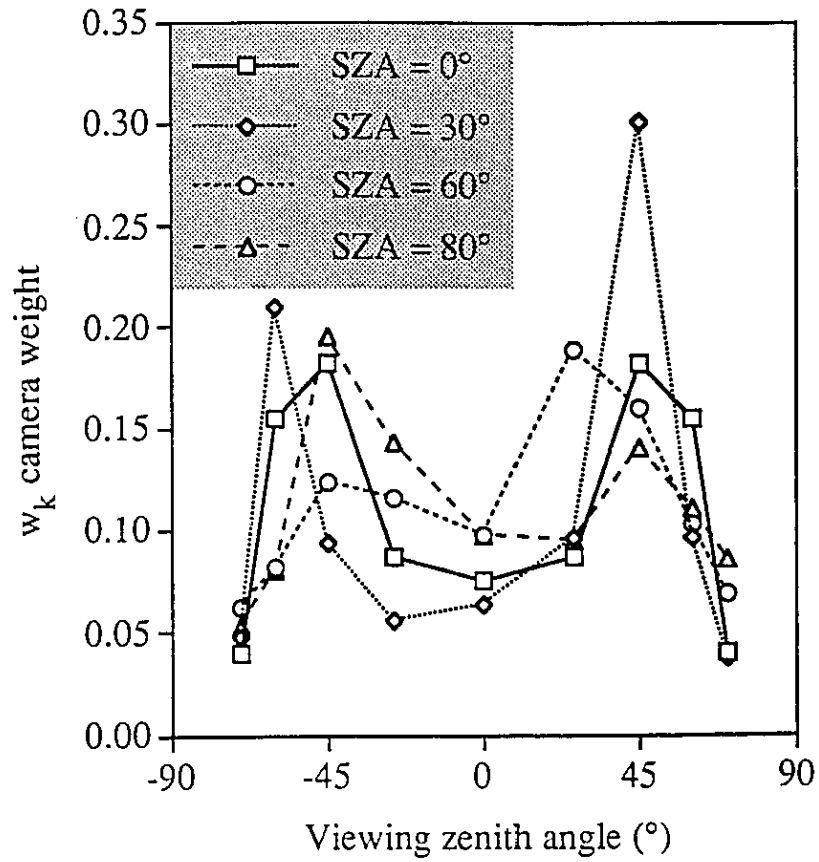


Figure 4.5.5. The w_k camera weights for various solar zenith angles as a function of the camera viewing zenith angle. Negative viewing zenith angles indicate forward scattering directions; positive ones, backscatter.

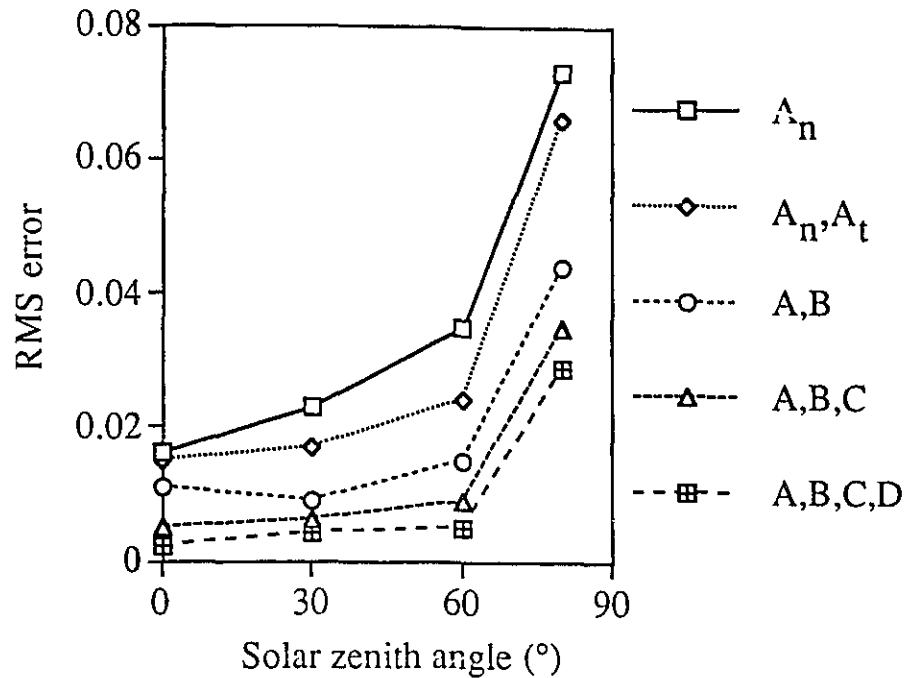


Figure 4.5.6. RMS errors if oblique cameras are obscured. Each line corresponds to a set of available cameras.

Since Figure 4.5.4 presents error estimates obtained at 35.2 km resolution, its values refer to coarse albedos. As mentioned in Section 4.4, the accuracy of MISR's fine albedos can be affected by some 2.2 km pixels containing only portions of inhomogeneous clouds. In order to demonstrate this effect, the reflection of a 35.2 x 35.2 km broken cloud field ($\langle \tau \rangle = 15$; $CF = 0.5$; $\beta = 30 \text{ km}^{-1}$; $s_{(k)} = 1$, if $k \leq 6$, otherwise $s_{(k)} = 3.6$) is simulated at 2.2 km resolution. For 60° solar zenith angle, the results indicate that while the generic cloud model can determine the overall scene albedo with an error of only 0.017, the RMS error for the individual pixels is 0.047. This indicates that MISR's fine albedo values have larger uncertainties than coarse albedos. Since using a single nadir view for the same scene would give a fine albedo uncertainty of 0.134, though, MISR's multiple views can still be expected to improve the accuracy of fine albedos.

Uncertainties associated with the energy weighting scheme are much more difficult to evaluate than errors in plane-parallel and generic cloud retrievals. The reason for this is

that the cloud database cannot be used to test the scheme, since the scheme is supposed to be applied specifically for cases that are inconsistent with the database. Until actual measurements can be studied, one can only assume that multiple views will improve the retrieval accuracy even for the energy weighting scheme.

So far, all estimates for the retrieval uncertainty have been presented for the 0.865 μm MISR channel. As mentioned above, over ocean, the most important difference between the four channels is in the magnitude of Rayleigh scattering. The main effect of this scattering is to smooth out the differences among angular distributions of radiation reflected by various cloud types, thus making albedo retrievals a little easier. Since the magnitude of Rayleigh scattering decreases with increasing cloud height, this effect can be expected to be strongest for low-level clouds, and weakest for high-level clouds. It can also be expected to increase with SZA, since Rayleigh scattering becomes stronger as photons travel along more tilted, and hence longer paths in the atmosphere. The magnitude of this effect is examined by comparing the accuracy of albedo retrievals at a wavelength with strong Rayleigh scattering (0.443 μm) to the accuracy at a wavelength with negligible Rayleigh effect (0.865 μm), assuming a cloud-base height of 2 km for all scenes. The results presented in Figure 4.5.7 suggest that (provided that the RLRA is known precisely) for low- and mid-level clouds, MISR albedos can be expected to be most accurate for the blue channel (0.443 μm).

Over land, the retrieval accuracy at various wavelengths depends on how precisely the surface characteristics are known. The problems of retrieving surface radiative properties, however, lie beyond the scope of the present work, and are therefore deferred to further studies.¹¹

¹¹Surface albedo retrieval methods are being developed by Chris Borel and Sig Gerstl at the Los Alamos National Laboratory.

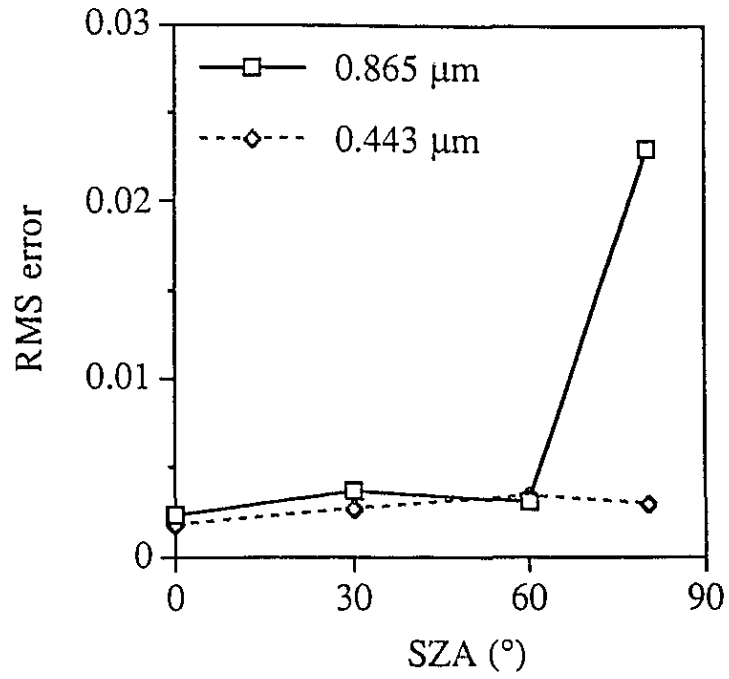


Figure 4.5.7 RMS error of stochastic albedo retrievals at 0.443 μm and 0.865 μm wavelengths.

Chapter 5

Conclusions

This study has focused on the shortwave radiative effects of cloud inhomogeneities. In particular, it has addressed two main questions: what the processes through which inhomogeneities influence solar reflection are, and how this influence can be taken into account in albedo retrievals based on future satellite measurements.

Addressing the first question was important, since while previous studies calculated the radiative effect of various cloud inhomogeneities, they did not fully explain these effects. These studies offered explanations for the calculated inhomogeneity effects using various terms and expressions, such as "channeling," "plane-parallel albedo bias," and "side illumination." However, these terms did not give full descriptions of the mechanisms through which cloud inhomogeneities influence solar radiation. As a result, there was no way to tell the degree to which various mechanisms were responsible for the overall inhomogeneity effect. Specifically, the main problems were that

- Most terms were used only in a qualitative sense, without exact definitions. Thus the magnitudes of various effects could not be quantified.
- Many definitions were appropriate only for special cloud geometries. For example, the term "side illumination" could be interpreted easily for cuboidal or cylindrical clouds, but it is not so obvious exactly where the sides of a cumulus cloud end and the top begins.
- The various terms described only some individual aspects of radiative transfer in inhomogeneous clouds, but they did not form coherent systems that would explain the overall effects of cloud inhomogeneities. For example, the plane-parallel albedo bias addressed the fact that the cloud layer which solar radiation reaches has areas where clouds are thicker and thinner than average. However, there were no corresponding definitions for the effects that complement this bias by influencing radiation once it is within the cloud layer.

This study has proposed a way to overcome these problems by taking a new approach: instead of examining how inhomogeneities change radiance and flux values at various fixed locations, as other studies did, it has studied how individual photons are influenced by inhomogeneities as they move along their paths within the cloud layer. The difference between the present approach and other ones is analogous to the difference between the Lagrangian and Eulerian approaches used, for example, in fluid dynamics.

Using the adopted approach, this study established a theoretical framework which defines and evaluates the various mechanisms through which cloud inhomogeneities influence solar radiation. The main advantages of the proposed framework are that

- It reflects the physical processes through which cloud inhomogeneities influence shortwave radiation.
- It is based on unambiguous, quantitative definitions that are easy to calculate.
- Its individual inhomogeneity effects complement each other without overlap; i.e., they can simply be added up to obtain the overall inhomogeneity effect.
- It can be used for any irregular cloud fields. Any inhomogeneities—for example, internal volume extinction coefficient variations and the effects of cloud brokenness—can be handled within a unified framework.

The proposed system separates the radiative effect of cloud inhomogeneities into two main components: 1-D and 3-D inhomogeneity effects. The 1-D effect addresses the fact that photons enter the cloud layer at locations of various optical thicknesses, whereas the 3-D effect, that these photons may actually encounter more or fewer droplets than their point of entry would suggest, because multiple scattering changes their course. In order to calculate the magnitude of the first component, the study has developed a one-dimensional radiative transfer approximation called the “Tilted Independent Pixel Approximation” (TIPA). This approximation, somewhat related to the widely used “Independent Pixel Approximation” (IPA), can not only calculate the 1-D inhomogeneity effect, but could also be used in future studies to obtain quick estimates of scene albedo. An important advantage of the TIPA is that, unlike the IPA, it uses not only the frequency distribution, but also the spatial distribution of cloud optical thicknesses. This allows the TIPA to explain various phenomena that cannot be explained using the IPA, for example, that cloud streets parallel and perpendicular to the sun have different radiative properties. However, results also indicate that even if the TIPA is used, a 1-D framework is not sufficient to fully describe numerous phenomena, since 3-D effects are often also very important. This study identified four 3-D mechanisms through which cloud

inhomogeneities influence solar radiation: upward trapping, downward trapping, upward escaping, and downward escaping. The magnitude of these four components of the 3-D inhomogeneity effect was calculated from Monte Carlo simulations.

Uses of the proposed framework were demonstrated by quantitatively examining various aspects of the inhomogeneity effects that occur in irregular cloud fields. It was found that identical variations in cloud optical thickness can cause much stronger inhomogeneity effects if they are due to variations in cloud top height (CTH) (i.e., geometrical cloud thickness), and not in volume extinction coefficient (VEC), as assumed in previous studies of irregular cloud fields. For overhead sun, the differences in albedo are comparable in magnitude to the 3-D effects themselves, and can exceed 0.05. For oblique sun, the differences are smaller, but can still be significant.

The differences were explained by examining why the individual components of the overall inhomogeneity effect are different for the two types of cloud variability. It was found that for VEC variations, downward escaping is the strongest 3-D effect, whereas in the case of CTH variations, the other three 3-D effects can be at least as important. Combining the individual 3-D effects revealed that, as suggested in previous studies, the main means by which 3-D effects decrease the albedo of clouds with VEC variations is the flow of radiation from thick to thin regions. In case of CTH variations, however, the main means is the flow of radiation from thin to thick regions. It was also found that for oblique sun, 3-D effects decrease the scene albedo primarily by making the reflection of upwelling radiation more difficult. This finding was somewhat unexpected since previous studies focused more on 3-D effects decreasing the scene albedo by making the transmission of downwelling radiation easier.

As expected, 3-D effects were found to decrease the albedo of all scenes having VEC variations. However, it was found that for overhead sun, 3-D effects due to CTH variations can increase the albedo even if neither absorption, nor surface reflection is present. The increase (which was less than 0.01 for all cases) can occur for scenes with slightly sloped cloud sides and large cloud fraction, and is due to a relatively strong upward escaping effect. Although 3-D effects still decreased the albedo of most scenes with CTH variations, the above result implies that the IPA underestimates the albedo of some inhomogeneous cloud scenes even for overhead sun.

It was also found that the addition of an underlying homogeneous, plane-parallel cloud layer can enhance 3-D inhomogeneity effects due to CTH variations. For turreted stratus geometries the enhancement is due to an increase in the upward trapping effect and can exceed 0.06. The results suggest that 3-D effects due to small CTH variations decrease cloud reflection most at the cloud edge, whereas 3-D effects due to large CTH variations decrease cloud reflection most at intermediate cloud thicknesses. One should note, however, that the addition of a plane-parallel layer always decreases the 1-D inhomogeneity effect, and hence the overall inhomogeneity effect as well.

After examining the effects on albedo, this study also investigated how inhomogeneities affect cloud reflection toward the zenith, a direction which is especially important for satellite remote sensing. (Many studies have used near-vertical satellite measurements because they have higher spatial resolution than oblique measurements. Another advantage of near-vertical views is that vertically extended clouds do not obscure the gaps that occur between them, as they do in oblique measurements.) In particular, the proposed theoretical framework was used to offer a possible explanation of why clouds reflect a relatively larger portion of the incoming solar radiation toward the zenith for oblique than for overhead sun (Loeb and Davies 1996). While this phenomenon appears to contradict the behavior of homogeneous clouds, it can apparently be explained by the effect of cloud inhomogeneities, especially CTH variations. It was shown that the zenith reflectance of inhomogeneous clouds increases with the solar zenith angle mainly because inhomogeneities tend to make it more difficult for radiation to leave the cloud in oblique forward directions. The results indicate that the relative difference between the scene average nadir reflectance of cloud fields with CTH and VEC variations can exceed 25% for overhead sun, and 50% for oblique sun.

The results discussed above imply that the radiative properties of many cumulus cloud fields (which have significant CTH variations) may be somewhat different from those suggested in previous studies. (These studies either used simple cloud geometries, such as cubes, or attributed all optical thickness variations to changes in the VEC, and kept the geometrical cloud thickness constant.)

This study described various processes and phenomena that occur in some irregular cloud fields. Its most important limitation seems to be the uncertainty in how representative the examined cloud structures are of real clouds (e.g., which examined situation occurs how

often, etc.). Thus, future studies based on more representative cloud datasets are required to determine the magnitude of the described effects in the earth's atmosphere.

In future studies, the proposed theoretical framework can also be used to investigate various aspects of shortwave radiative inhomogeneity effects not addressed here. For example, it can be useful in exploring the influence of stochastic vertical inhomogeneities and of 3-D variations in microphysical cloud properties, or in examining the effects of cloud inhomogeneities on the angular and spatial distributions of reflected radiation, and on solar absorption and transmission. The developed definitions and approach of examining how each individual photon is affected by cloud inhomogeneities can also be useful in studying radiative processes that occur in inhomogeneous media other than clouds, such as turbid fluids.

This study also developed an algorithm that, by taking advantage of the unique multi-view capability of the future MISR instrument, can improve the accuracy of satellite estimates of inhomogeneous cloud albedos. This task is important, since present albedo retrieval methods (based on single-view measurements) treat homogeneous and inhomogeneous scenes the same way, thereby, as shown in previous studies, introducing large biases in estimated albedo values. The potential accuracy of the developed algorithm was analyzed for a dataset obtained by using a Monte Carlo model to simulate radiative transfer through a large number of irregular cloud fields. The results indicate that using multi-view measurements can improve the accuracy of satellite-based albedo retrievals by a factor of three or more. The improvements can be attributed to two main factors. First, knowledge of the angular variation of reflected radiation helps decide whether plane-parallel or generic cloud models can be used, and thereby prevents the use of inappropriate models in certain cases. Second, multiple views decrease errors once the appropriate cloud model is selected by making the task of angular integration easier.

The most important task required to improve the accuracy of the developed method is the improvement of the cloud dataset used in generating look-up table values. Such improvements can be achieved by processing future MISR measurements. Since such data are not yet available, more AVHRR scenes will soon be used to make the dataset more

representative of real cloud fields. The present dataset should also be extended to include ice clouds and various land surfaces.

Although the algorithm was developed specifically for the MISR instrument, it can be adapted for albedo retrievals based on other multi-view instruments or on co-located measurements taken from different satellite platforms (for example, a geostationary and a polar orbiter platform).

Finally, the algorithm, which presently calculates albedos for specific wavelengths, can be further developed to estimate broad-band shortwave albedos. These climatologically important albedos could be obtained by combining MISR data with measurements taken by other instruments on the same platform (for example MODIS and CERES). Such algorithms could take advantage of the unique opportunity posed by the fact that, for the first time, the EOS-AM satellite will provide simultaneous information about the spatial, spectral and angular distributions of the solar radiation reflected from clouds.

Appendix A

Algorithms for Albedo Calculations using the Tilted Independent Pixel Approximation

In this study, the values of $\langle A_{\{\tau_{(x,y)}^*\}} \rangle$ in equation (3.1.2) are calculated using a slightly modified version of the Monte Carlo radiative transfer model described in Section 2.2.2. Only the following three modifications are required to enable the model to perform calculations based on the TIPA:

- In order to ensure that all photons move along straight lines, the first free pathlength L of each photon (measured in optical thickness units) is set to an extremely large value. This ensures that all photons pass through the cloud layer without being scattered.
- After each photon is simulated, a τ^* value is obtained by multiplying the optical pathlength l the photon actually passed through by the cosine of the SZA. Then the $A_{\{\tau^*\}}$ plane-parallel albedo is obtained from a pre-calculated look-up table.
- The scene-average TIPA albedo $\langle A_{\{\tau_{(x,y)}^*\}} \rangle$ is then estimated by averaging the $A_{\{\tau^*\}}$ values of all simulated photons.

The statistical uncertainty of the obtained TIPA albedos can be estimated the same way as the uncertainty of any Monte Carlo albedos, with equation (2.2.4). An important advantage of this Monte Carlo approach is that the effects of diffuse illumination (due, for example, to Rayleigh scattering by the overlying air) can be included through a very simple modification: scattering in the overlying air should be allowed by setting the photon pathlength L to a large value only once a photon enters the cloud layer.

Another possible approach is to calculate the full distribution of $\tau_{(x,y)}^*$ over an entire scene. The knowledge of all $\tau_{(x,y)}^*$ values can be useful, for example, in studying the effects of cloud inhomogeneities on the spatial distribution of reflected radiation. For scenes with horizontal variations in the volume extinction coefficient, $\tau_{(x,y)}^*$ can be obtained by using the equation

$$\tau_{(x_0, y_0)}^* = \sum_{x=x_0}^{x_0 - z_0 \tan(\theta_0)} \frac{\beta(x, y_0, z_0 - (x_0 - x) \tan(\theta_0)) \Delta x}{\tan(\theta_0)},$$

where Δx is the horizontal resolution of the scene and Θ_0 is the SZA. For internally homogeneous clouds with cloud top height variations, the τ^* values for full lines in x direction can be obtained using

$$\tau_{(x_0, y_0)}^* = \sum_{x=z_0 \tan(\theta_0)}^X \sum_{x^*=x-z_0 \tan(\theta_0)}^{x-(z_0 - z_{top}(x, y)) \tan(\theta_0)} \frac{\beta \Delta x}{\tan(\theta_0)}, \quad \left[0 < x_0 < X - z_0 \tan(\theta_0) \right],$$

where $z_{top}(x, y)$ is the cloud top height at point (x, y) and X is the domain size in the x direction. Since both equations require high spatial resolutions for accurate results, this second approach can be most efficient for smaller scenes (for example based on Landsat-TM images). For larger scenes (for example, those based on AVHRR or GOES images), the modified Monte Carlo approach tends to be more efficient.

References

- Aida, M., 1977: Reflection of Solar Radiation from an Array of Cumuli. *J. Meteor. Soc. Japan*, **55**, 174-181.
- Alberta, T.L., and S.K. Cox, 1990: Cloud Field Reflectance Variations Traceable to Finite Cloud Effects. *J. Appl. Meteor.*, **29**, 165-178.
- Arking, A., 1991: The Radiative Effects of Clouds and their Impact on Climate. *Bull Amer. Meteor. Soc.*, **72**, 795-813.
- Asrar, G., and D.J. Dokken, 1993: *EOS Reference Handbook*. NASA, NP-202, Washington, DC, 145 pp.
- Atlas, D., S.Y. Matrosov, A.J. Heymsfield, M-D. Chou, and D.B. Wolff, 1995: Radar and Radiation Properties of Ice Clouds. *J. Appl. Meteor.*, **34**, 2329-2345.
- Barker, H.W., 1992: Solar Radiative Transfer through Clouds Possessing Isotropic Variable Extinction Coefficient. *Quart. J. Roy. Meteor. Soc.*, **118**, 1145-1162.
- Barker, H.W., 1994: Solar Radiative Transfer for Wind-Sheared Cumulus Cloud Fields. *J. Atmos. Sci.*, **51**, 1141-1156.
- Barker, H.W., 1996a: A Parameterization for Computing Grid-Averaged Solar Fluxes for Inhomogeneous Marine Boundary Layer Clouds. Part I: Methodology and Homogeneous Biases. submitted to *J. Atmos. Sci.*
- Barker, H.W., 1996b: Estimating Cloud Field Albedo Using One-Dimensional Series of Optical Depth. submitted to *J. Atmos. Sci.*
- Barker, H.W., and D. Liu, 1995: Inferring Optical Depth of Broken Clouds from Landsat Data. *J. Climate*, **8**, 2620-2630.
- Barker, H.W., and J.A. Davies, 1992a: Solar Radiative Fluxes for Stochastic, Scale-invariant Broken Cloud Fields. *J. Atmos. Sci.*, **49**, 1115-1126.
- Barker, H.W., and J.A. Davies, 1992b: Cumulus Cloud Radiative Properties and the Characteristic of Satellite Radiance Wavenumber Spectra. *Remote. Sens. Environ.*, **42**, 51-64.
- Boers, R., and R.M. Mitchell, 1994: Absorption Feedback in Stratocumulus Clouds. Influence on Cloud Top Albedo. *Tellus*, **46A**, 229-241.
- Bohren, C.F., and D.R. Hufmann, 1983: *Absorption and Scattering of Light by Small Particles*. John Wiley & Sons Inc., New York, 530 pp.

- Bréon, F.-M., 1992: Reflectance of Broken Cloud Fields: Simulation and Parameterization. *J. Atmos. Sci.*, **49**, 1221-1232.
- Browning, K.A., 1994: Survey of Perceived Priority Issues in the Parameterization of Cloud-Related Processes in GCM-s. *Quart. J. Roy. Meteor. Soc.*, **120**, 483-488.
- Busygin, V.P., N.A. Yevstratov, and Ye.M. Feygelson, 1973: Optical properties of Cumulus Clouds, and Radiant Fluxes for Cumulus Cloud Cover. *Izv. Acad. Sci. USSR, Atmos. & Oceanic Phys.*, **9**, 648-653.
- Busygin, V.P., N.A. Yevstratov, and Ye.M. Feygelson, 1977: Calculation of the Direct, Scattered and Total Solar Radiant Fluxes and their Distributions in Cumulus Clouds. *Izv. Acad. Sci. USSR, Atmos. & Oceanic Phys.*, **13**, 184-190.
- Cahalan, R.F., 1989: Overview of Fractal Clouds. *Remote Sensing Retrieval Methods*, H.E. Fleming and J.S. Theon Ed., Deepak Publishing.
- Cahalan, R.F., and Snider, J.B., 1989: Marine Stratocumulus Structure. *Remote Sens. Environ.*, **28**, 95-107.
- Cahalan, R.F., W. Ridgway, W.J. Wiscombe, T.L. Bell, and J.B. Snider, 1994a: The Albedo of Fractal Stratocumulus Clouds. *J. Atmos. Sci.*, **51**, 2434-2455.
- Cahalan, R.F., W. Ridgway, W. Wiscombe, S. Gollmer, and Harshvardhan, 1994b: Independent Pixel and Monte Carlo Estimates of Stratocumulus Albedo. *J. Atmos. Sci.*, **51**, 3776-3790.
- Cahalan, R.F., D. Silberstein, and J.B. Snider, 1995: Liquid Water Path and Plane-Parallel Albedo Bias During ASTEX. *J. Atmos. Sci.*, **52**, 3002-3012.
- Cannon, J.C., 1970: Line Transfer in Two Dimensions. *Astrophys. J.*, **161**, 255-264.
- Carter, L.L., and E.D. Cashwell, 1975: *Particle-Transport Simulation with the Monte Carlo Method*. ERDA Critical Review Series, U.S. Energy Research and Development Administration, TID-26607, Springfield, Va, 115 pp.
- Cess, R.D. et al., 1990: Intercomparison and Interpretation of Climate Feedback Processes in 19 AGCM-s. *J. Geophys. Res.*, **95 D**, 601-615.
- Chandrasekhar, S., 1960: *Radiative Transfer*. Dover Publications, New York, 393 pp.
- Chou, M.D., A. Arking, J. Otterman, and W.L. Ridgway, 1995: The Effect of Clouds on Atmospheric Absorption of Solar Radiation. *Geophys. Res. Lett.*, **22**, 1885-1888.
- Chylek, P. and J.S. Dobbie, 1995: Radiative Properties of Finite Inhomogeneous Cirrus Clouds: Monte Carlo Simulations. *J. Atmos. Sci.*, **52**, 3512-3522.
- Coakley, J.A. Jr., and R. Davies, 1986: The Effect of Cloud Sides on Reflected Solar Radiation as Deduced from Satellite Observations. *J. Atmos. Sci.*, **43**, 1025-1035.
- Coakley, J.A. Jr., and T. Kobayashi, 1989: Broken Cloud Biases in Albedo and Surface Insolation Derived from Satellite Imagery Data. *J. Climate*, **2**, 721-730.

- Davies, R., 1976: *The Three-Dimensional Transfer of Solar Radiation in Clouds*. Ph.D. Thesis, University of Wisconsin-Madison, 220 pp.
- Davies, R., 1978: The Effect of Finite Geometry on the Three-Dimensional Transfer of Solar Irradiance In clouds. *J. Atmos. Sci.*, **35**, 1712-1725.
- Davies, R., 1984: Reflected Solar Radiances From Broken Cloud Scenes and the Interpretation of Scanner Measurements. *J. Geophys. Res.*, **89**, 1259-1266.
- Davies, R., 1994: Spatial Autocorrelation of Radiation Measured by the Earth Radiation Budget Experiment: Scene Inhomogeneity and Reciprocity Violation. *J. Geophys. Res.*, **99**, 20879-20887.
- Davies, R., W.L. Ridgway, and K.-E. Kim, 1984: Spectral Absorption of Solar Radiation in Cloudy Atmospheres: A 20cm-1 Model. *J. Atmos. Sci.*, **41**, 2126-2137.
- Davis, A., 1992: *Radiation Transport in Scale Invariant Media*. Ph.D thesis, McGill University, Montreal, 325 pp.
- Davis, A., P. Gabriel, S. Lovejoy, D. Schertzer, and G.L. Austin, 1990: Discrete Angle Radiative Transfer - Part III: Numerical Results and Applications. *J. Geophys. Res.*, **95**, 11729-11742
- Davis, J.M., and S.K. Cox, 1986: Additional Confirmation of the Validity of Laboratory Simulation of Cloud Radiances. *J. Climate Appl. Meteor.*, **25**, 398-400.
- Davis, J.M., S.K. Cox, and T.B. McKee, 1979: Total Shortwave Radiative Characteristics of Absorbing Finite Clouds. *J. Atmos. Sci.*, **36**, 508-518.
- Davis, J.M., S.K. Cox, and T.B. McKee, 1983: Design and Verification of a Cloud Field Optical Simulator. *J. Climate Appl. Meteor.*, **22**, 947-958.
- Di Girolamo, L., and R. Davies, 1994: A Band-Differenced Angular Signature Technique for Cirrus Cloud Detection. *IEEE Trans. Geosci. Remote Sens.*, **32**, 890-896.
- Diner, D.J., S.R. Paradise, and J.V. Martonchik, 1994: Development of an Aerosol Opacity Retrieval Algorithm for use with Multi-Angle Land Surface Images. *IGARSS'94*, 8-12 Aug., Pasadena, Ca.
- Diner, D.J. et al., 1995a: *MISR Level 2 Algorithm Theoretical Basis: Aerosol / Surface Product, Part 1 (Aerosol Parameters)*. JPL D-11401, Rev. A
- Diner, D.J. et al., 1995b: *MISR Level 2 Algorithm Theoretical Basis: Aerosol / Surface Product, Part 2 (SurfaceParameters)*. JPL D-11401, Rev. A
- Diner, D.J. et al., 1995c: *MISR Level 2 Algorithm Theoretical Basis: TOA / Cloud Product*, JPL D-11507. Rev. A

- Ellingson, R.G., and Y. Fouquart, 1990: *Radiation and Climate. The Intercomparison of Radiation Codes in Climate Models (ICRCCM)*. Report of Workshop, Paris, France, 15-17 Aug. 1988, WCRP-39, WMO/TD-No. 371, WMO, International Council of Scientific Union, 38 pp.
- Evans, K.F., 1993a: A General Solution for Stochastic Radiative Transfer. *Geophys. Res. Lett.*, **20**, 2075-2078.
- Evans, K.F., 1993b: Two-Dimensional Radiative Transfer in Cloudy Atmospheres: The Spherical Harmonic Spatial Grid Method. *J. Atmos. Sci.*, **50**, 3111-3124.
- Frisch, U.P., P.L. Sulem, and M. Nelkin, 1978: A Simple Dynamical Model of Intermittency in Fully Developed Turbulence. *J. Fluid Mech.*, **87**, 719-724.
- Gabriel, P.M., and K.F. Evans, 1996: Radiative Transfer Methods for Calculating Domain-Averaged Solar Fluxes in Inhomogeneous Clouds. *J. Atmos. Sci.*, **53**, 858-877.
- Gabriel, P.M., S.-C. Tsay, and G.L. Stephens, 1993: A Fourier-Ricatti Approach to Radiative Transfer. Part I: Foundations. *J. Atmos. Sci.*, **50**, 3125-3147.
- Gabriel, P.M., S. Lovejoy, A.B. Davis, D. Schertzer, and G.L. Austin, 1990: Discrete Angle Radiative Transfer. Part II: Renormalization Approach for Homogeneous and Fractal Clouds. *J. Geophys. Res.*, **95**, 11717-11728.
- Gierens, K.M., 1993: A Fast Six-Flux Radiative Transfer Method for Application in Finite Cloud Models. *Contrib. Atm. Phys.*, **66**, 73-87.
- Gupta, V.K., and Waymire, E.C., 1993: A Statistical Analysis of Mesoscale Rainfall as a Random Cascade. *J. Appl. Meteor.*, **32**, 251-267.
- Gurney, R.J., J.L. Foster, and C.L. Parkinson, 1993: *Atlas of Satellite Observations Related to Climate Change*. Cambridge University Press, 470 pp.
- Haferman J.L. et al., 1994: Three Dimensional Aspects of Radiative Transfer in Remote Sensing of Precipitation: Application to the 1986 COHMEX Storm. *J. Appl. Meteor.*, **33**, 1609-1622.
- Harshvardhan, 1991: Atmospheric Radiation. *Rev. Geophys.*, *supplement*, 56-68 April 1991
- Harshvardhan, and R.W.L. Thomas, 1984: Solar Reflection from Interacting and Shadowing Cloud Elements. *J. Geophys. Res.*, **89 D**, 7179-7185.
- Harshvardhan, and D.A. Randall, 1985: Comments on the Parameterization of Radiation for Numerical Weather Prediction and Climate Models. *Mon. Wea. Rev.*, **113**, 729-740.
- Hartman, D., 1994: *Global Physical Climatology*. Academic Press, San Diego, 411 pp.

- Hayasaka, T., N. Kikuchi, and M. Tanaka, 1995: Absorption of Solar Radiation by Stratocumulus Clouds: Aircraft Measurements and Theoretical Calculations. *J. Appl. Meteor.*, **34**, 1047-1055.
- IPCC, 1990: *Climate Change: The IPCC Scientific Assessment*. Cambridge University Press, Cambridge, 364 pp.
- Iqbal, M., 1983: *An Introduction to Solar Radiation*. Academic Press, 390 pp.
- Jonas, P.R., 1989: Effect of Radiation on Clouds. *Atmos. Res.*, **23**, 259-286.
- Jonas, P.R., 1990: Observations of Cumulus Cloud Entrainment. *Atmos. Res.*, **25**, 105-127.
- Jonas, P.R., 1994: On the Reflectance of Cellular Cloud Layers. *Quart.J. Roy. Meteor. Soc.*, **120**, 221-230.
- Killen, R., and R.G. Ellingson, 1994: The Effect of Shape and Spatial Distribution of Cumulus Clouds on Longwave Irradiance. *J. Atmos. Sci.*, **51**, 2123-2136.
- Kite, A., 1987: The Albedo of Broken Cloud Fields. *Q.J.R. Meteorol. Soc.*, **113**, 517-531.
- Kneizys, F.X., E.P. Shettle, W.O. Gallery, J.H. Chetwynd, Jr., L.W. Abreau, J.E.A. Selby, R.W. Fenn, and R.A. McClatchey, 1980: *Atmospheric Transmittance / Radiance: Computer Code LOWTRAN 5*. AFGL-TR-80-0067, Environmental Research Papers, No. 697, Air Force Geophysics Laboratory, 233 pp.
- Kobayashi, T., 1988: Parameterization of Reflectivity for Broken Cloud Fields. *J. Atmos. Sci.*, **45**, 3034-3045.
- Kobayashi, T., 1991: Reflected Solar Flux for Horizontally Inhomogeneous Atmospheres. *J. Atmos. Sci.*, **48**, 2436-2445.
- Kobayashi, T., 1993: Effects Due to Cloud Geometry on Biases in the Cloud Albedo Derived from Radiance Measurements. *J. Climate*, **6**, 120-128.
- Korolev, A.V., 1993: On the Formation of non-Adiabatic LWC Profile in Stratiform Clouds. *Atmos. Res.*, **29**, 129-134.
- Li, J., D.J.W. Geldart, and P. Chylek, 1994a: Solar Radiative Transfer in Clouds with Vertical Internal Inhomogeneity. *J. Atmos. Sci.*, **51**, 2542-2552
- Li, J., D.J.W. Geldart, and P. Chylek, 1994b: Perturbation Solution for 3-D Radiative Transfer in a Horizontally Periodic Inhomogeneous Cloud Field. *J. Atmos. Sci.*, **51**, 2110-2122.
- Liou, K.N., 1992: *Radiation and Cloud Processes in the Atmosphere*. Oxford University Press, 487 pp.
- Loeb, N.G., and R. Davies, 1996a: Angular Dependence of Observed Radiation Field: A Comparison with Plane Parallel Theory. submitted to *J. Geophys. Res.*

- Loeb, N.G., and R. Davies, 1996b: Observational Evidence of Plane-Parallel Model Biases at Low Sun Elevations. *J. Geophys. Res.* **101 D**, 1621-1634.
- Loeb, N.G., T. Várnai, and R. Davies, 1996: Solar Zenith Angle Dependence of Solar Radiation Reflected from Inhomogeneous Clouds. submitted to *J. Geophys. Res.*
- Lovejoy, S., 1982: Area-Perimeter Relation for Rain and Cloud Areas. *Science*, **216**, 185-187.
- Lovejoy, S., and B.B. Mandelbrot, 1985: Fractal Properties of Rain, and a Fractal Model. *Tellus*, **37A**, 209-232.
- Lovejoy, S., and D. Schertzer, 1985: Generalized Scale Invariance in the Atmosphere and Fractal Models of Rain. *Water Resour. Res.*, **21**, 1233-1250.
- Lovejoy, S., A. Davis, P. Gabriel, D. Schertzer, and G.L. Austin, 1990: Discrete Angle Radiative Transfer 1. Scaling and Similarity, Universality and Diffusion. *J. Geophys. Res.*, **95**, 11699-11715.
- Lovejoy, S., D. Schertzer, P. Silas, Y. Tessier, and D. Lavallée, 1993: The Unified Scaling Model of Atmospheric Dynamics and Systematic Analysis of Scale Invariance in Cloud Radiances. *Ann. Geophysicae*, **11**, 119-127.
- Lovejoy, S., B. Watson, D. Schertzer, and G. Brosamlen, 1995: Scattering in Multifractal Media. *Proc. of Particle Transport in Stochastic Media*, L. Briggs Ed., Amer. Nuclear Soc., Portland, Or., 750-760.
- Malvagi, F., R.N. Byrne, G.C. Pomraning, and R.C.J. Somerville, 1993: Stochastic Radiative Transfer in a Partially Cloudy Atmosphere. *J. Atmos. Sci.*, **50**, 2146-2158.
- Marchuk, G.I., G.A. Mikhailov, M.A. Nazaraliev, R.A. Darbinjan, B.A. Kargin, and B.S. Elopov, 1980: *The Monte Carlo Methods in Atmospheric Optics*. Springer-Verlag, Berlin, 208 pp.
- Marshak, A., A. Davis, W. Wiscombe, and R. Cahalan, 1995a: Radiative Smoothing in Fractal Clouds. *J. Geophys. Res.*, **100 D**, 26247-26261.
- Marshak, A., A. Davis, W. Wiscombe, and G. Titov, 1995b: The Versimilitude of the Independent Pixel Approximation Used in Cloud Remote Sensing. *Remote Sens. Environ.*, **52**, 71-78.
- McKee, T.B., and S.K. Cox, 1974: Scattering of Visible Radiation by Finite Clouds. *J. Atmos. Sci.*, **31**, 1885-1892.
- McKee, T.B., and J.T. Klehr, 1978: Effects of Cloud Shape on Scattered Solar Radiation. *Mon. Wea. Rev.*, **106**, 399-404.
- Minnis, P., 1989: Viewing Zenith Angle Dependence of Cloudiness Determined from Coincident GOES East & West Data. *J. Geophys. Res.*, **94**, 2303-2320.

- O'Brien, D.M., 1992: Accelerated Quasi Monte Carlo Integration of the Radiative Transfer Equation. *J. Quant. Spectroscopy Radiative Transfer*, **48**, 41-59.
- Oreopoulos, L. 1996: *Plane-parallel Albedo Bias from Satellite Measurements*. Ph.D thesis, McGill University, Montreal, 142 pp.
- Padro-Igúzquiza, E., and M. Chica-Olmo, 1994: SPECSIM: A Program for Simulating Random Fields by an Improved Spectral Approach. *Computers and Geosciences*, **20**, 597-613.
- Paltridge, G.W., and C.M.R. Platt, 1976: *Radiative Processes in Meteorology and Climatology*. Elsevier Scientific Pub. Co., Amsterdam, New York, 318 pp.
- Pincus, R., M. Szczordak, J. Gu, and P. Austin, 1995: Uncertainty in Cloud Optical Depth Estimates Made from Satellite Radiance Measurements. *J. Climate*, **8**, 1638-1657.
- Pflug, K., S. Lovejoy, and D. Schertzer, 1993: Differential Rotation and Cloud Texture: Analysis Using Generalized Scale Invariance. *J. Atmos. Sci.*, **50**, 538-553.
- Price, R.D., et al., 1994: Earth Science Data for All: EOS and the EOS Data Information System. *Photogramm. Eng. Remote Sens.*, **60**, 277-285.
- Romanova, L.M., 1975: Radiative Transfer in a Horizontally Inhomogeneous Scattering Medium. *Izv. Acad. Sci. USSR, Atmos. Oceanic Phys.*, **12**, 808-818.
- Rossow, W.B., 1989: Measuring Cloud Properties from Space: A Review. *J. Climate*, **2**, 201-213.
- Rossow, W.B. et al., 1985: ISCCP Cloud Algorithm Intercomparison. *J. Climate Appl. Meteor.*, **24**, 877-903.
- Sánchez, A., Krajewski, W.F., and Smith, T.F., 1992: *A General Purpose Radiative Transfer Model for Application to Remote Sensing in Multi-dimensional Media*. IIHR Report # 335, Iowa Institute of Hydraulic Research, The University of Iowa, Iowa City, Iowa, 216 pp.
- Sassen, K., and K.-N. Liou, 1979: Scattering of Polarized Laser Light by Water Droplet, Mixed-Phase and Ice Crystal Clouds. Part I: Angular Scattering Patterns, *J. Atmos. Sci.*, **36**, 838-851.
- Schertzer, D., and S. Lovejoy, 1987: Physical Modeling and Analysis of Rain and Clouds by Anisotropic Scaling Multiplicative Processes, *J. Geophys. Res.*, **92**, 9693-9714
- Schmetz, J., 1984: On the Parameterization of the Radiative Properties of Broken Clouds. *Tellus*, **36A**, 417-432.
- Smith, T.F., and J.R. Ehlert, 1993: Albedos for a Cloud Bar Array over a Reflecting Surface. *J. Geophys. Res.*, **98**, 5059-5068.

- Stackhouse, P.W., Jr., and G.L. Stephens, 1994: Investigation of the Effects of the Macrophysical and Microphysical Properties of Cirrus Clouds on the Retrieval of Optical Properties: Results from FIRE II. *Eight Conference on Atmospheric Radiation, Amer. Met. Soc.*, January 23-28, 1994, Nashville, Tn, 225-227.
- Stephens, G.L., 1988: Radiative Transfer through Arbitrarily Shaped Optical Media: Part I. A General Method of Solution. *J. Atmos. Sci.*, **45**, 1818-1836.
- Stephens, G.L., and C.M.R. Platt, 1987: Aircraft Observations of the Radiative Properties of Stratocumulus and Cumulus Cloud Fields. *J. Climate Appl. Meteor.*, **26**, 1243-1269.
- Stephens, G.L., P.M. Gabriel, and S. Tsay, 1991: Statistical Radiative Transport in One-dimensional Media and its Application to the Terrestrial Atmosphere. *Transport Th. Statist. Phys.*, **20**, 139-175.
- Stuhlmann, R., P. Minnis, and G.L. Smith, 1985: Cloud Bidirectional Reflection Functions: A Comparison of Experimental and Theoretical Results. *Appl. Opt.*, **24**, 396-401.
- Takano, Y., and K.N. Liou, 1989: Solar Radiative Transfer in Cirrus Clouds. Part I: Single-Scattering and Optical Properties of Hexagonal Ice Crystals. *J. Atmos. Sci.*, **46**, 3-19.
- Takano, Y., and K.N. Liou, 1995: Radiative Transfer in Cirrus Clouds. Part III: Light Scattering by Irregular Ice Crystals. *J. Atmos. Sci.*, **52**, 818-837.
- Taylor, V.L., and L.L. Stowe, 1984: Reflectance Characteristics of Uniform Earth and Cloud Surfaces Derived from Nimbus-7 ERB. *J. Geophys. Res.*, **89**, 4987-4996.
- Tessier, Y., S. Lovejoy, and D. Schertzer, 1993: Universal Multifractals: Theory and Observation for Rain and Clouds. *J. Appl. Meteor.*, **32**, 223-250.
- Titov, G.A., 1990: Statistical Description of Radiative Transfer in Clouds. *J. Atmos. Sci.*, **47**, 24-38.
- Vonder Haar, T.H., 1983: Climate Studies from Satellite Observations: Special Problems in the Verification of Earth Radiation Balance, Cloud Climatology, and Related Experiments. *Adv. Space Res.* **2**, 3-10.
- Vonder Haar, T.H., 1994: The Global Energy Budget and Satellite Observations. *Adv. Space Res.* **14**, 131-144.
- Wang, M., and H.R. Gordon, 1994: Estimating Aerosol Optical Properties Over the Oceans with MISR: Some Preliminary Studies. *Appl. Opt.*, **33**, 4042-4057.
- Welch, R.M., and W.G. Zdunowski, 1981: The Effect of Cloud Shape on Radiative Characteristics. *Contrib. Atmos. Phys.*, **54**, 482-491.

- Welch, R.M., and B.A. Wielicki, 1984: Stratocumulus Cloud Field Reflected Fluxes: The Effect of Cloud Shape. *J. Atmos. Sci.*, **41**, 3085-3102.
- Welch, R.M., S.K. Cox, and J.M. Davis, 1980: *Solar Radiation and Clouds*. Meteorological Monographs, **17**, #39, American Meteorological Society, 96 pp.
- Wendling, P., 1977: Albedo and Reflected Radiance of Horizontally Inhomogeneous Clouds. *J. Atmos. Sci.*, **34**, 642-650.
- Wielicki, B.A., et al., 1995: Mission to Planet Earth: Role of Clouds and Radiation in Climate. *Bull. Amer. Meteor. Soc.*, **76**, 2125-2153.
- Zuev, V.E., and G.A. Titov, 1995: Radiative Transfer in Cloud Fields with Random Geometry. *J. Atmos. Sci.*, **52**, 176-190.
- Xu, K.M., and D.A. Randall, 1995: Impact of Interactive Radiative Transfer on the Macroscopic Behavior of Cumulus Ensembles. Part II: Mechanisms for Cloud-Radiation Interactions. *J. Atmos. Sci.*, **52**, 785-799.